

Dynamic Monte–Carlo modeling of hydrogen isotope reactive–diffusive transport in porous graphite

I n a u g u r a l d i s s e r t a t i o n

zur

Erlangung des akademischen Grades
doctor rerum naturalium (Dr. rer. nat.)

an der Mathematisch-Naturwissenschaftlichen Fakultät

der

Ernst-Moritz-Arndt-Universität Greifswald



vorgelegt von

Abha Rai

geboren am 01.04.1981

in Ghazipur, Indien

Greifswald, 03.12.2007

Dekan

1. Gutachter:

2. Gutachter:

Tag der Promotion:

I dedicate this work to my

father Vinod Kumar Rai,

mother Krishna Rai and

husband Gaurang Dilip Phadke

for support, encouragement and love.

Abstract

Plasma material interaction in fusion devices is a critical issue that affects the overall machine performance. In the current design of ITER graphite has been chosen as a plasma facing material (PFM) in the regions where heat loads are extremely high (10 MW/m²) due to its good thermal conductivity and low atomic number. The two main topics regarding interaction of hydrogen isotopes and graphite that need to be understood properly are: (i) hydrogen retention and release and (ii) chemical erosion and its flux dependence. The problem of tritium retention is extremely important to study because tritium is a radioactive material and its long term inventory in a fusion device should stay below the safety limit (350 g tritium).

The physics of the interaction of hydrogen with graphite used in the fusion devices is multi-scale in space (Å to cm) and time (pico-seconds to seconds). The idea is to use the insights gained from the microscopic models (MD or ab-initio methods) for modeling the transport at the meso-scale and further at the macro-scale in order to understand the physical processes contributing to macroscopic transport.

The 3D multi-scale model developed by Warriier et al. [1] has been improved to model the hydrogen reactive-diffusive transport in porous graphite. Sensitivity studies of the various factors affecting the retention and release of hydrogen from graphite have been performed. The void fraction has the most dominant role followed by the void size and then the void orientation comes into play. The model allows extrapolation of well diagnosed ion-beam experiments to fusion conditions.

The model has been applied to study hydrogen retention and release from the deposits collected from the leading edge of the neutralizer of Tore Supra. These deposits consists of micropores with typical size lower than 2 nm ($\sim 11\%$), mesopores (typical size between 2 and 50 nm, $\sim 5\%$) and macropores with a typical size more than 50

nm. The simulations showed that the macropores play the dominant role in retention and release behavior of hydrogen. The hydrogen released from the micropores and mesopores gets adsorbed on the surfaces of the macropores. The internal deposition of hydrogen will further enhance the tritium retention problem. In order to understand the hydrogen transport mechanism in graphite the isotope exchange reaction has been studied. The mixed molecule formation during the exposure to hydrogen and deuterium ion beams with completely separate ion profile (penetration depths) demonstrates that hydrogen molecule formation is not a local process. It takes place throughout the implantation zone and not only at the end of the ion range.

The model for chemical erosion of graphite due the thermal hydrogen ion bombardment proposed by Horn et al. [2] has been implemented. A simple 1D-KMC model has been developed to check the implementation of the basic atomistic process occurring during the chemical erosion process. The simple 1D-KMC model has been successfully validated against the analytical model and the experimental results of Horn et al. [2]. The model is extended to 3D and the effect of the internal structure of graphite on CH_3 molecule formation has been studied. It has been shown that samples with larger internal surface areas facilitate CH_3 molecule formation. The flux dependence predicted with this model is very weak.

To study the flux dependence of chemical erosion a simple multi-scale model has been developed. The basic idea here is that due to the shielding of the carbon atoms lying in the lower layers only few surface layers are accessible by the incoming hydrogen ions. This puts an upper limit on the released carbon flux. The model agrees very well with the experimental trends. After a certain critical incident flux, the carbon flux released from a sample becomes equal for all incident hydrogen fluxes and the erosion yield decreases by orders of magnitude with increasing flux. The erosion yield shows a very strong flux dependence which indicates that the problem of carbon erosion and co-deposition will not be as severe as predicted and carbon will still be a good candidate as a PFM for ITER.

Contents

Abstract	v
1 Introduction	1
1.1 Basics of plasma material interaction	2
1.2 Plasma facing materials	7
1.2.1 Interaction of hydrogen plasma with carbon based materials . .	9
1.3 Motivation	14
1.4 Outline	15
2 Methods and techniques	19
2.1 Molecular dynamics	19
2.2 Kinetic Monte-Carlo	20
2.2.1 The Bortz-Kalos-Lebowitz algorithm	21
2.2.2 Time dependency in BKL	22
2.3 Monte-Carlo-Diffusion	23
2.4 Implementation of ion flux	24
2.5 Generation of the 3D porous graphite geometry	24
2.6 Recap	26
3 Multi-Scale Scheme	27
3.1 Parametrization of the processes	30
3.1.1 Hydrogen atoms	30
3.1.2 Hydrogen molecules	36
3.2 Recap	38
4 Hydrogen retention and release from porous graphite	39
4.1 Validation of the model	40

4.2	Setting up the simulation	40
4.3	Results	41
4.3.1	Effect of the range of penetration of incident ion beam	44
4.3.2	Effect of incident flux	46
4.3.3	Effect of trap site density	46
4.3.4	Effect of the void orientation	48
4.3.5	Effect of the void fraction	49
4.3.6	Effect of the void size	51
4.4	Recap	51
5	Retention and release from Tore Supra Co-deposits	53
5.1	Structure of Tore Supra co-deposits	54
5.2	Analysis of deposits at meso-scale	55
5.2.1	Setting up the simulation	55
5.2.2	Results at meso-scale	57
5.3	Scaling up to macro-scale	60
5.3.1	Setting up the simulation	61
5.3.2	Results at macro-scale	62
5.4	Recap	67
6	Isotope exchange in graphite	69
6.1	Isotope exchange: present status	69
6.2	Completely overlapping ion profiles	71
6.2.1	Setting up the simulation	71
6.2.2	Results	72
6.3	Completely separated ion profiles	74
6.3.1	Setting up the simulation	74
6.3.2	Results	75
6.4	Recap	77
7	Chemical erosion of graphite	79
7.1	Analytical description of chemical erosion	79
7.1.1	Thermally activated process	80
7.1.2	Radiation damage	83
7.1.3	Kinetic hydrocarbon emission	83
7.2	A simple 1D-KMC model for chemical erosion	84

7.2.1	Validation of the simple 1D–KMC model for chemical erosion	85
7.2.2	Flux dependence of chemical erosion	86
7.3	A 3D–KMC model for chemical erosion	88
7.3.1	Setting up the simulation	89
7.3.2	Results	89
7.4	Recap	91
8	Flux dependence of chemical erosion: a simple multi–scale model	93
8.1	Description of the model	94
8.2	Setting up the simulation	94
8.3	Results	95
8.4	Recap	98
9	Summary and conclusions	101
	Acknowledgments	113

Chapter 1

Introduction

Controlled thermonuclear fusion has the potential to open a new energy source to mankind and to contribute to a peaceful world. The fuel used in this reaction is a mixture of deuterium and tritium which is created from the breeding of lithium by using some of the released neutrons in the fusion reaction. A complete design of a machine which will deliver energy from magnetically confined thermonuclear fusion reactions under quasi-stationary conditions is now ready for construction – the International Tokamak Experimental Reactor (ITER). The design of ITER is the collaborative result of worldwide fusion research in many experimental devices [3]. Their results give rise to a strong confidence that the design will meet the scientific and technological objectives of ITER:

- long-pulse (about 7 min) burning fusion plasma capable of delivering 500 MW fusion power with an energy amplification factor Q^1 of at least 10
- testbed for studying the steady-state plasma operation
- investigation of quasi-steadystate plasma operation which could allow to extend the pulse length up to 30 min under ‘Hybrid’ scenarios with $Q = 5$
- integration of fusion relevant physics and technology (tritium breeder blanket, superconductors, heating) with significant flexibility which allows to exploit progress made in various areas aiming at performances which would lead to a commercial thermonuclear fusion power plant.

For long time operation of any fusion machine two requirements are crucial:

¹The ratio of the fusion power to the external power input.

- (i) a stationary magnetic field configuration for plasma confinement and
- (ii) a sufficient life time of wall components.

The second requirement is related to the plasma wall interaction which is also studied in this thesis. In order to understand the second requirement it is necessary to identify the main atomistic processes occurring during the interaction of the plasma with the wall material.

1.1 Basics of plasma material interaction

Graphite is used in many fusion devices as plasma facing wall material (PFM). In this section the different atomistic processes taking place during the interaction of energetic hydrogen ions and neutrals with a graphite sample are delineated (Fig. 1.1).

When charged particles (ions or electrons) strike a solid surface they stick to it. While ions do have a finite probability of back-scattering from the surface, they do so mainly as neutrals picking up electrons from the surface. The neutral atoms are re-emitted back into the plasma where they can be re-ionized, usually by electron impact.

The incident energetic atom collides with a target surface atom and transfers its momentum, consequently it can either get reflected from the surface (backscattering) or it penetrates into the target and after a collision cascade comes to rest in thermal equilibrium with the target atoms (implantation) (Fig. 1.2). The target atoms which reach the surface and have more energy than the surface binding energy of the target material can be released from the surface (physical sputtering). The physical sputtering and backscattering depends on the atomic masses of the incident ion and the target, the energy and the angle of incidence of the incident ion. The erosion of the surface by physical sputtering and the implantation of atoms can lead to changes in the composition and structure of the material. Thus, one factor for the limited lifetime of the PFMs in fusion devices is sputtering.

In fusion machines where carbon-based materials are used as PFM incident hydrogen isotope atoms which have equilibrated with the surface diffuse within the target and can undergo chemical reactions with the target atoms to form hydrocarbons and

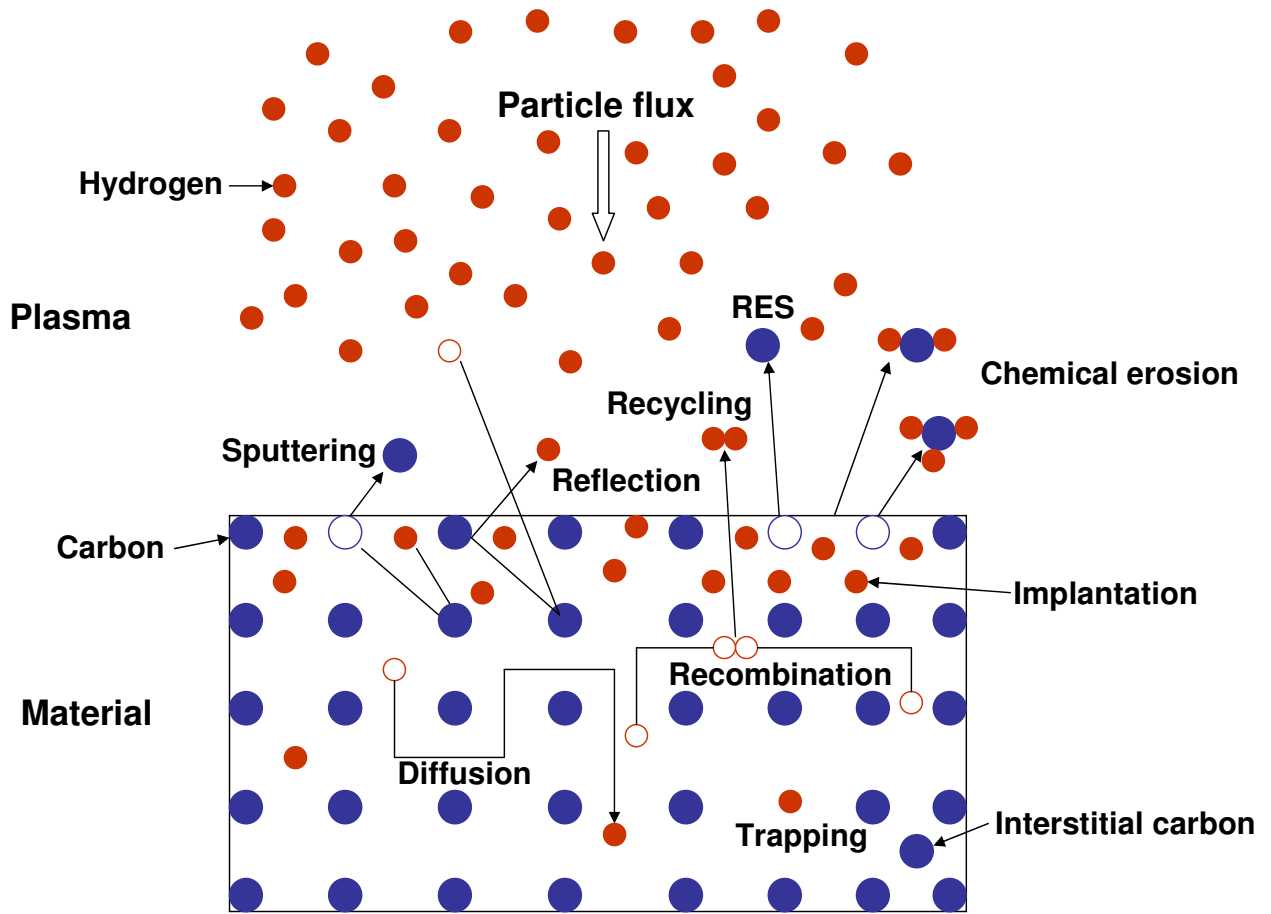


Figure 1.1: Overview of the atomistic processes during plasma surface interactions in fusion machines relevant to particle recycling. The acronym RES represents radiation enhanced sublimation process.

hydrogen molecules. Some of these molecules diffuse to the target surface and can either be desorbed by incident atoms or be released thermally from the surface depending on the surface temperature (chemical erosion). In some cases the incoming energetic hydrogen atom or ion breaks a covalent C–C bond on the graphite surface by pushing apart the carbon atoms due to its short range repulsive potential. This can result in the ejection of either a carbon atom or a hydrocarbon and is called swift chemical sputtering.

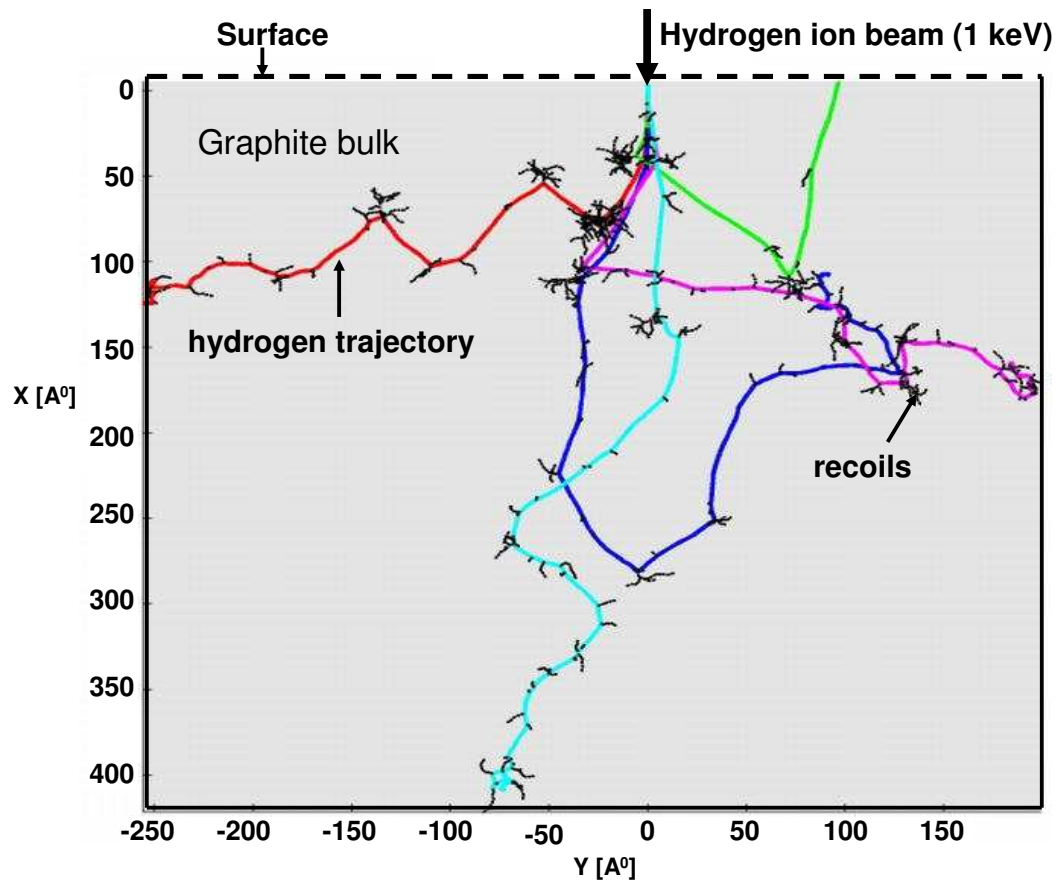


Figure 1.2: Collisional cascade created in graphite by 1 keV hydrogen ion beam. The simulation was done using the TRIM code.

All sputtering processes are characterized by the *sputtering yield*, Y , which is the number of atoms or molecules ejected per impacting particle. Physical sputtering depends on

- The energy of the incident particle,
- Atomic mass of the incident and target atoms,
- Angle of incidence of the incident particle,
- Surface roughness of the target.

For physical sputtering to occur, enough momentum must be transferred to the lattice atom to overcome the surface binding energy, thus a *threshold energy* E_{th} exists for physical sputtering, below which no sputtering occurs. The value of E_{th} can be estimated from the surface binding energy of the target. The physical sputtering yield can be calculated using, for example, the binary collision TRIM code.

Chemical sputtering is dependent on

- The energy and mass of the incident particle,
- The target temperature,
- Incident flux of particles.

No threshold kinetic energy is needed for chemical sputtering to occur, and yields even for sub-eV hydrogen ion bombardment are not negligible [4]. The strong dependence on the threshold temperature is one of the key signatures of chemical sputtering [5]. Chemical sputtering is dominant for incident ion energy $E_0 \leq 100$ eV, except at extremely high temperatures [6]. For $E_0 \approx 100$ eV chemical sputtering yields are comparable to or even larger than physical sputtering yields.

The energy deposited by the plasma on the surface determines the surface temperature which is an important parameter in determining the diffusion of the various species and the molecule formation on the surface. At very high incident energy flux and / or insufficient cooling of the target, the surface temperature can be increased and the surface atoms can thermally evaporate. Besides, implanted gas atoms can accumulate in the surface layers to form bubbles. This leads to blister and flake formation and breaking of the surface layer [7].

The bombardment of energetic atoms creates damage sites (traps) and interstitials within their range of penetration in the target. This process competes with the annealing of the lattice defects by the recombination of interstitials and vacancies. Due to the relatively high flux densities and fluences on the target plates in tokamaks the recombination rate is not high enough to anneal all the damage. This results in net production of damage and amorphization of the target surface. The porous structure of the graphite offers a large internal surface area along which the incident hydrogen

atoms can diffuse and penetrate much beyond the implantation range of the ions.

On the way of realizing fusion power to a commercial reactor, still a set of critical questions related to the plasma–wall interaction remain to be addressed sufficiently in present experiments. The main constraints are:

- (i) to achieve technically acceptable condition for power (continuous heat flux of 10 MW/m² on divertor target plates) and particle (sufficient helium pumping to avoid plasma dilution) exhaust.
- (ii) to achieve sufficient lifetime of PFMs. The lifetime of PFMs can be reduced mainly due to
 - transient heat loads due to disruptions² and edge localized modes (ELMs)³
 - physical and chemical erosion
- (iii) to stay below the safety limit (350 g tritium) of long term tritium inventory.

In magnetic confinement devices the edge plasma is used to buffer the high temperature plasma core from the material walls [8]. The interaction between the edge plasma and the PFMs profoundly influences the conditions in the core plasma and the tokamak operation in many ways. Retention and recycling of hydrogen from plasma facing components (PFCs) affects fueling efficiency, plasma density control and the density of neutral hydrogen in the plasma edge, which further influences particle and energy transport. Erosion by the plasma is the source of impurities and determines the lifetime of PFCs. The eroded impurity atoms can get into the plasma and radiate energy, which cools and dilutes the plasma.

²Sudden loss of plasma confinement. The stored energy in the plasma is rapidly dumped into the rest of the plasma system (vacuum vessel walls, magnet coils, etc.) and can cause significant damage if precautions are not taken.

³ELMs are MHD related events that play a key role in mediating the energy and particle transport characteristic of the plasma edge in the regime of enhanced global energy confinement called the high confinement mode. They involve the very rapid expulsion of energy and particles from the outer part of a confined plasma into the SOL and can transiently reduce the temperature and density in this region and thereby affect the core confinement. In addition, they can lead to increased peak heat loads on the divertor plates.

1.2 Plasma facing materials

In a tokamak the outer magnetic field lines are diverted to a location far from the plasma by means of specially shaped magnetic fields. Thus the energy and the particles move to restricted areas of the vessel wall. The field lines contact the vessel wall on specially equipped divertor plates. With this configuration it is possible to produce much purer plasmas, i. e. less contaminated by foreign atoms than limiter⁴ plasmas. The last closed flux surface (LCFS) is the boundary between the core plasma in a tokamak (or other device), where the field lines form closed flux-surfaces, and the scrape-off-layer (SOL)⁵ where they run into a material wall.

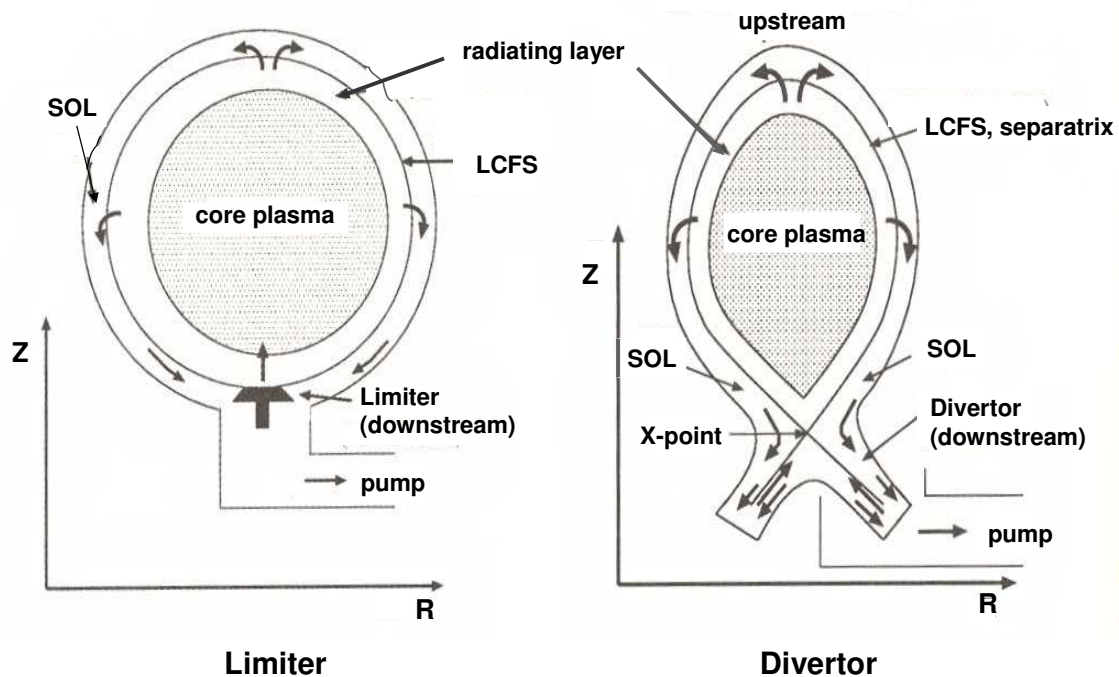


Figure 1.3: Schematic view of a limiter (left side) and divertor (right side). The abbreviations used are SOL: Scrape-off-layer, LCFS: Last closed flux surface.

The main function of the divertor system is to exhaust the major part of the alpha

⁴Structures placed in contact with the edge of a confined plasma which are used to define the shape of the outermost magnetic surface.

⁵Outer layer of a plasma, which is affected ('scraped off') by a divertor or limiter. That is, the outer layer of a magnetically confined plasma where the field lines intersect a material surface (limiter or divertor plate) rather than closing upon themselves. Plasma crossing into the SOL is rapidly lost since transport along the field is much faster than that across the field.

particle power as well as He and impurities from the plasma. As the main interface component under normal operation between the plasma and material surfaces, it must tolerate high heat loads while at the same time providing neutron shielding for the vacuum vessel and magnet coils in the vicinity of the divertor. Although good progress has been made in the understanding of divertor plasma physics, there continues to be some uncertainties, and hence the divertor remains an experimental device, which, it is anticipated, will need to be replaced and upgraded during the life of ITER. To facilitate rapid replacement, remote maintainability of the divertor has been given a high priority.

Plasma-wall interaction (PWI) in a typical divertor machine concerns the armor of the first wall in the main chamber and the components of the divertor. In a typical fusion device the heat flux is of the order of a few MW/m² and particle flux is a few times $10^{23} m^{-2}s^{-1}$ up to $10^{25} m^{-2}s^{-1}$ for ITER. Therefore the requirements for plasma facing material are very good thermal conductivity, high melting point and low radiation losses. The radiation loss is proportional to the atomic number number Z raised to the fourth power [9] which makes low Z material a better choice as a PFM. Additionally, if a low Z impurity enters into the core of the plasma, due to the lesser radiation losses comparatively high impurity levels can be tolerated. Factors for the selection of PFMs are the requirements of plasma performance (minimize impurity contamination and the resulting radiation losses in the core plasma), engineering integrity, component lifetime (need to withstand thermal stresses, acceptable erosion), compatibility with the neutron environment and safety (minimize tritium and radioactive dust inventories). The heat load to the main chamber wall is determined by the radiative processes (bremsstrahlung from the core and impurity radiation from the plasma boundary) and charge exchange fluxes [8].

The peak heat load of about 10 MW/m² occurs at the strike point on the divertor plates by plasma flow along the magnetic field lines. In the current design of ITER (Fig. 1.4) graphite has been chosen for this region because of its 'forgiving' nature. It does not melt (but sublimates) and preserves its shape even with transient heat loads much beyond the acceptable steady state heat flow. The other advantages of using graphite as PFM include low radiative power losses due to its low Z . Also, its radiation characteristics allows a lot of radiation losses on open field lines outside the core allowing a perfect combination with a divertor operation to spread the power over a large area.

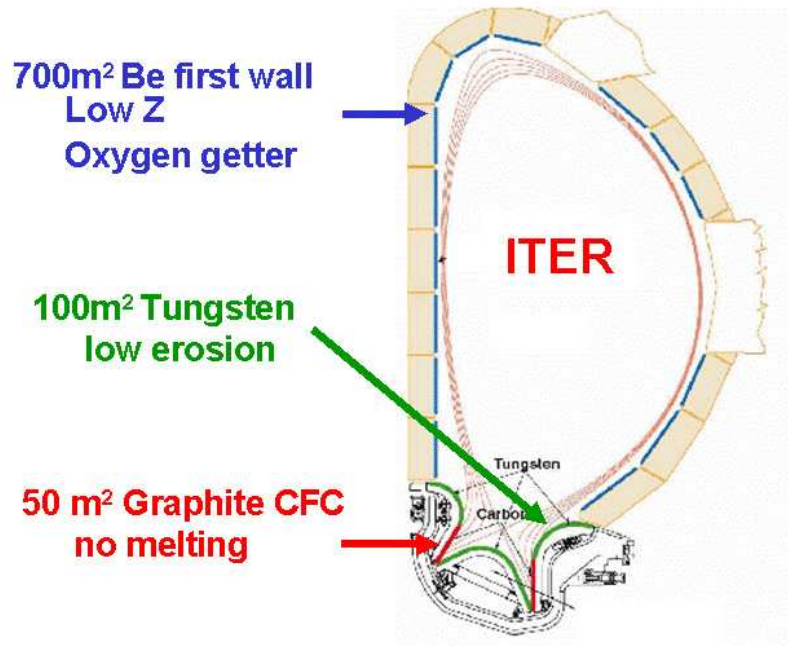


Figure 1.4: ITER cross-section showing the choice of materials for the plasma facing components [10].

1.2.1 Interaction of hydrogen plasma with carbon based materials

The graphite used in fusion devices consists of granules (typically 1-10 micrometer, macroscale) separated by voids which are typically a fraction of a micrometer. The granules consist of graphitic micro-crystallites of size 10-100 nm separated by micro-voids which are typically one nm (mesoscale) [11, 12] (Fig. 1.5). These sub-structures, voids and micro-voids provide a large internal surface area inside graphite where the hydrogen interstitial atoms can diffuse and react with each other which will affect the

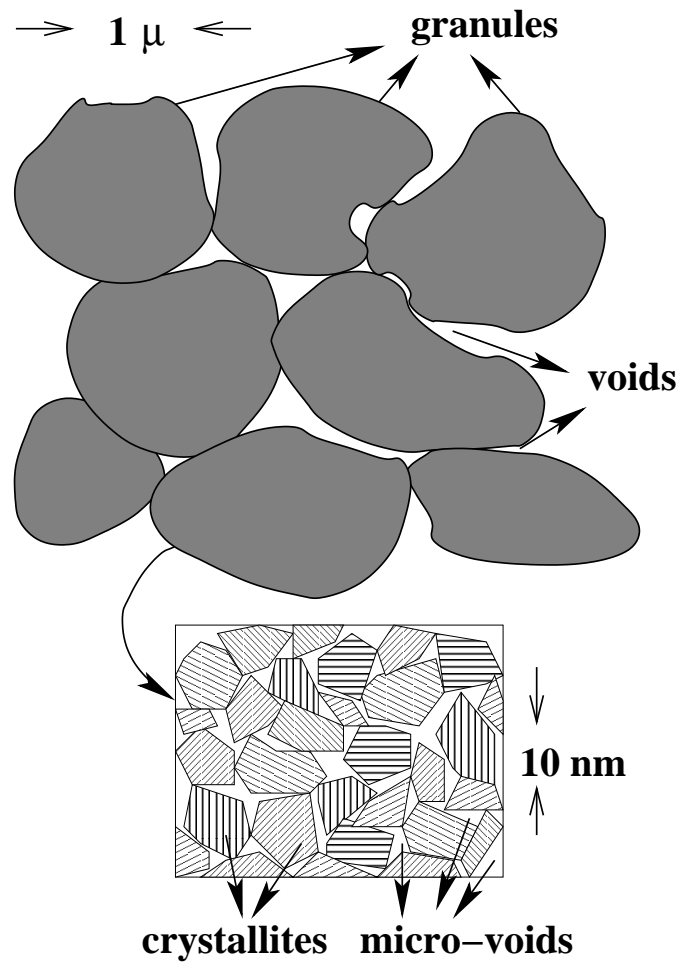


Figure 1.5: The porous structure of graphite.

hydrogen isotope inventory and recycling behavior and also chemical erosion. Due to the large internal surface area provided by graphite it acts like a sponge for hydrogen. In case of carbon based plasma facing materials, essentially four mechanisms have been identified for the retention and uptake of hydrogen [13] (Fig 1.6)

- (i) formation of a saturated surface layer
- (ii) surface diffusion on the internal porosity
- (iii) trans-granular diffusion and bulk trapping
- (iv) co-deposition of hydrogen with plasma exposed surfaces

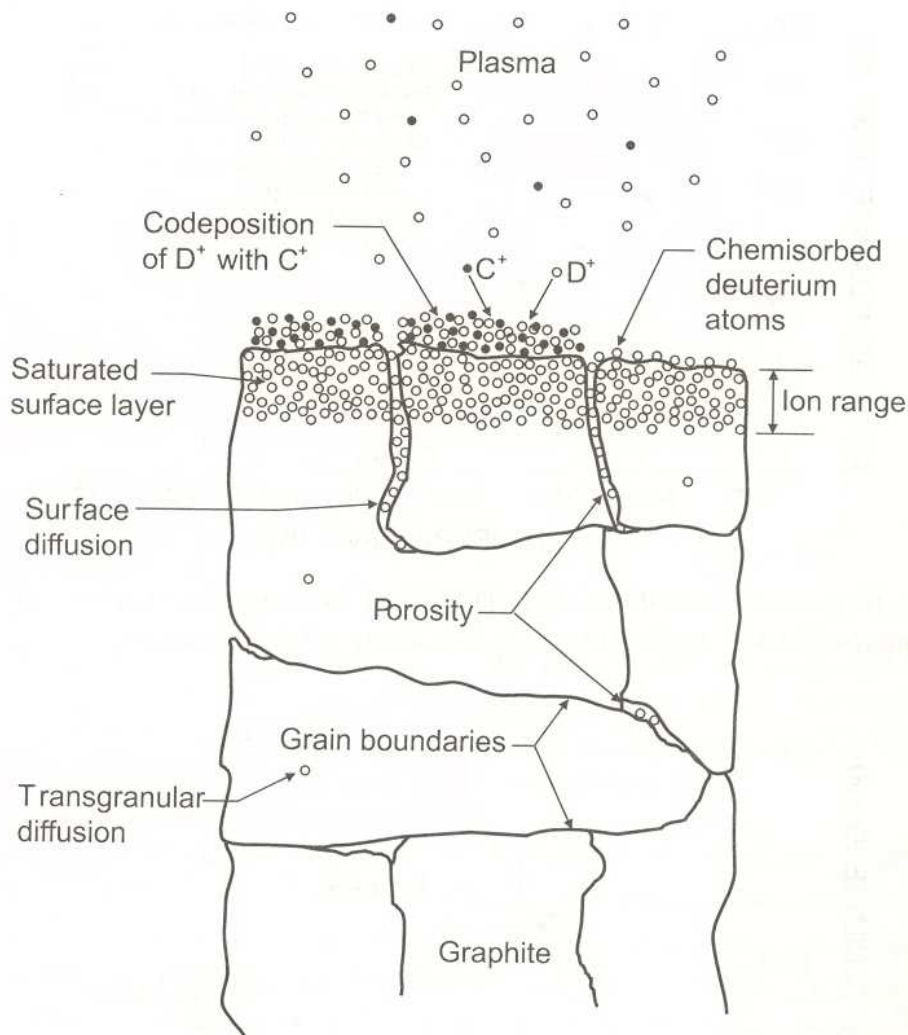


Figure 1.6: Schematic of the primary mechanisms for hydrogen retention and transport in graphite [14].

Formation of a saturated surface layer

Implantation of hydrogen into graphite creates broken carbon bonds and due to the strong chemical reactivity of carbon with hydrogen, hydrogen can be strongly bound through the formation of C–H chemical bonds (≈ 4.5 eV). Fig. 1.6 shows the primary mechanisms responsible for the retention of energetic hydrogen impacting on the carbon based materials. At low fluences and low temperature most of the non-reflected hydrogen is trapped and retained in the graphite. After the saturation of the implantation region is achieved, re-emission sets in and most of the incident flux is re-emitted. The amount of hydrogen in the implantation zone is ~ 0.4 H/C at room temperature.

This hydrogen concentration level extends from the surface till the penetration depth (range) of the incident hydrogen ions. The range of the hydrogen ions depends on the energy of the incident flux and is less for the lower energy. Thus a smaller quantity of hydrogen is trapped for lower energy hydrogen ions.

Diffusion

As the temperature is increased (≥ 1000 K) the detrapping of the hydrogen atoms starts, leading to release of hydrogen and decrease of retention level in the implantation zone. Upon further bombardment following the saturation of the implantation zone, the hydrogen atoms and molecules start diffusing deep into the bulk (much beyond the implantation zone) along the internal porosity or the grain boundary of the granules, as shown in Fig. 1.6. At temperatures above ~ 1000 K, the hydrogen atoms start entering into the granules and trans-granular diffusion sets in. This gives rise to the access to the trapping sites in the grains which are practically inaccessible at low temperatures and therefore the retention levels start to increase again [15]. This transport mechanism will be very important for the neutron irradiated samples which have a huge density of the trapping sites created because of the damage caused to the sample during irradiation process and will result in higher retention levels.

Co-deposition

The carbon atoms which are sputtered from graphite or other carbon based materials due to the impacting plasma particles can either be co-deposited as neutrals or ions due to the plasma chemistry processes in hydrocarbon plasmas, on both plasma facing and out of line-of-sight surfaces in the device (See Fig. 1.7). The layer that is formed is similar to the saturated implant layer described above. But, the saturated implant layers have a thickness of several tens of nm (depending on energy) whereas, the co-deposited layers seem to have no upper limit to their thickness [16] and may extend to several μm . If the layer gets too thick one produces dust and flakes. Both kinds of layers have similar H/C ratio, viz, ~ 0.4 at room temperature. These thick co-deposited layers make it difficult to put an upper limit on the tritium inventory that would result during the co-deposition process in future fusion devices. Most of the tritium in ITER is expected to be trapped in the co-deposited layers [17], consequently, the removal of such layers has become a high priority issue.

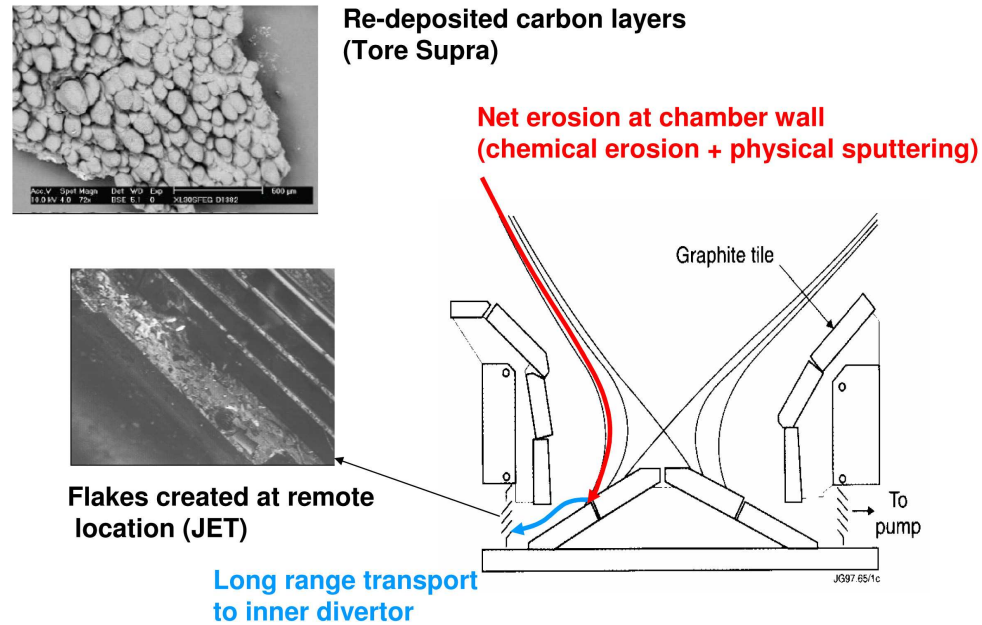


Figure 1.7: Divertor cross-section of JET. The photograph on the lower left side shows a typical region of the flaking deposition on the louvers at the inner corner of the JET Mk-IIA divertor [8, 18]. The figure on the top shows the scanning electron microscopy micrographs of the Tore Supra samples collected from the TS-NTR [19].

The main shortcomings of graphite as a PFM are

- Chemical erosion leads to co-deposition of tritium with eroded carbon (Fig. 1.7).
- Co-deposited layers have apparently no upper limit on their thickness (even though there is a mechanical limit where the layers start flaking and produce dust) and are a source of large tritium inventory.
- Chemical erosion and physical sputtering further reduces the erosion life time.
- Uncertainty about the extrapolation of the chemical sputtering yield to high reactor relevant fluxes (Fig. 1.8). If the chemical sputtering really decreases

with the increasing flux ($10^{25} \text{ m}^{-2}\text{s}^{-1}$ for ITER), then carbon might still be an acceptable choice as a PFM.

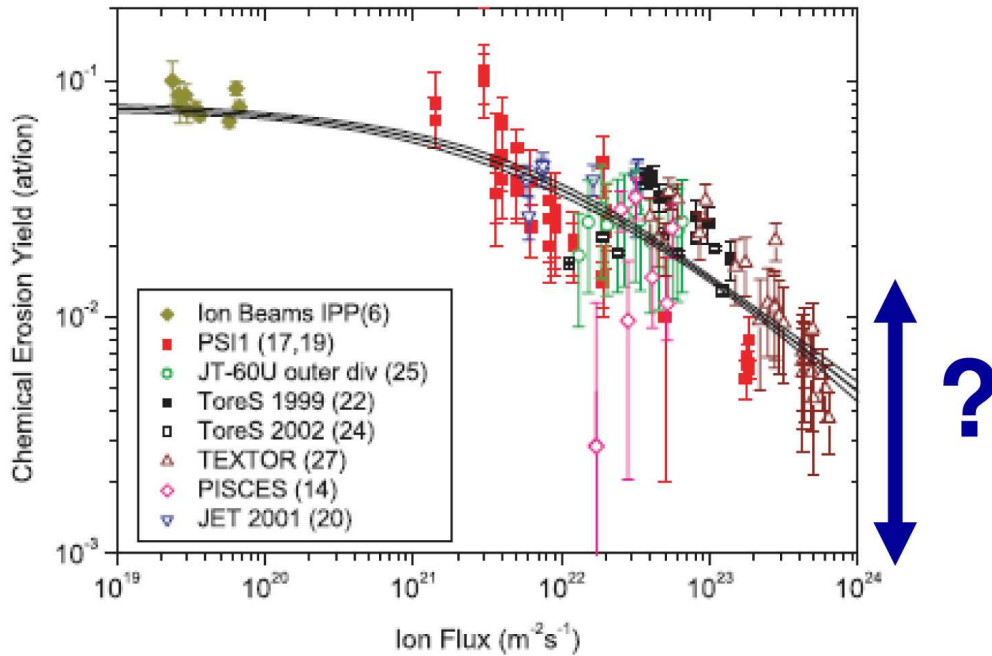


Figure 1.8: Flux dependence of the chemical erosion yield for T_{max} and an ion energy of 30 eV determined from spectroscopic measurements in different fusion devices and plasma simulators. The *solid lines* are a fit using Bayesian probability theory and its confidence intervals [20, 21].

The two most important implications of tritium inventory buildup in ITER are the trapping of the fuel in the PFMs (reducing the available fuel in the machine) and the need to keep the in-vessel tritium inventory within the licensed limit (350 g tritium) due to safety considerations.

1.3 Motivation

In steady state operation of a fusion reactor, only a small fraction of the particles needed to fuel the plasma will be injected from external sources like gas puff, neutral

beam or pellets, the rest of the fuel is expected to enter the plasma via the recycling of the PFMs. This motivates us to understand the recycling mechanism and the related processes in detail. The following points are of main interest

- (i) retention of hydrogen isotopes in graphite and various factors affecting it.
- (ii) chemical sputtering and the flux dependence of chemical sputtering yield.
- (iii) velocity of the hydrogen particles re-entering the plasma in order to calculate the penetration depth.
- (iv) the ratio of re-emitted atoms/molecules in order to derive the flux of the re-entering hydrogen particles from the measurement of H_α light. The photon rates for atoms are in general larger than for the atoms coming from the dissociation of H_2 molecule [22].

1.4 Outline

The main aim of this thesis is to give insight into the physics of the interaction of hydrogen isotopes with graphite in a fusion environment.

The existence of large variations in length scales of sub-structures of graphite coupled with the wide range of possible atomistic processes makes the study of hydrogen transport and inventory in graphite a non-trivial exercise. The key idea is to use the insights gained from the microscopic models for modeling the transport at the meso-scale and further into the macro-scale in order to understand the physical processes contributing to macroscopic transport. Such a multi-scale model was developed by Warriar et al. [1] for modeling the trace hydrogen diffusion problem. This model has been extended in the present thesis by the inclusion of reactions, molecule formation and chemical erosion. The basic computational tools and techniques needed to develop the multi-scale model is described in chapter 2.

The detailed description of the multi-scale model and the parametrization of all the atomistic and molecular processes included in the model is given in chapter 3.

The first physics problem studied in chapter 4 using this multi-scale model is the hydrogen retention and release from the graphite. Special emphasis is given to calcu-

late the ratio of hydrogen released in atomic and molecular form. The interaction of plasmas with atoms or molecules will be different, therefore, it is important to know in which form hydrogen is released. Due to the safety considerations only a small amount (350 g) of tritium is allowed in the machine. Therefore it is important to study the hydrogen retention problem and to quantify the amount of hydrogen retained in the graphite. Formation of hydrogen molecules or hydrocarbons in the graphite is due to the diffusion of hydrogen atoms along internal porosity. It was shown by Warrier [1] that the diffusion coefficient of the hydrogen depends on the internal structure of graphite, viz, void-size and void-fraction, which implies that the molecule formation also depends on these factors. Therefore, the retention and release analysis of hydrogen is performed for samples with different internal structure.

Various other factors affecting retention and release of hydrogen from graphite e.g. energy and flux of the incident hydrogen ion beam play major roles in retention and release behavior. There are many factors which influence the retention and release behavior of hydrogen from graphite and for this reason, different sensitivity studies are performed in chapter 4. Depending on the energy and flux, the incident ion beam creates damage (open bonds) in the graphite. These damage sites are the potential traps for the hydrogen atoms. Standard graphite samples used in the ion-beam experiments have low void fraction ($\sim 5\%$) and trap site density ($10^{-4} - 10^{-5}$ H/C) whereas the co-deposited layers are comparatively porous and have high trapping probability. Using the model developed in this thesis, by varying the trapping probability (or the number of trap sites in the sample) and the internal structure one can model a sample representing standard graphite or a co-deposited layer.

In chapter 5 another application of the multi-scale model, the study of hydrogen retention and release from the deposits collected from the leading edge of the neutralizer of Tore Supra is presented. These deposits consists of micropores with typical size lower than 2 nm ($\sim 11\%$), mesopores (typical size between 2 and 50 nm, $\sim 5\%$) and macropores with a typical size more than 50 nm. This study enables us to understand the kind of voids (micropores, mesopores or macropores) which will be dominant in determining the retention and release behavior from samples having porosity at multiple length scales.

After having understood the hydrogen transport in porous graphite, the next ques-

tion is where does the molecule formation take place? Does it happen at the end of the ion range, which will indicate that molecule formation is a local process, or does it takes place throughout the implantation range (starting from the surface until the end of the implantation zone)? If the molecule formation takes place throughout the implantation range then the isotope exchange reaction can be used as a cleaning (retrieving the retained tritium from the sample) method of a target material saturated with tritium by bombarding it with deuterium or hydrogen. In order to answer these questions the hydrogen isotope exchange reaction in graphite has been studied and is presented in chapter 6.

The consequences of chemical erosion processes are studied in chapter 7. As a first step, a simple 1D-KMC model based on the analytical model proposed by Horn et al. [2] is developed. This is extended to the 3D-KMC model and the effect of the internal structure on the chemical erosion process will be studied.

The flux dependence predicted with the present 3D-model is very weak and no current analytical model can account for the experimentally observed drop in the carbon erosion yield. The molecular dynamics study of Salonen et al. [23, 24] shows that the decrease of the erosion yield at higher fluxes is due to the decreased carbon collision cross section at a surface which had obtained the temporary supersaturation of H atoms due to the extremely high flux involved. Inspired by this study, a simple multi-scale model has been developed to study the flux dependence of chemical erosion and is presented in chapter 8.

Finally, the results are summarized.

Chapter 2

Methods and techniques

In this chapter all the main computational methods which have been used in the simulations presented in this thesis are described briefly. The following methods have been used

- Molecular dynamics (MD)
- Kinetic Monte–Carlo (KMC)
- Monte–Carlo Diffusion (MCD).

2.1 Molecular dynamics

Molecular dynamics (MD) simulates the time dependent behavior of a system of particles. The time evolution of the set of interacting atoms is followed by integrating their equation of motion. MD generates information at the microscopic level: atomic positions, velocities and forces. This microscopic information is then converted to macroscopic observables like pressure, temperature, heat capacity and stress tensor etc. using statistical mechanics.

The essential elements for a molecular dynamics simulation are a knowledge of (1) the interaction potential for the particles, from which the forces can be calculated, and (2) the equations of motion governing the dynamics of the particles. We follow the laws of classical mechanics, mainly Newton’s law,

$$m_i \ddot{\vec{r}}_i = \sum_{i \neq j, j=1}^N -\nabla \Phi_{ij} \quad (2.1)$$

for each atom i in a system constituted by N atoms. Here, m_i is the atom mass, \vec{r} is the position vector of the i^{th} atom and Φ_{ij} is the inter-atomic potential between the i^{th} atom and the j^{th} atom [1].

2.2 Kinetic Monte–Carlo

Any physical situation that can be viewed as a statistical outcome of some basic sub-processes, can be simulated using pseudo random numbers. This can then be characterized as a Monte Carlo (MC) method. MC methods are efficient when a large number of dimensions or complex geometries are involved. They are especially suitable to solve diffusion of a large number of particles in a complex geometry with independent jumps classified as a *standard Wiener process* in literature [25].

Kinetic Monte–Carlo (KMC) is used to simulate the dynamics of a N body system by a stochastic (or random walk) process. Unlike the Metropolis Monte Carlo method, which has been employed to study systems at equilibrium, the KMC method allows to investigate non-equilibrium processes such as diffusion and reactions. The time evolution of the probability density of various events (transitions) that can take place in the system is given by the Master equation. The KMC method provides a numerical solution to the Master equation which is given by

$$\frac{\partial P(\sigma, t)}{\partial t} = \sum_{\sigma'} W(\sigma' \rightarrow \sigma) P(\sigma', t) - \sum_{\sigma'} W(\sigma \rightarrow \sigma') P(\sigma, t) \quad (2.2)$$

where σ and σ' are successive states of the system, $P(\sigma, t)$ is the probability that the system is in state σ at time t , and $W(\sigma' \rightarrow \sigma)$ is the probability per unit time that the system will undergo a transition from state σ' to state σ . At steady state, the time derivative of 2.2 is zero and the sum of all transitions into a particular state σ equals the sum of all transitions out of state σ .

The KMC method can be used to simulate the dynamics of a Poisson–like process provided [26]:

- (i) the events comprising the sequence of processes are independent, i.e. not correlated
- (ii) transitions must satisfy *detailed balance* and a “dynamical hierarchy” of transition probabilities is established
- (iii) time increments upon successful events are calculated properly (as given by eq. 2.4).

2.2.1 The Bortz-Kalos-Lebowitz algorithm

All the thermally activated processes taking place in the system (e.g. diffusion, desorption) are characterized as jumps following an Arrhenius–like relation. Let there be j possible jumps for a particle belonging to the specie i . For each jump

$$\omega^j = \omega_o^j e^{\frac{-E_m^j}{k_b T}} \quad (2.3)$$

where ω^j is the jump rate, ω_o^j is the jump attempt frequency and E_m^j is the height of the energy barrier corresponding to the j^{th} process (Fig. 2.1). For the i^{th} species, let ω_i^j be the jump rate of the j^{th} jump and n_i be the number of particles, then

$$R_i = \sum_{j=0}^{N\text{Jumps}} n_i \omega_i^j$$

is the sum of the rates of all the possible jumps for the i^{th} species.

In the Bortz-Kalos-Lebowitz (BKL) algorithm during each simulation step a particle is picked randomly, but with a probability proportional to its jump rate and the following procedure is followed:

- (i) Initialize the system at $t = 0$
- (ii) Form a list of all the rates r_j of all possible transitions (jumps) in the system
- (iii) Calculate the cumulative function

$$R = \sum_{i=0}^{N\text{Species}} R_i = \sum_{i=0}^{N\text{Species}} \sum_{j=0}^{N\text{Jumps}} n_i \omega_i^j$$

- (iv) Get a uniform random number $U \in [0, 1]$.

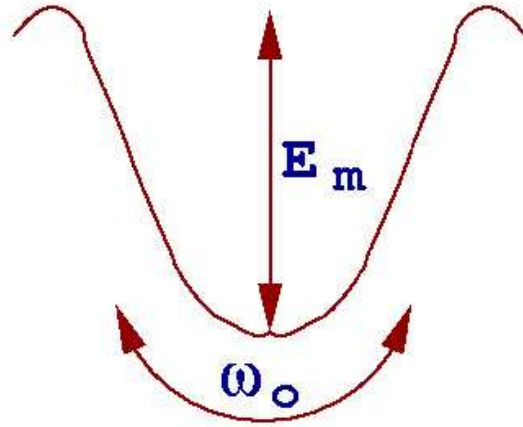


Figure 2.1: A sketch showing the energy E_m needed to overcome the potential well for a thermally activated process. ω_o is the jump attempt frequency for this process.

- (v) Find the event to carry out, i by finding the i for which

$$R_{i-1} < UR < R_i$$

- (vi) Carry out event i .
- (vii) Update those R_i that have changed as a result of event i
- (viii) Get a new uniform random number $U \in [0, 1]$
- (ix) Update the time with $t = t + \Delta t$ where

$$\Delta t = -\frac{\ln(U)}{R} \quad (2.4)$$

and update the KMC step count.

2.2.2 Time dependency in BKL

Within the KMC the time “ t ” is a local quantity for each particle. For simple systems like the example of adsorption–desorption process on a surface used by Fichthron et al. [26] most of the processes taking place in the system have similar migration energies. Therefore, the Δt (given by the BKL algorithm) for the processes is a statistical distribution (similar order of magnitude). Then, with the kind of time increment scheme presented above one can find a statistical “average time” or the “global time”

for the system. Whereas, for a system having very different migration energies leading to several orders of magnitude difference in Δt , it is not possible to define something like a “global time” of the system. This is one of the major drawbacks of the KMC scheme. We take a simple example of the hydrogen atom diffusion in graphite. There are two kinds of jumps a hydrogen atom can make while diffusing on the internal porosity of the graphite, namely diffusion along the internal porosity (migration energy 0.9 eV) and diffusion across the voids (migration energy 1.91 eV). The parametrization of these processes is presented later in this chapter. Fig. 2.2(a) shows the spread of the Δt for these two processes at 500 K.

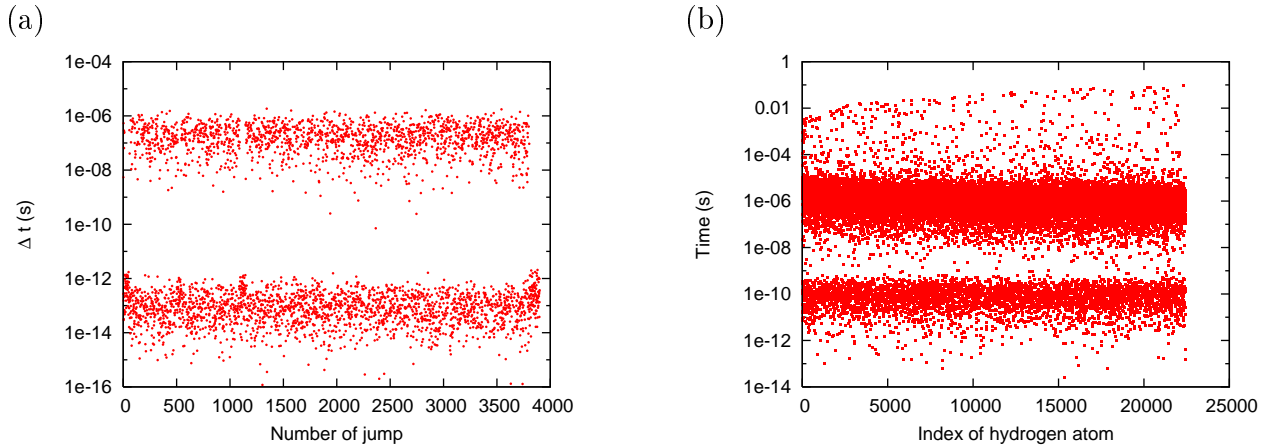


Figure 2.2: Figure showing (a): the spread of Δt for different jumps of the hydrogen atom at 500 K and (b): Real time distribution of different hydrogen atoms after 10^9 BKL steps.

Fig. 2.2(b) shows the time of different hydrogen atoms after 10^9 BKL steps and clearly demonstrates the inability to define a “global time” for the kind of system we intend to study where the migration energies vary from 0.0147 eV (hydrogen atom diffusion within the crystallites) to 4.45 eV (dissociation energy of a hydrogen molecule). As a consequence, time is a local property for each particle in KMC.

2.3 Monte–Carlo–Diffusion

The N–body diffusion equation is given by

$$\frac{\partial n}{\partial t} = \nabla(D\nabla n) + S \quad (2.5)$$

where n is the density, D is the diffusion coefficient of the particles, t is the time variable, S are the sources or sinks in the system, and ∇ stands for the gradient in

3 dimensions. n is determined by the distribution of the N atoms in the simulation volume. The diffusion can be represented as a random walk of N particles with the jump size given by

$$\Delta r = \sqrt{2 D \Delta t} \zeta \quad (2.6)$$

where Δt is the time step and ζ is sampled from a random number distribution satisfying $\langle \zeta \rangle = 0$ and $\langle \zeta^2 \rangle = 1$. This representation is valid for $\frac{D}{\Delta t} \gg \sqrt{2 D \Delta t}$ [1]. The time step Δt is decided within the KMC scheme.

2.4 Implementation of ion flux

A continuous influx of hydrogen atoms determined by the flux of the ion beam was implemented.

$$\Delta N = \phi \times \Delta t \times L_x \times L_y \quad (2.7)$$

where ϕ is the incident flux and L_x , L_y are the system dimensions in X and Y direction respectively. Eqn. 2.7 gives the number of particles introduced into the system (ΔN) in time Δt at the surface ($z = 0$). The time step Δt is decided within the KMC scheme.

2.5 Generation of the 3D porous graphite geometry

An algorithm similar to the one proposed by Graziani [27] was used to create a 3D rectilinear parallelepiped with a specified void fraction and sub-structures having random shapes separated by voids. For a given volume, a Poisson distribution was used to specify the size of a crystallite *element* that has a random shape, orientation and a mean width denoted by the *element-size*. These *elements* are created by populating basic blocks called *cells*. The smoothness of the *element* depends on the *cell-size*. After each populating event the remaining void fraction is checked and the process is repeated if the void fraction is equal to that specified. For more details about the algorithm used for generating the porous structure see [1].

For example a porous structure of $3 \times 10^{-7} m$, $3 \times 10^{-7} m$, $1 \times 10^{-7} m$ in X, Y and Z direction respectively, representing a typical granule with periodic boundary conditions

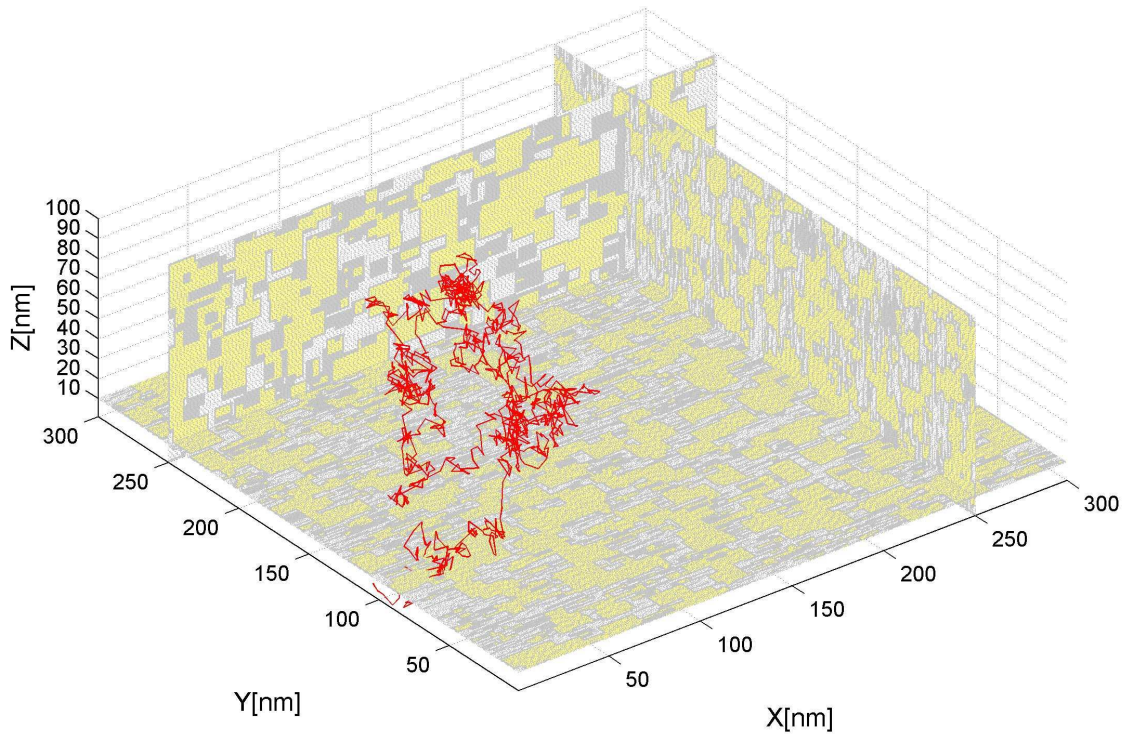


Figure 2.3: The porous structure of graphite. Light yellow color: bulk, grey: surface and white: void. The red line shows the random walk trajectory of a hydrogen atom.

in X and Y direction was created. The basic cell size was $1 \times 10^{-9} m$. The graphite sample was composed of the combination of the two kinds of voids

(i) smaller voids of size $1 \times 10^{-9} m$, $1 \times 10^{-8} m$, $1 \times 10^{-8} m$ (11%)

(ii) larger voids of size $1 \times 10^{-8} m$, $1.8 \times 10^{-8} m$, $1.8 \times 10^{-8} m$ (5%)

in X, Y and Z directions respectively. Fig. 3.3 shows a cut of the porous graphite structure specified above. The random walk trajectory of a diffusing hydrogen is also shown in the 3D view.

2.6 Recap

The main computational methods which are used in the model to simulate the reactive–diffusive transport of hydrogen in graphite have been described. A tool has been developed that can generate a 3D porous structure with a given void fraction and void size. It will help us to study the reactive–diffusive transport of hydrogen in graphite and the effect of the internal structure on it.

Chapter 3

Multi-Scale Scheme

Multi-scale modeling and computation has recently become one of the most active research areas in applied science. With rapidly growing computing power, we are increasingly more capable of modeling the details of physical processes. Nevertheless we still face the challenge that the phenomena of interest are often the result of strong interaction between multiple spatial and temporal scales, and the physical processes are described by radically different models at different scales.

In order to understand this let us take example of the problem being addressed here, i.e. reactive-diffusive transport of hydrogen in porous graphite. The graphite used in fusion devices consists of granules (typically 1-10 micrometer) separated by voids which are typically a fraction of a micrometer. The granules consist of graphitic micro-crystallites of size 10-100 nm separated by micro-voids which are typically one nm [11, 12]. The existence of such large variations in length scales of sub-structures coupled with the wide range of possible atomistic processes (Chapter 1) makes the study of hydrogen transport and inventory (or complementing this, the formation of hydrocarbons and their transport) in graphite a non-trivial exercise.

In the present work following nomenclature have been used for different length scales:

- micro-scales: void size $< 2 \times 10^{-9} m$ and system dimension of several $10^{-9} m$.
- meso-scales: void size $< 10 \times 10^{-9} m$ and system dimension of several $10^{-7} m$.
- macro-scales: void size $> 50 \times 10^{-9} m$ and system dimension of several $10^{-6} m$.

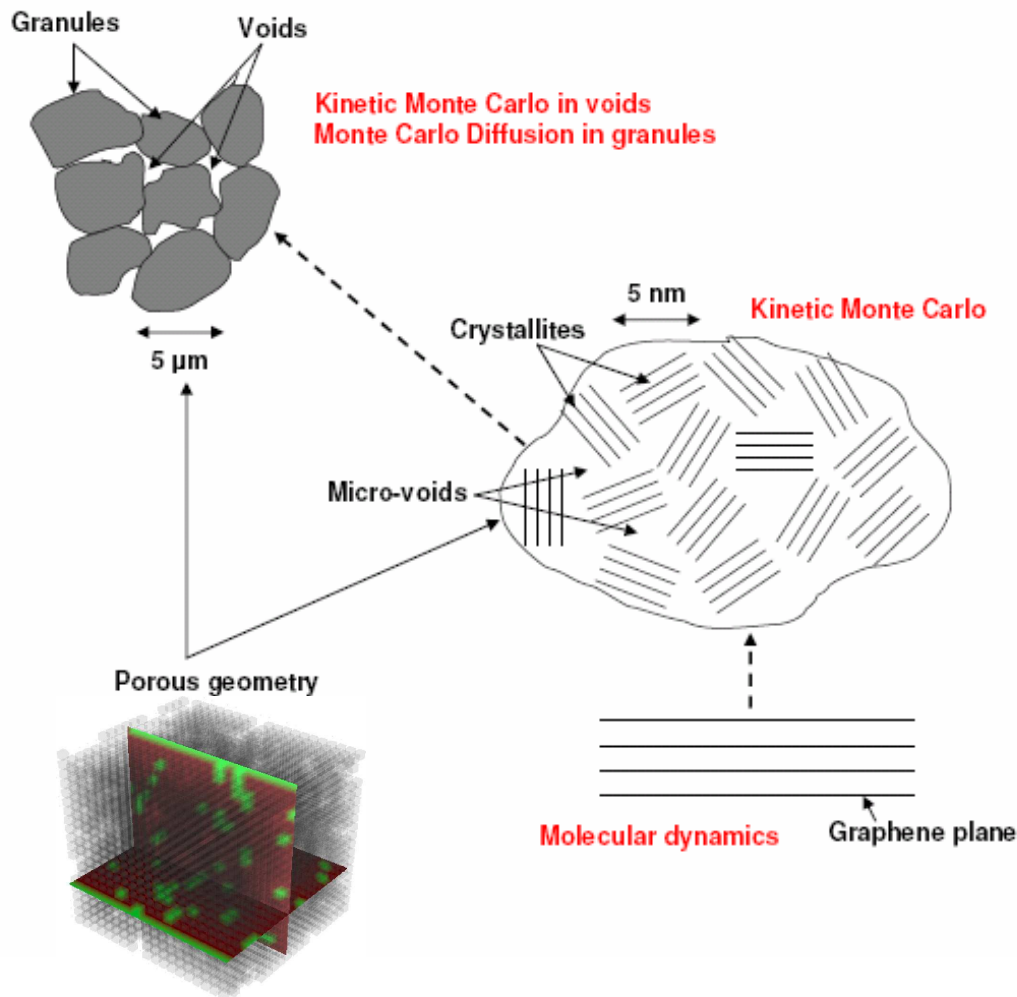


Figure 3.1: Multi-scale schematic.

Many detailed macroscopic models have been proposed to study hydrogen isotope inventory and transport in porous graphite [28, 29, 30, 31] and hydrocarbon formation and transport in graphite [5]. These models use rate constants for transport from experiments [32, 33, 34, 16, 35, 36], some of which still need theoretical explanations and

lacks the micro-structural information that gives us the understanding of the microscopic mechanisms which eventually contributes to the macroscopic behavior. There exists many microscopic models [37, 38, 39, 40] using MD with either empirical potentials or density functional theory and they give insight into the microscopic mechanisms studied in graphite. These microscopic models allows us to probe the detailed atomistic mechanisms. However, the length and time scales of interest are often far beyond what a full atomistic computation can reach. This is where multi-scale modeling comes into play. The idea is to use the insights gained from the microscopic models for modeling the transport at the meso-scale and further at the macro-scale in order to understand the physical processes contributing to macroscopic transport. By using this philosophy of multi-scale modeling, one is able to develop numerical tools that takes into account the physics happening at the micro-scale and the efficiency that is comparable to the macroscopic models.

Warrier et al. [1] have modeled hydrogen isotope diffusion in pure, crystal graphite using MD at micro-scales ($2.5 \text{ nm}, 10^{-10} \text{ s}$) and consistently parametrized the MD results within a KMC scheme [40]. A 3D, porous, granule structure was constructed using statistical distributions for crystallite dimensions and crystallite orientations for a specified micro-void fraction. The KMC scheme was extended to include trapping and detrapping at the crystallite-micro-void interface in the 3D porous granule structure to simulate trans-granular-diffusion (TGD) in the meso-scales ($10^{-7} - 10^{-6} \text{ m}$, several ms) [41] using the results from micro-scale modeling and from experiments ([42] and references therein). Later, this concept was extended in the simulations to the macro-scales (1 cm , up to a few s), thereby having a truly multi-scale capability.[43].

In the present work, the model proposed by Warrier et al. [1] was extended. The following features have been added to the existing model

- (i) Introduction of molecular species. This implies the inclusion of the following reactions
 - recombination
 - dissociation
 - trapping (based on predefined trap site distribution or trapping probability)

- (ii) implementation of a continuous influx of hydrogen atoms determined by the flux of the ion beam
- (iii) implementation of the model for the chemical erosion based on the Küppers–Hopf cycle [44].

The above mentioned features added to the model changes the characteristics of the code from a “trace atom diffusion” code to a “reactive–diffusive” code.

3.1 Parametrization of the processes

All the processes taking place in the system have been parametrized for KMC, in terms of the jump attempt frequency ω_o^j , the migration energy E_m^j , and the jump distance L_j [1]. The jump distance L_j corresponds to the distance jumped by an atom or molecule in a specified direction after overcoming the j^{th} energy barrier with migration energy E_m^j . The input parameters have been taken from molecular dynamics simulations and experiments. Various processes which have been included in the simulations for the hydrogen recycling problem are described. A two–region model is implemented distinguishing for atoms or molecule transport processes within the bulk and surface region on the graphite crystallites. Hydrogen atoms and molecules within the crystallites and in the voids are treated as different species and have different transport behavior due to the fact that they experience different chemical surroundings.

3.1.1 Hydrogen atoms

In the present model following processes have been included for the hydrogen atoms (see also [11, 29])

- Diffusion within the crystallites
- Surface diffusion
- Trapping–detrapping
- Going into the bulk
- Desorption
- Recombination

Diffusion within the crystallites

Chiu and Haasz [45] found that there exist two different diffusion channels for the hydrogen transport in the crystallites, with different migration energies and pre-factors. They speculated that this was due to the diffusion of hydrogen atoms along graphite planes within the crystallites at low temperatures (<500 K), whereas at higher temperatures (>500 K) diffusion (perhaps through defects) could occur perpendicular to the planes. They observed a difference in the release of HD molecules when a pseudo-monocrystal graphite, preimplanted with 1 keV D^+ , was bombarded with 10 keV H^+ perpendicular or parallel to the graphite planes. This indicates an inhibited diffusion across the planes, but a free diffusion along the planes at room temperature. The MD studies by Warriier [1] reveals that two channels do exist but there is no diffusion across the graphene layers and the diffusion is isotropic in the plane of the graphene layers. Phonon vibrations of the graphene layers show a large amplitude at higher temperatures (>450 K). This allows the hydrogen interstitials to sneak through the large openings between the graphene layers and by interaction with the phonons, allowing longer jumps. Atoms in the crystallites can have either short (0.015 eV, 0.38 nm, $6.8 \cdot 10^{12}$ s $^{-1}$) or long (0.269 eV, 0.1 nm, $2.74 \cdot 10^{13}$ s $^{-1}$) jumps [1].

Surface diffusion

Causey et. al. studied the retention of deuterium and tritium in graphite (POCO AXF-5Q) using the nuclear analysis reaction (NRA) technique. Three temperature regimes were studied separately in order to understand the processes which get dominant around those specific temperatures. At 500 K and below, plasma exposure results in the saturation of the implant region and very high surface coverage. The overall retention in this temperature range is limited because the hydrogen isotopes are practically immobile, both on the surface and in the grains. For temperature between 500 K and 1000 K, hydrogen isotopes become mobile and start diffusing along the pore surfaces, reaching deep into the sample. Above 1000 K, hydrogen isotopes begin to enter the graphite grains and occupy the high energy traps. Studies using the BET¹ adsorption technique proved that most of the internal porosity of the sample was interconnected. The surface diffusion coefficient calculated from the diffusion profiles at 573 K and 773 K was found to be $D = 1.2 \exp(-0.9 \text{ eV}/kT) \text{ cm}^2/\text{s}$.

¹a gas adsorption technique devised by Brunauer, Emmett and Teller (BET) to measure the specific surface areas of the materials.

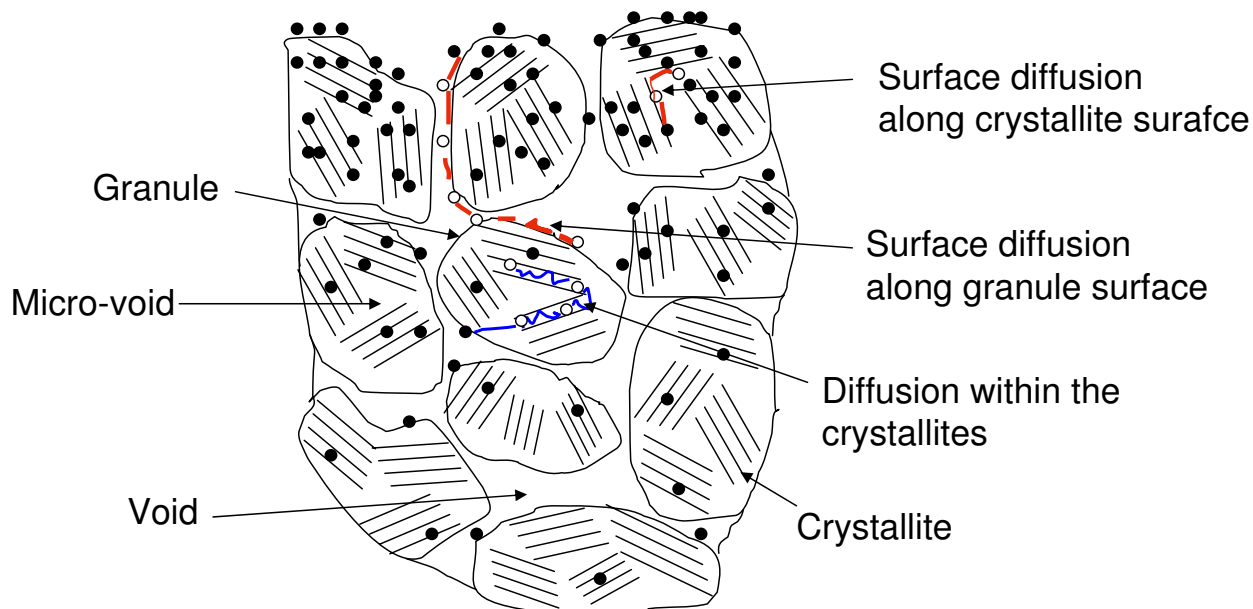


Figure 3.2: Sketch of the different diffusion channels of the hydrogen atoms.

In the present simulations the activation energy for the surface diffusion is taken to be 0.9 eV with a jump attempt frequency of 10^{13} s^{-1} (typical phonon frequency). Diffusion coefficients are usually published [15, 42] in the form

$$D = D_o e^{\frac{-E_m}{k_B T}} \quad (3.1)$$

with units of *length*²/*second*, D is the diffusion coefficient and D_o is called the pre-factor of the diffusion coefficient. Within the trapping-detrapping limited diffusion

regime, this can be interpreted as

$$D = \omega_o L^2 e^{\frac{-E_m}{k_B T}}. \quad (3.2)$$

The physical meaning of D_o is obvious from eqn.3.1 and eqn.3.2. It is the product of the number of jump attempts to detrapp, ω_o , and the square of the length jumped, L^2 , after a detrapping event [1]. So a jump length of 34.64 Å was used to match the surface diffusion coefficient of $D = 1.2 \exp(-0.9 \text{ eV}/kT) \text{ cm}^2/\text{s}$. This jump length of 34.64 Å is the maximum distance that can be covered by a hydrogen isotope diffusing along the internal porosity of the sample. However the actual distance covered depends on the details of the local internal structure where the atom is present.

Detrapping

The atoms diffusing along the internal porosity can get trapped at the trapping sites (open carbon bonds). It is estimated that the trap site concentrations within the bulk graphite are of the order 10^{-3} to 10^{-5} per C atom [46, 15]. Graphites exposed to fusion edge plasmas also get damaged by the incident energetic ions and neutrals from the plasma and this causes a high density of trap sites within the range of penetration of the incident ions ([29, 46] and references therein). The trapping event is not a thermally activated process [29]. In the present work two possible ways for an atom to get trapped have been investigated. One possibility is to distribute a predefined number of trap sites and treat trapping as a recombination event between a solute hydrogen atom and a trap site. The other possibility is to define a trapping probability and whenever an atom jumps along the surface it has some probability to get trapped. The trapped atoms can get detrapped with a jump attempt frequency of $\sim 1 \times 10^{13} \text{ s}^{-1}$ and a detrapping energy between 2.6 and 4.3 eV [42].

Kanashenko et al. [47] and Chernikov et al. [48] have suggested that two kinds of trapping sites exist in graphite, a low-energy site (2.3 eV) and a high-energy site (4.4 eV). The low-energy sites corresponds to 'usual C atoms at the edge of crystallite' due to their energy, and the high-energy sites correspond to 'submicroscopic interstitial clusters'. The concentration of low-energy trapping sites should be much higher in graphite, on the other hand, the number of high energy trapping sites increases with the energetic ion or neutron irradiation of the graphite sample. However they concluded that the major contribution to the trapping comes from the trapping sites present at

the edge surface of the crystallites. Later these values were verified by the desorption experiments by Atsumi et al. [49]. The jump length of 0.3 nm was chosen in order to match the reported diffusion coefficient in the trapping–detrapping limited regime [1].

Going into the bulk

At low temperatures (< 1000 K) hydrogen atoms adsorbed on the granule-void interface diffuse along the granule surface and thus can penetrate much beyond the implantation range. As the temperature increases the hydrogen atoms starts entering into the granules. Federici et al. calculated the energy needed for an atom to enter into the granules using their theoretical model TIPO [30]. The energy required to enter into the granule (E_A) depends on the adsorption energy of a H_2 molecule (E_c), the desorption energy of a H_2 molecule (E_D), the solution energy of the atom (E_s) and the diffusion energy of the atom (E_d). Using the relation

$$E_A = \frac{E_D}{2} + E_d - \frac{E_c}{2} + E_s \quad (3.3)$$

gives $E_A \sim 2.67$ eV. In terms of KMC this process has an energy barrier, a jump attempt frequency and a jump length of 2.67 eV, 0.3 nm and $1.0 \times 10^{13} \text{ s}^{-1}$ respectively.

Desorption

The hydrogen atoms which are adsorbed on the normal graphite lattice can be desorbed from the surface via thermal desorption process. Ashida et al. [50] found the desorption energy of hydrogen isotopes from pyrolytic samples using thermal desorption spectroscopy (TDS). It was found to be 1.91 eV for the three isotopes of hydrogen. The desorption process obeys a second order kinetics, indicating that the rate determining step is the surface recombination reaction of hydrogen atoms. In terms of the KMC parametrization, the jump attempt frequency of $1 \times 10^{13} \text{ s}^{-1}$ and the jump length of 0.2 nm was chosen.

Recombination

A hydrogen atom diffuses along the internal porosity and after coming closer than a certain cutoff distance to another hydrogen atom adsorbed at the surface, they can recombine to form a hydrogen molecule. A solute hydrogen atom can also recombine with a trapped hydrogen atom to form a trapped hydrogen molecule. A Smoluchowski

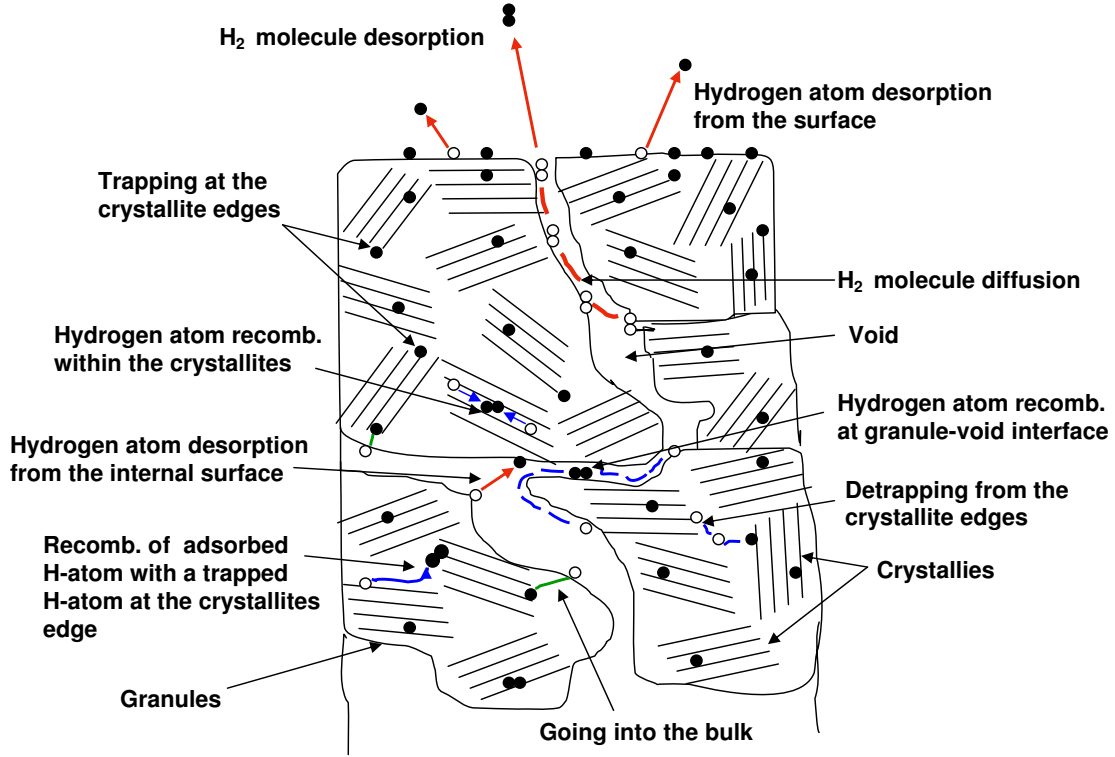


Figure 3.3: Sketch of the different kinds of jumps and events possible for the hydrogen atoms and molecules.

boundary condition [51] is used to model specie recombination in the code. This is achieved by checking the distance of hydrogen atoms. If the distance between two hydrogen atoms gets smaller than a certain distance r_o they recombine to form hydrogen molecules. This is equivalent to having a step potential well for interaction of the species at a radial distance r_o . Such boundary condition is valid for the cases with strong binding energies (like hydrogen recombination or hydrogen trapped at the open bond site) where reflection becomes a rare event once the atom gets closer than a cutoff distance [52].

However Haasz et al. [29] treated recombination as thermally activated process and have parametrized it using the classical equation for recombination

$$\kappa_{ss} = 8\pi\Delta_s R_{ss} N_c. \quad (3.4)$$

where κ_{ss} is the recombination coefficient, Δ_s is the surface diffusion coefficient,

N_c is the atomic density of the graphite crystallites (of the order of $10^{29} C/m^3$) and R_{ss} is the radius of recombination. Deusing et al. [53] reported $R_{ss} \sim 0.2$ nm. Even though in the KMC parametrization presented here recombination was not treated as a thermally activated process, temperature dependence on recombination rates comes through the diffusion coefficient of atoms, which is temperature dependent.

It has been observed that the recombination rate depends on the internal structure of the sample and is facilitated by the higher internal porosity, along which the atoms can diffuse and eventually recombine to form molecules. Eq. 3.4 does not include any dependence of the recombination rate on the internal structure of the sample. In the present work the recombination process was parametrized for a given internal structure of the sample at the meso-scale and was used as an input parameter for scaling up to macro-scale.

As mentioned above, there is no “global time” for the present system in KMC ansatz and time is a local property for each particle. Therefore, in order to quantify the recombination rate, each particle is followed and assigned a local time separately (adding Δt to the local time of this particular particle every time it makes a jump). When a recombination event takes place the maximum of the times of the two recombining particles is taken ($t_{recomb.}$, the time spent by the particle in the system before it recombines). The quantity $1/t_{recomb.}$ gives the recombination rate for one recombination event. Similar procedure is followed for the other recombination events too and finally an average is taken of all $1/t_{recomb.}$'s. This quantity was used as the average recombination rate.

3.1.2 Hydrogen molecules

The different processes for hydrogen molecules considered in the model are

- Diffusion
- Dissociation
- Desorption
- Detrapping

Diffusion

Diffusion of hydrogen atoms within the crystallites leads to recombination events and hydrogen molecules are formed. The inter-layer spacing between two graphene planes is ~ 0.335 nm, therefore, due to the size of the H_2 molecules, their diffusion within the crystallites is extremely slow. In KMC a very high migration energy (4.06 eV) is chosen for this process. The jump frequency and jump length for this process are $1 \times 10^{13} \text{ s}^{-1}$ and 0.1 nm.

The hydrogen atoms diffusing along the crystallite–microvoid interface (CMI, at mesoscales) or along the granule–void interface (at macroscales) form molecules and the resulting molecules can diffuse very easily due to the presence of large voids. This is due to the fact that the material is subjected to a high level of radiation damage, which results in the formation of a complicated network of different carbon–carbon and carbon–hydrogen bonds. This network might well contain open paths to the surface on a sub–nanometer scale, which render possible a fast out-diffusion of molecules [54]. The hydrogen molecule diffusion was assumed to be very fast (above room temperature), which is supported by the immediate drop of the H_2 re-emission signal when a H^+ beam is turned off [29]. So for the hydrogen molecules to jump through the voids the KMC parameters are 0.06 eV, 0.2 nm and $1.0 \times 10^{13} \text{ s}^{-1}$.

Dissociation

The energy needed for the dissociation of a hydrogen molecule in graphite is around 4.48 eV [49]. The jump attempt frequency is $1.0 \times 10^{13} \text{ s}^{-1}$ and a jump distance of 0.2 nm is used. Due to the very high energy barrier this process is less probable.

Desorption

Due to the fact that a hydrogen molecule is a chemically inactive species the desorption process is considered to have no energy barrier. So, as soon as a diffusing hydrogen molecule reaches the geometrical surface, it is released.

Detrapping

The solute hydrogen atoms diffusing along the inner surface may get trapped at the crystallite edges. A trapped hydrogen atom having another trapped hydrogen atom

in the close vicinity (within the recombination radius of the trapped atom) have been identified as a specie consisting of two trapped hydrogen atoms close enough to form a hydrogen molecule. The energy needed to detrap two hydrogen atoms to produce a hydrogen molecule is estimated to be 4.4 eV, however Atsumi et al. [55] proposed that the carbon atoms at the edge surface in the ordered graphite structure induces a relaxation between neighboring atoms, thus reducing the activation energy for detrapping of a hydrogen molecule to 2.3 eV. After the detrapping process the resulting solute hydrogen molecule can diffuse through the inner porosity and get desorbed. In the presented model, for this process the migration energy of 2.3 eV, jump frequency of $1.0 \times 10^{13} \text{ s}^{-1}$ and jump length of 0.4 nm is used.

Within the KMC ansatz, all attractive potentials were considered as traps, be it either covalent bonding or adsorption. Therefore, the term trap was loosely used for even adsorption events. The energy for an atom to (i) detrap, (ii) dissociate or (iii) desorb was referred to the migration energy. This was because any of these events leads to a migration of the trapped atom.

The present model simulates the reactive-diffusive transport of the thermalized hydrogen in graphite. The collisional cascade effects were taken into account by using a depth distribution corresponding to the range of the incident ions as calculated with TRIM.

3.2 Recap

All the atomistic processes needed to describe the hydrogen transport in porous graphite have been identified. The information gained from MD studies and experimental database have been used to parametrize the atomistic processes in terms of the KMC parameters ω_o^j , E_m^j and L^j . Using these, one has a 3D model which is capable of simulating the reactive-diffusive transport of hydrogen at multiple length and time scales.

In the next chapter the code developed here is benchmarked with respect to the experiments and the model is applied to understand different factors affecting the hydrogen retention and release from porous graphite sample. These are two of the

main questions to be addressed for studies of interaction of hydrogen plasmas with carbon. After having answered these two questions we can proceed to study the isotope exchange and chemical erosion problem.

Chapter 4

Hydrogen retention and release from porous graphite

The understanding of retention and release processes of hydrogen and its isotopes in graphites and carbon-based materials is essential to plasma density control and tritium inventory considerations in ITER. Various studies and experimental databases to understand the hydrogen retention and release from graphite can be classified into two regimes. First, ion beam experiments, which are carried out using energetic ion beams having energies and fluxes of the order of few keV and 10^{19} *ions/m²/s* respectively. Second, tokamak experiments where the ion energies close to the divertor region are a few eV to a few hundreds eV and the ion fluxes are very high $\sim 10^{21} - 10^{24}$ *ions/m²/s*. Both of the scenarios have been studied in the simulations presented here. The different conditions make extrapolation of beam scenarios to fusion devices very problematic and modeling allows to overcome these problems.

In this chapter the multi-scale model presented before (chapter 3) has been validated against the well diagnosed ion-beam experiment performed to study the plasma-surface interaction at KFA Jülich [56]. The validated model can then be used to extrapolate and analyze the hydrogen transport in fusion conditions. The hydrogen retention and release behavior from porous graphite sample has been presented for the ion-beam regime. Various factors affecting retention and release of hydrogen from graphite have been studied. It is shown that the internal structure of the graphite (void fraction, void size and void orientation), the energy of the incident hydrogen ion beam and the flux play major roles in retention and release behavior.

4.1 Validation of the model

For validating our model, an experiment used to study the plasma–surface interaction at KFA Jülich [56] was simulated. Graphite samples were bombarded by a 3 keV H_3^+ ion beam at normal incidence. The ion beam had a fluence of $10^{18} H/cm^2$. Re-emitted particles were directly detected by a two–stage differentially pumped line–of–sight quadrupole mass spectrometer. Several data points were presented for each temperature in order to document the scatter in the data. The material chosen in the experiment was EK98 (Ringsdorff, FRG), an isotropic, porous, fine grain graphite with the density $1.85 g/cm^3$. This gives an estimate of the void fraction of about 12% (density of standard graphite is about $2.09–2.23 g/cm^3$).

The number of hydrogen atoms and trap sites were specified according to a Gaussian profile based on the energy of the ion beam simulated and then the evolution of the system was followed. The amount of hydrogen released and retained in the sample was calculated. From the released amount of hydrogen the fraction of hydrogen released in the form of atoms and molecules were calculated. This quantity is very important to know because in experiments, flux of the re–entering hydrogen particles is derived from the relative fraction of the hydrogen released as atoms and molecules.

4.2 Setting up the simulation

It was shown by Warrior [1] that the diffusion coefficient of the hydrogen depends on the internal structure of graphite, viz, void–size and void–fraction, which implies that the internal structure of the graphite plays a major role in the retention and release behavior (shown later in this chapter). Therefore, a parameter scan over different geometries of the graphite was done and it was found that the following geometrical configuration gives the best agreement with the experiment. The basic cell size was 0.5 nm. The graphite sample chosen for this case was a cube of $100 nm \times 100 nm \times 100 nm$ having a void fraction $\simeq 10\%$ and a void size $1 nm \times 10 nm \times 10 nm$ in x, y and z directions, respectively. The geometrical surface lies at $z = 0$.

The typical ion beam energies considered in the simulation spans from 1–3 keV. The profile of the ions as given by TRIM calculations was approximated to a Gaussian

distribution with a range of penetration of 27.5 to 59.0 nm and a standard deviation of 8.0 to 12.0 nm along the z -direction. The full width at half maximum of the distribution is 16.0 to 24.0 nm. Initially 2000 hydrogen atoms were distributed in the system. The basic cell size was 0.5 nm. This implies that an ion beam having an energy of 1 keV was centered around the 55th cell from the surface covering around 16 cells on both sides. Due to the short mean free path of hydrogen atoms (fraction of a nanometer) it was sufficient to concentrate on the transport mechanisms in the trans-granular level (within one granule with dimensions about 100 nm or 200 cells in z -direction) for retention and release studies. A Poisson distribution was used to create the geometry and there were closed as well as open pores in the sample. Closed pores are the voids which are not directly connected to the surface, whereas open pores are directly connected to the surface.

4.3 Results

Fig. 4.1 shows the released amount of hydrogen as a function of temperature. From the total released amount the fraction contributed by atoms and molecules is plotted on the Y-axis. Out of 2000 hydrogen atoms distributed initially in the sample around 10% hydrogen is released at 900 K, increasing to 70% at 1500 K and finally saturating around 87% at 2100 K. The released amount of hydrogen at different temperatures can be found from the corresponding retention curve (Fig. 4.2). The hydrogen release curve follows the experimental results of [56] and the model calculation of [29], *i.e.* the released flux is mainly molecular hydrogen at lower temperatures and atomic hydrogen at higher temperatures.

At lower temperatures (< 700 K), the desorption energy of the hydrogen atoms is too high (1.9 eV) for H atom release. However, it diffuses along the surface (migration energy 0.9 eV) and recombines to form hydrogen molecules. These molecules have a very low desorption energy (0.06 eV) and almost immediately diffuse to the surface and are thermally released. As the temperature increases, H atomic desorption from the internal surfaces also becomes an important process and we begin to observe atomic hydrogen release too. Since atomic hydrogen release occurs, there are lesser hydrogen atoms available for molecule formation and this results in a fall of molecular hydrogen release at higher temperatures.

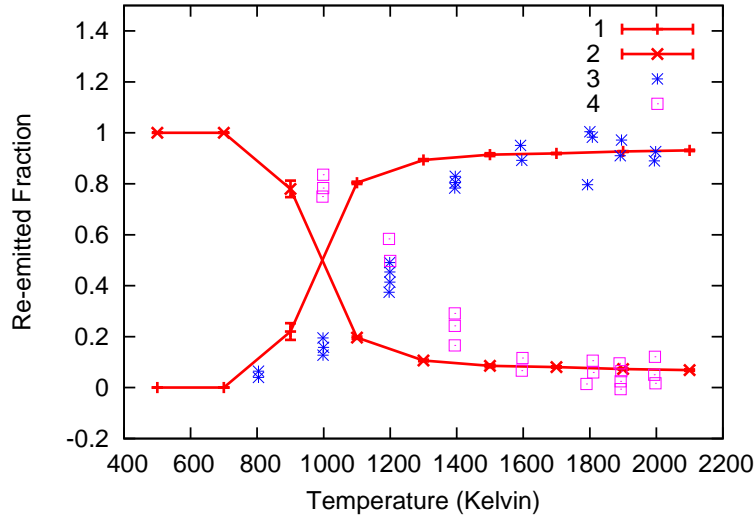


Figure 4.1: Released amount of hydrogen atoms and molecules. Lines: model calculations from present work (1: H-atom, 2: H_2 -molecule), points: data obtained from experiments, ref. [56] (3: H-atom, 4: H_2 molecule). The fluence in the present work was $2 \times 10^{13} H/cm^2$ and in the experiment of Franzen et al. (ref. [56]) was $6 \times 10^{18} H/cm^2$. Out of 2000 hydrogen atoms distributed initially in the sample around 10% hydrogen is released at 900 K, increasing to 70% at 1500 K and finally saturating around 87% at 2100 K.

The released flux depends on the competition between diffusion, recombination and trapping–detrapping which further depends on the internal structure of the graphite. Graphite samples having different internal structure offer different amounts of inner surface area, which determines the amount of passage offered to hydrogen atom for diffusion towards the real surface or deep into the bulk and thus affect release and retention behavior, respectively. The inner surface area of the sample also determines the recombination and trapping probability. The higher the inner surface area offered by the sample, the higher is the probability for recombination or trapping.

The temperature at which both atomic and molecular hydrogen are released in equal amount ($T_{50\%}$) is shifted about 200 K towards lower temperatures in our results compared to experiment. This is due to the fact that the amount of released atoms or molecules depend on the incoming flux. This shift was explained earlier already by Haasz et al. [29] and is due to the different flux value in our calculation (see figure caption 4.1). The released flux is basically determined by the competition of the second–order process of recombination with the first–order process of atomic hydrogen diffusion and release. In our simulation it was observed that with increasing the initial

number of hydrogen atoms in the system, $T_{50\%}$ shifts towards higher temperatures and considerable amount of about 20 – 30% of the released hydrogen is released in molecular form even at higher temperatures. This point is discussed later, when we present the analysis of the dependence of the incident flux on the release characteristics.

The retention of hydrogen in graphite is not limited to the ion implantation range. Due to the diffusion of the implanted hydrogen along the internal porosity surfaces, hydrogen can penetrate deep inside the bulk well beyond the implantation zone. A graphite sample exposed to a hydrogen ion beam retained all of the incident ion and no saturation was observed till about $10^{17} H^+ /cm^2$ [57].

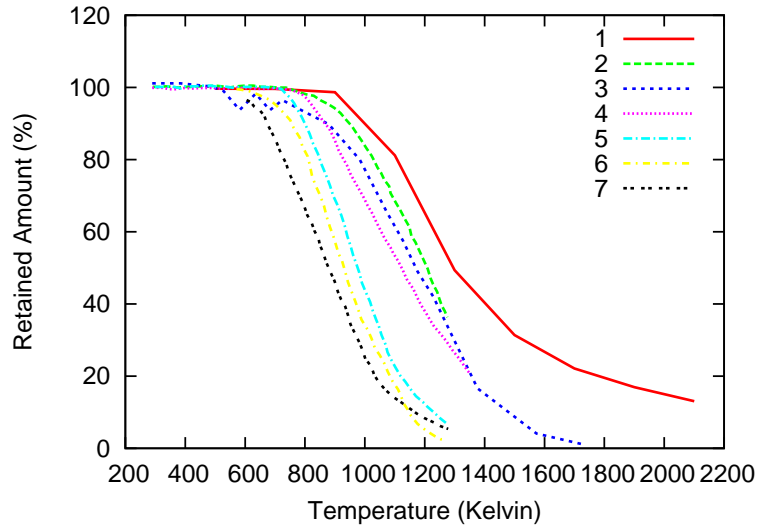


Figure 4.2: Amount of retained hydrogen as a function of temperature for different fluences. Data obtained in this work (curve 1, 1 keV, $2 \times 10^{13} H/cm^2$) is compared with the retention data reported by Braun et al. [58] (curve 2, 20 keV, $8 \times 10^{16} D^+ ions/cm^2$), Sawicki et al. [59] (curve 3, 40 keV, $5 \times 10^{15} HT ions/cm^2$), Doyle et al. [60] (curve 4, 1.5 keV, $10^{16} D^+ ions/cm^2$), Scherzer et al. [61] (curve 5, 1.5 keV, $5 \times 10^{17} D^+ ions/cm^2$), Braun et al. [58] (curve 6, 20 keV, $9 \times 10^{18} D^+ ions/cm^2$), and Langley et al. [62] (curve 7, 8 keV, $10^{18} D atoms/cm^2$).

It was shown that the retained amount of hydrogen in graphite depends on the temperature of the sample, the fluence of the ion beam and the type of graphite used. Fig. 4.2 shows the retained amount of hydrogen as a function of temperature. Results from other references [59, 58, 60, 61, 62] are also presented for comparison. At lower temperatures, the retention is practically 100% and as the temperatures increases, hydrogen is released and the retained amount reduces to about 5%. As discussed before, at lower temperatures, practically all the hydrogen present in the sample is in the form

of trapped hydrogen and the probability of a detrapping event is very low. Even if some detrapping event takes place the resulting solute hydrogen atom gets re-trapped in its course of diffusion and therefore most of the hydrogen is retained in the sample and nothing is released. Whereas at higher temperatures the detrapping starts and the diffusion coefficient of hydrogen also increases. This high mobility of atoms leads to higher desorption and lower retention values.

As observed by Sawicki et al. [59], the retention characteristics depend strongly on the incident fluence and follows a regular trend. At a given temperature, for low fluences, the concentration of atomic hydrogen on the inner surfaces is lower. Therefore the recombination probability decreases. This gives rise to a reduced molecular hydrogen formation and lower desorption *i.e.* higher retention levels. Also, the longer the duration of the bombardment (higher fluence) the more time is available for hydrogen to diffuse. Consequently, the probability of an out-diffusing hydrogen atom to be released or recombine is higher which leads to higher desorption *i.e.* lower retention levels.

Other parameters like internal structure, trapsite density, energy of the incident ion beam, also affect retention and release of hydrogen from graphite and it is a difficult task to identify the effect of those experimentally. The simulations offers a much easier tool for this. For this reason, different sensitivity studies were performed.

4.3.1 Effect of the range of penetration of incident ion beam

Fig. 4.3 shows the effect of the ranges of penetration on the hydrogen release behavior. Ion beams with ranges of penetration of 27.7 nm (energy \simeq 1 keV), 37.5 nm (energy \simeq 1.7 keV) and 47.5 nm (energy \simeq 2.4 keV) were used. The retained amount for all these simulation cases are given in Fig. 4.4 and one can find for each temperature the exact amount of hydrogen released from the retained amount ($100\% - \textit{retained amount}\%$).

The results agree well with those of Haasz et al. [29]. It is seen that as the energy of the incident ion beam is increased (which also means an increase in range of penetration) a larger fraction of hydrogen is released in molecular form than in atomic form. The higher the energy of the incident ion beam, the deeper it can penetrate. This results in a higher probability for atoms to recombine on an inner surface before

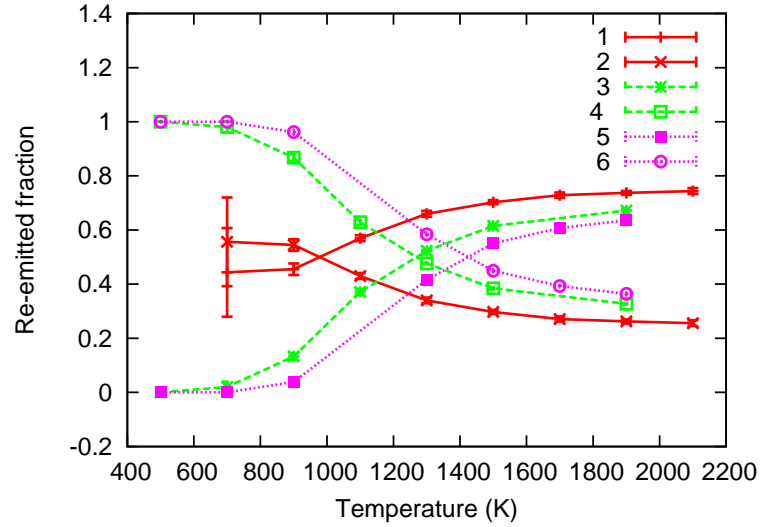


Figure 4.3: Released amount of hydrogen atoms and molecules as a function of temperature for different depths of penetration. Curve (1,2), (3,4) and (5,6) represents (H, H_2) for ion range of 27.5 nm, 37.5 nm and 47.5 nm respectively.

they reach the real surface due to increased diffusion paths, thereby increasing the possibility of molecule formation.

Also, the temperature at which both atomic and molecular hydrogen are released in equal amount ($T_{50\%}$) is lower for an ion beam with a low range of penetration and the release of hydrogen in atomic form starts at lower temperatures. The closer the hydrogen atoms are distributed with respect to the real surface of hydrogen the easier it is for them to diffuse out and to reach the real surface without being trapped and recombined. The hydrogen release characteristics are governed by the competition between trapping–detrapping, recombination and desorption.

Fig. 4.4 shows that the net level of retention is higher in the case of an ion beam with higher energy as the specimen temperature is increased. This is expected, because the deeper the ions penetrate until thermalization, the higher is the probability of getting trapped at trapping sites available at the CMI (Crystallite Micro-Void Interface) before reaching the real surface for release leading to higher retention levels. This figure is consistent with Fig. 4.3.

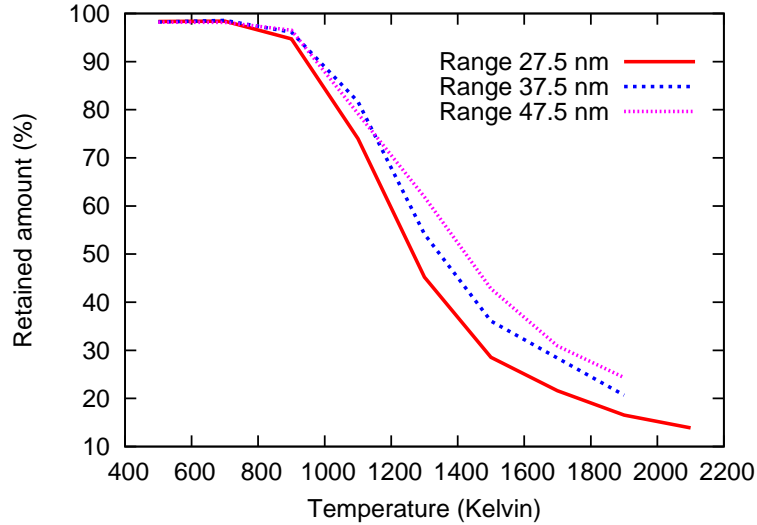


Figure 4.4: Amount of retained hydrogen as a function of temperature for different depths of penetration.

4.3.2 Effect of incident flux

Fig. 4.5 shows the effect of the incident flux on the re-emission behavior of hydrogen. The temperature at which both atomic and molecular hydrogen are released in equal amount ($T_{50\%}$) shifts towards higher temperatures by increasing the flux and a large fraction of molecules are released even at higher temperatures. With increasing flux, the density of trapped and mobile hydrogen atoms on the inner surfaces increases. This gives rise to higher recombination probability and reduces the probability of a diffusing hydrogen atom to be released in atomic form. Even at very high temperatures, detrapping takes place, however, due to the very high probability of being recombined, the hydrogen release in atomic form is less probable as compared to cases with lower fluxes where due to lower densities of hydrogen atoms on inner surfaces the probability of being trapped or recombined is smaller.

4.3.3 Effect of trap site density

Two possible ways for an hydrogen atom to get trapped had been investigated. In the first case a predefined number of trap sites were distributed and trapping was treated as a recombination event between a solute hydrogen atom and a trap site. Three runs were carried out with a trap density varying from 1.5 to 2.5×10^{13} *trap sites/cm²*. There were more trapped hydrogen atoms in case of the higher trap density but neither the retained nor the released amount of hydrogen was influenced.

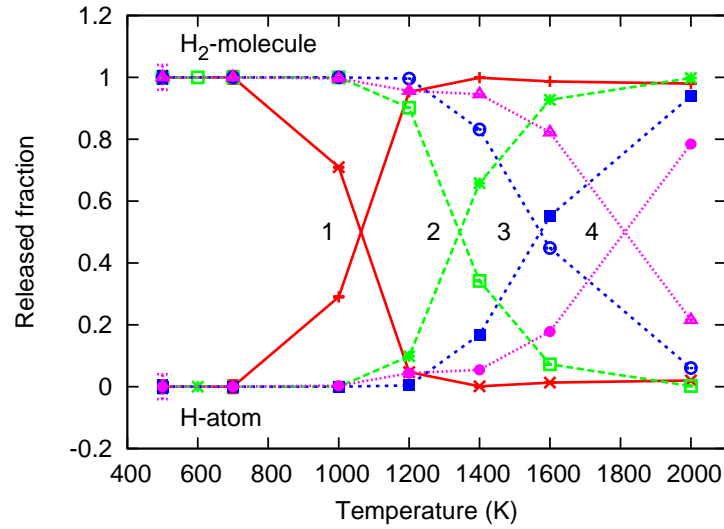


Figure 4.5: Released amount of hydrogen atoms and molecules as a function of temperature for different incident fluxes. The flux value for curves are (1 \rightarrow 10^{17} $H/m^2/s$, 2 \rightarrow 10^{20} $H/m^2/s$, 3 \rightarrow 10^{22} $H/m^2/s$, 4 \rightarrow 10^{24} $H/m^2/s$).

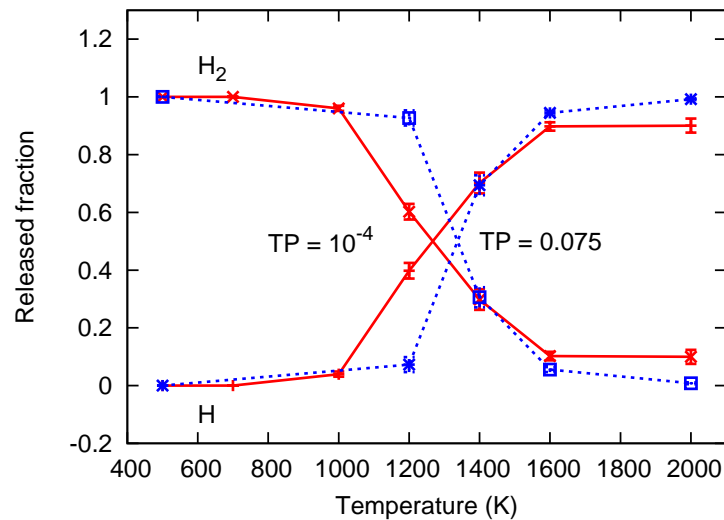


Figure 4.6: Re-emitted amount of hydrogen atoms and molecules for samples having different trapping probabilities (TP).

In the second case a trapping probability was defined and whenever an atom jumped along the surface it had some probability to get trapped. Fig. 4.6 shows the effect of the trapping probability on hydrogen release behavior. Increasing the trapping probability gives rise to more trapped hydrogen atoms. At higher temperature (> 1000 K),

a lot of trapped hydrogen atoms have enough thermal energy that is needed for the detrapping, but after detrapping, for the case with higher trapping probability they get re-trapped before reaching the geometrical surface. Therefore, $T_{50\%}$ shifts towards higher temperatures for samples having higher trapping probability.

The model developed here can be used for the fusion conditions also. For a given kind of co-deposited layer one can calculate the number of active carbon sites which act as trapsites. This gives us a rough estimate of the trapping probability and using the way trapping is handled above, we can simulate co-deposited layer collected from different parts of the fusion machine. One example of such an application is presented in the next chapter.

4.3.4 Effect of the void orientation

A porous graphite sample having 10% void fraction with void size $1\text{ nm} \times 10\text{ nm} \times 10\text{ nm}$ (case 1 : offers $\sim 24.5\%$ internal surface area) in X, Y and Z directions respectively was prepared. In order to check the effect of orientation of the voids, another sample was prepared with similar configuration, but in this case void size was $10\text{ nm} \times 10\text{ nm} \times 1\text{ nm}$ (case 2 : offers $\sim 45.5\%$ internal surface area) in X, Y and Z directions respectively.

Fig 4.7 shows the re-emission characteristics of micropores for both of the cases. The diffusion of hydrogen atoms is very fast (0.015 eV or 0.269 eV) within the crystallites, so most of the H-atom remain on the CMI. In case 1, due to the lesser internal surface area available, the local density of H increases on the internal surfaces and therefore probability of forming a molecule with another H-atom or getting trapped at CMI increases and indeed we observed higher number of H_2 getting re-emitted and trapped hydrogen. Also, because of the lesser surface area available in case 1, eventually there are lesser channels through which hydrogen atoms could diffuse and arrive the real surface and be released that is why we observe higher retention and lower re-emission.

The important thing to be noted here is the shift of $T_{50\%}$ (temperature at which both hydrogen atoms and H_2 molecules are released in equal amount) towards lower temperature in case 2. This is due to the fact that an out-diffusing hydrogen atom may

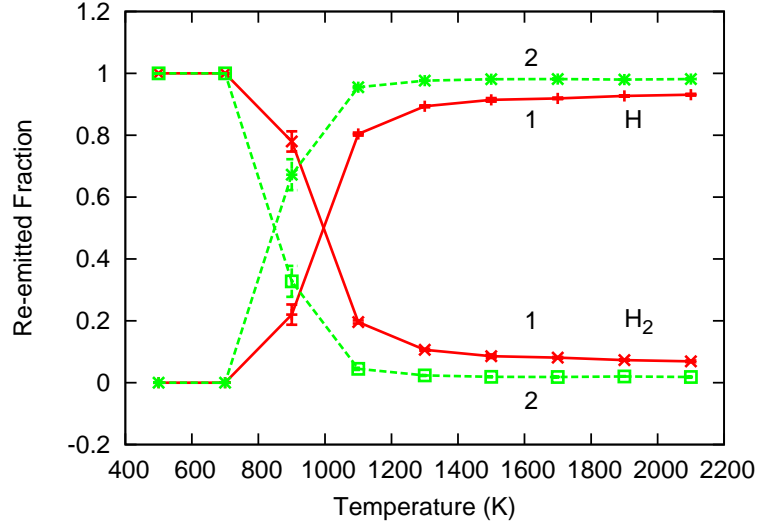


Figure 4.7: Re-emitted amount of hydrogen atoms and molecules for samples having different void orientations. The re-emitted signal for case 1 ($1 \times 10 \times 10 \text{ nm}^3$ voids) is represented by solid lines and for case 2 ($10 \times 10 \times 1 \text{ nm}^3$ voids) by broken lines.

recombine or get trapped before reaching the real surface. If it gets trapped then it attempts to get detrapped with a temperature dependent probability. During the movement towards the real surface it goes through a series of trapping–detrapping events. The lower the internal surface area is, the higher the probability of getting trapped or recombined and therefore the higher the frequency of the trapping–detrapping events needed for an out diffusing hydrogen atom to reach the real surface. Therefore, the lower the internal surface area is, the higher is the number of detrapping events required for an hydrogen atom to reach the real surface in atomic form and therefore $T_{50\%}$ shifts to higher temperatures in case 2, which has the larger internal surface area.

4.3.5 Effect of the void fraction

A cubic structure of $1 \times 10^{-7} \text{ m}$ representing one typical granule was created. $200 \times 200 \times 200$ cells were used with an elementary cell size of 0.5 nm . 2000 H atoms were uniformly distributed in X-Y at a depth of $3.75 \times 10^{-8} \text{ m}$ along Z with a Gaussian distribution of width $7.8 \times 10^{-9} \text{ m}$ as calculated from TRIM runs of 1 keV hydrogen atoms impinging on carbon.

In Fig. 4.8 the re-emitted flux for graphite with void fractions of 5 %, 7 % and 9 % bombarded with 1 keV hydrogen ions are shown. It is evident that by changing the void fraction from 5 % to 7 %, $T_{50\%}$ shifts to higher temperatures.

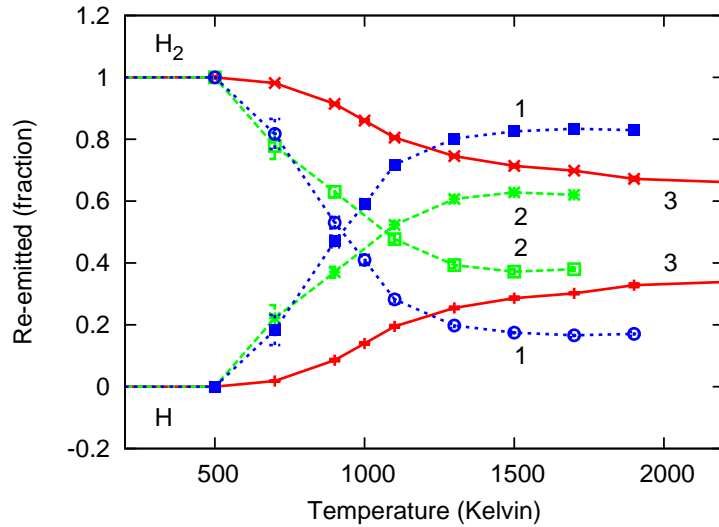


Figure 4.8: Re-emitted flux of hydrogen atoms and molecules as a function of temperature for 5 % (curve 1), 7 % (curve 2) and 9 % (curve 3) voids. The elementary size of a void in all the cases was $5 \times 10^{-9} m$.

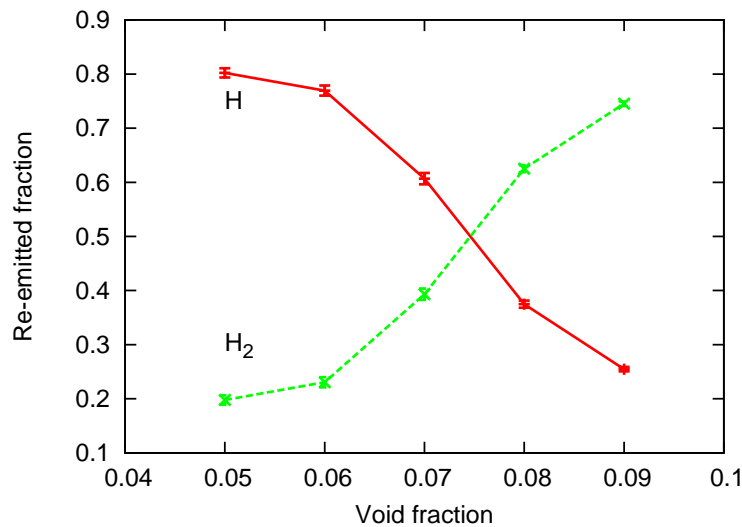


Figure 4.9: Re-emitted fraction of hydrogen atoms and molecules as a function of the void fraction at 1300 K. The elementary size of the voids was $5 \times 10^{-9} m$.

Increasing the void fraction to 9 % with constant elementary void size, we observe that larger amounts of hydrogen molecules are formed. As we increase the void fraction with same elementary void size we have more voids and lesser bulk elements, where a possible trapping of the atoms can happen (each bulk element represents one micro-crystal where at its surface trapping/detrapping can occur). Therefore, more hydrogen

molecule recombination events can occur and the molecular hydrogen flux increases (Fig. 4.9).

4.3.6 Effect of the void size

Changing the elementary void size and keeping the void fraction constant, Fig. 4.10 also shows an increase of the re-emitted hydrogen molecular flux with increasing elementary void size.

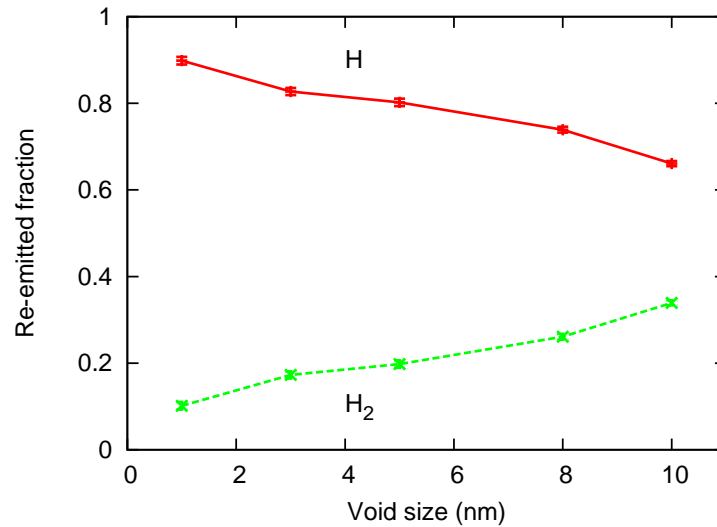


Figure 4.10: Re-emitted flux of hydrogen atoms and molecules as a function of the elementary void size at 1300 K for a void fraction of 5 %.

In this case, the sample has less internal void surface with increasing elementary void size (small elementary voids create a large number of small voids, large elementary voids create a small number of large voids for a fixed void fraction). Therefore, less and less trapping/detrapping can occur at the void surfaces and more hydrogen molecular recombination events can happen.

4.4 Recap

The multi-scale model presented previously (chapter 3) was validated against the ion-beam experiment performed at KFA Jülich [56]. It was used to model the hydrogen reactive-diffusive transport in porous graphite for ion-beam experiments. Various factors affecting the retention and release of hydrogen from graphite were analyzed. For

given ion beam parameters (flux, energy, geometry etc.) the amount of internal surface provided by a graphite sample (which is determined by of void fraction, void size and void orientation) determined the retention and release behavior of hydrogen. The void fraction had the most dominant role followed by the void size and then the void orientation came into play.

Now a model has been developed which can be applied to understand the retention and release behavior of a given graphite sample present in a fusion machine or an ion beam experiment environment by varying the parameters like incident flux, trapping probability and internal structure. For instance if one knows the kind of porous graphite sample existing at a given location (a divertor target tile or a co-deposited carbon layer), the model can be used in a predictive mode to determine the retention and release characteristics during off-normal events (sudden increase of flux, energy or surface temperature due to heating etc.). In the next chapter the model has been applied to study the hydrogen transport in carbon deposits collected from the neutralizer region of Tore-Supra.

Chapter 5

Retention and release from Tore Supra Co-deposits

Tritium retention is a key issue to be investigated for the next step fusion devices using carbon walls. Tore Supra offers a unique opportunity to study the steady-state particle balance due to its ability to produce long discharges (>200 s) [63]. In long pulses, particle balance gives evidence that a constant fraction of the injected gas (typically 50% of the injected fuel) is retained in the wall for the duration of the shot, showing no sign of wall saturation after more than 6 minutes of discharge [64]. Extrapolation of these results for ITER leads to an unacceptable value of tritium retention levels in the machine. In addition to this, the ratio of D/C in the deposits collected from Tore Supra (TS) neutralizer deposits is $< 1\%$. Neither implantation nor co-deposition could explain the constant retention rates observed in TS.

It was speculated that the implantation of the hydrogen followed by the diffusion through the internal porosity could lead to the penetration and trapping of the hydrogen much deeper than expected on the basis of depth of penetration, into the graphite used as PFC. This gives rise to the need for a better understanding of the transport, retention and re-emission of hydrogen into the co-deposited layers and into the graphite. The two main mechanisms that can contribute to the hydrogen retention in fusion devices are co-deposition and the hydrogen diffusion through the internal porosity of the graphite used as PFC [65].

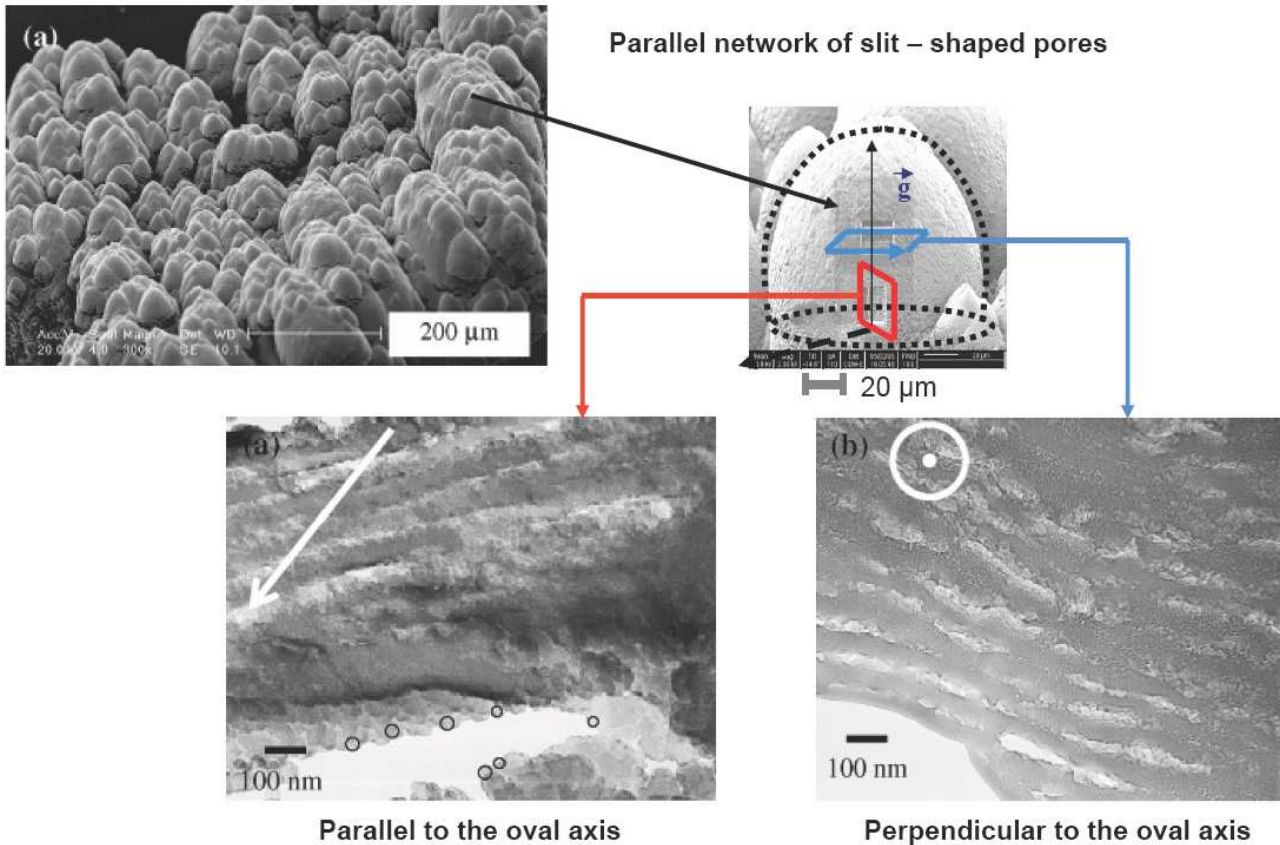


Figure 5.1: Fig. on the upper left is the Scanning electron microscopy micrograph of Tore Supra deposits collected at the leading edge of the neutralizer (TS-NTR). Transmission electron microscopy micrographs of TS-NTR thin foils prepared using focused ion beam is presented at the bottom of the figure [66].

5.1 Structure of Tore Supra co-deposits

Based on the experimental structural analysis [66], the hydrogen retention and re-emission of the deposits found on the leading edge of the neutralizer (named N-LE) of Tore Supra was simulated. The typical plasma flux near this region was about $10^{16} - 10^{17} D^+ cm^{-2} s^{-1}$ and the temperature can reach up to 1500 K. The deposits were analyzed using adsorption isotherm measurements and electron microscopy. The incident ion energy near the neutralizer region was typically 50 – 300 eV. The location of these deposits was in the direct line-of-sight of the plasma (under the toroidal limiter). Fig. 5.1 shows the Scanning Electron Microscopy micrographs of the deposits. At this location the field lines are almost perpendicular to the surface and the deposited layers grows in ovoid-shaped structures, elongated along a direction close to that of

the magnetic field [63].

It was found that the neutralizer deposits show an ovoid shape structure and a high specific surface area (around $190 \text{ m}^2\text{g}^{-1}$). They consisted of small graphite like crystallites whose typical sizes were 2–4 nm and 7–9 nm parallel and perpendicular to the graphene planes respectively. The porosity of these deposits was multi-scale in nature consisting of micropores with typical size lower than 2 nm ($\sim 11\%$), mesopores (typical size between 2 and 50 nm, $\sim 5\%$) and macropores with a typical size more than 50 nm. Transmission electron microscopy performed on thin foils cut from an ovoid revealed a regular network of parallel slit-shaped mesopore (size ~ 10 nm) and macropores (size ~ 100 nm), with a well-defined orientation with respect to the ovoid axis. It was speculated that the micro-porosity measured by volumetric measurements could be due to inter-crystallite stacking defects.

The parametrized recombination rate and TGD (Trans-Granular Diffusion) coefficient for the graphite structure representing Tore Supra deposits at meso-scales (sample having micropore and mesopores) presented above have been used as input to model macropores at macro-scales.

5.2 Analysis of deposits at meso-scale

5.2.1 Setting up the simulation

At meso-scales, the geometry was implemented in the simulations by creating a porous structure of $3 \times 10^{-7} \text{ m}$, $3 \times 10^{-7} \text{ m}$, $1 \times 10^{-7} \text{ m}$ in X, Y and Z direction respectively, representing a typical granule with periodic boundary conditions in X and Y direction. The basic cell size was $1 \times 10^{-9} \text{ m}$. The graphite sample was composed of micropores having 11% void fraction with void size $1 \times 10^{-9} \text{ m}$, $1 \times 10^{-8} \text{ m}$, $1 \times 10^{-8} \text{ m}$ and mesopores having 5% void fraction with void size $1 \times 10^{-8} \text{ m}$, $1.8 \times 10^{-8} \text{ m}$, $1.8 \times 10^{-8} \text{ m}$ in X, Y and Z directions respectively. Out of the total 9×10^6 cells in the simulation box $\sim 21\%$ were surface cells. In the work presented here only the analysis of thermalized hydrogen was done. The ion beam energy considered in the simulation was 300 eV. The profile of the ions given by TRIM calculations was approximated to a Gaussian distribution with a range of penetration of $7.5 \times 10^{-9} \text{ m}$ and a standard deviation of $6.0 \times 10^{-9} \text{ m}$ along the z-direction. The deposits had 0.75 % active carbon

sites, therefore, in the simulation, every time an atom jumps, a trapping probability of 0.0075 was used. Fig 5.2 shows the schematic of the geometry created at meso-scale.

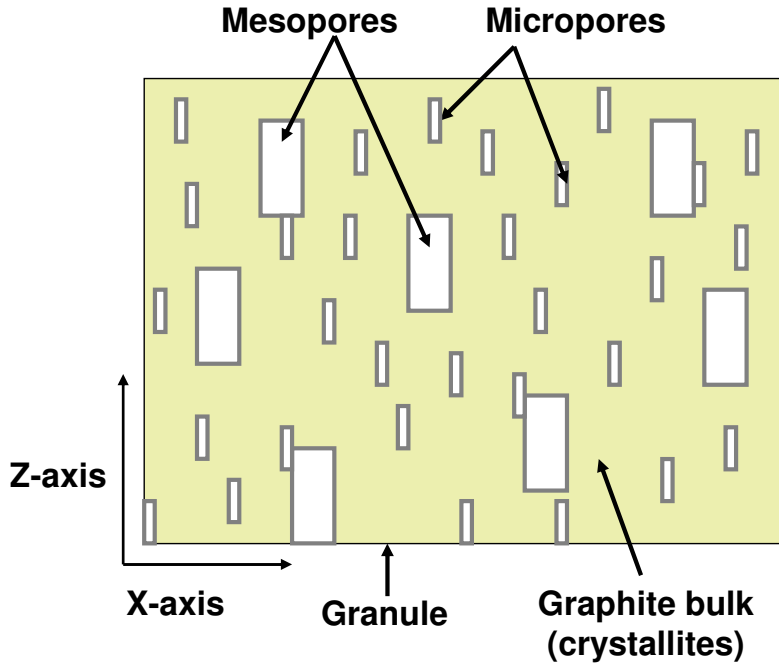


Figure 5.2: Schematic of the Meso-scale geometry.

In the simulations presented in this chapter a continuous influx of hydrogen atoms determined by the flux of the ion beam has been implemented.

$$\Delta N = \phi \times \Delta t \times L_x \times L_y \quad (5.1)$$

where ϕ is the incident flux and L_x, L_y is the system dimension in X and Y direction respectively. Eqn. 2.7 gives the number of particles introduced into the system (ΔN) in time Δt at the surface ($z = 0$). The time step Δt is decided within the KMC scheme. This improvement in the code allows us to understand the effect of the different particles arriving at different times in the simulation and the effect of this on their diffusion and recombination processes.

5.2.2 Results at meso-scale

Fig. 5.3 shows the recombination rate for different incident fluxes from $10^{17} H/m^2/s$ (ion beam experiments) to $10^{24} H/m^2/s$ (plasma fusion devices) as a function of target temperature. Note that for the lower fluxes, there is a peak in the recombination rate and this peak shifts to higher temperatures as the flux increases. It is also seen that the recombination rate increases with increasing flux. At higher incident fluxes there is no peak.

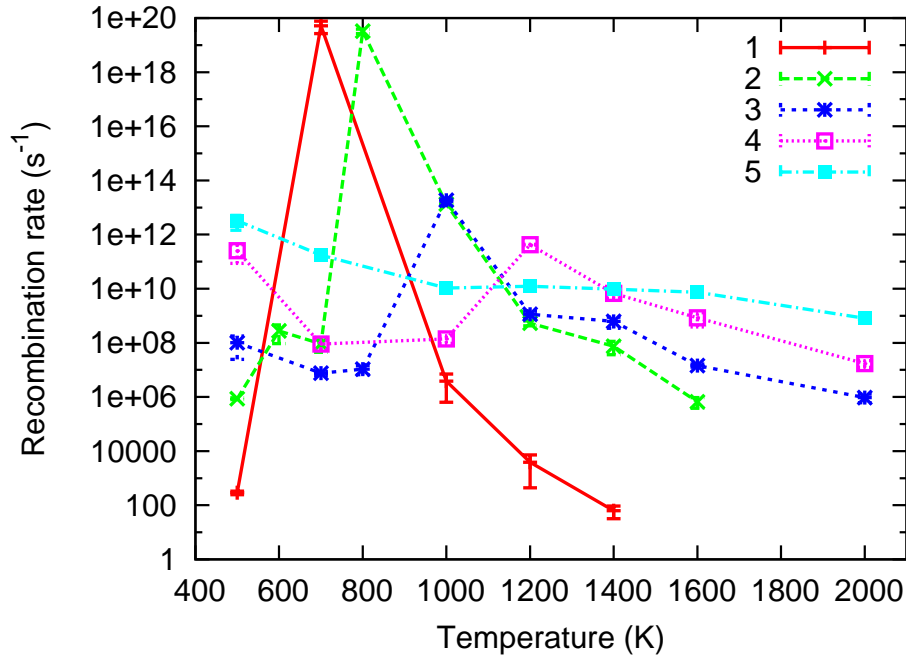


Figure 5.3: Recombination rates from meso-scales as a function of temperatures for different incident fluxes. The flux value for the curves are (1 \rightarrow $10^{17} H/m^2/s$, 2 \rightarrow $10^{20} H/m^2/s$, 3 \rightarrow $10^{21} H/m^2/s$, 4 \rightarrow $10^{22} H/m^2/s$, 5 \rightarrow $10^{24} H/m^2/s$).

This can be understood as follows: the recombination rate depends on two factors: (i) it increases with increasing H density in the sample and (ii) it increases with increased diffusion coefficient of H in the sample. It is well known that for a system of particles if the temperature is increased, they gain energy and starts diffusing out resulting in decrease of the particles density. At a given incident flux, the density decreases with temperature tending to decrease the recombination rate and the diffusion coefficient increases with temperature tending to increase the recombination rate. The increase in recombination rate with increase in temperature is due to the higher mobility of the atoms which increases the probability of the meeting of two atoms. This

balance is what leads to a maximum in the recombination rates as the temperature is increased. It is obvious that, at a given temperature, the density of H increases with increasing flux just because one introduces more atoms per unit time step in the system. Therefore at higher fluxes, the diffusion contribution to recombination rate matches the decreasing density contribution only at higher temperatures and the maxima in the recombination rate peak shifts to higher temperatures. At very high fluxes, diffusion does not affect the recombination rate due to high densities and a maxima does not show up.

Fig. 5.4 shows the effect of the incident flux on the hydrogen retention. At temperatures < 1000 K, most of the incident flux is retained. At higher temperatures there is a drop in the retained fraction, with lower fluxes showing the drop at temperatures lower than those with higher fluxes. As the flux increases, at a given temperature > 1000 K, it is seen that larger fraction of the incident flux is retained.

The main contribution to the retention is hydrogen molecule formation in crystallites. Therefore, recombination rates affect directly retention. The probability of recombination compared with the probability of other processes that occur (H desorption, detrapping, etc.), which at low temperatures have a very low probability of occurrence, decides the number of recombination events taking place.

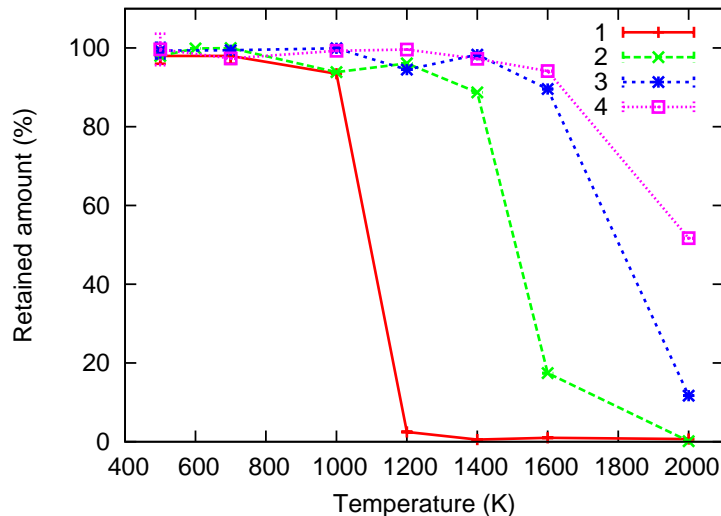


Figure 5.4: Retained amount of hydrogen from meso-pores as a function of temperatures for different incident fluxes. The flux value for the curves are (1 $\rightarrow 10^{17} H/m^2/s$, 2 $\rightarrow 10^{20} H/m^2/s$, 3 $\rightarrow 10^{22} H/m^2/s$, 4 $\rightarrow 10^{24} H/m^2/s$).

At temperatures < 1000 K, the hydrogen densities are high, and there is low probability of H atomic desorption, detrapping, etc. The H atoms recombine within the crystallites mainly and these H_2 molecule have a high migration energy (4.0 eV) for diffusion. Due to the size of the hydrogen molecules, their diffusion is difficult within the crystallites (inter-layer spacing of graphene layers is 3.34×10^{-9} m). Therefore one observes high values of retained fraction. As the temperature increases above 1000 K, we observe in Fig. 5.3, that at lower fluxes the recombination rates are lower and the other mechanisms of hydrogen loss (atomic desorption and detrapping, etc) become equally probable. Therefore at lower incident fluxes one sees lesser retained fraction of incident flux.

Hydrogen profile

Fig. 5.5 shows the profile of the hydrogen present in different chemical state (adsorbed, trapped) for different incident fluxes at 1000 K for the meso-scales. When the hydrogen is introduced into the system some of the hydrogen atoms land up in the crystallites and some of them in the voids. The hydrogen atom diffusion within the crystallites is very fast and when they reach the crystallite edges they have a certain probability of being trapped. At low incident flux 1×10^{17} H/m^2s , due to the very low density of hydrogen atoms, the recombination probability is small and therefore most of the hydrogen within the crystallites or on the internal surfaces is trapped.

As the flux increases to 1×10^{20} H/m^2s the density of the hydrogen increases and a significant amount of the hydrogen is present in adsorbed form on the internal surface (0.9 eV). The recombination probability also increases and hydrogen molecules are formed both within the crystallites and on the internal surfaces. When the flux is increased further to 1×10^{22} H/m^2s the density of hydrogen atoms present within the crystallite planes increases further. There is a high probability that the hydrogen atom arriving at the crystallite edge meets another trapped hydrogen present within its recombination distance (0.2 nm). Such a pair of hydrogen atoms has been labeled as $H_{Trap}-H_{Trap}$ and as explained in chapter 2, needs a migration energy of 2.3 eV to get detrapped and become a solute hydrogen molecule. Fig. 5.6 shows schematically the distribution of different hydrogen species for different fluxes. If the flux is increased further to 1×10^{24} H/m^2s the hydrogen profile remains almost self similar.

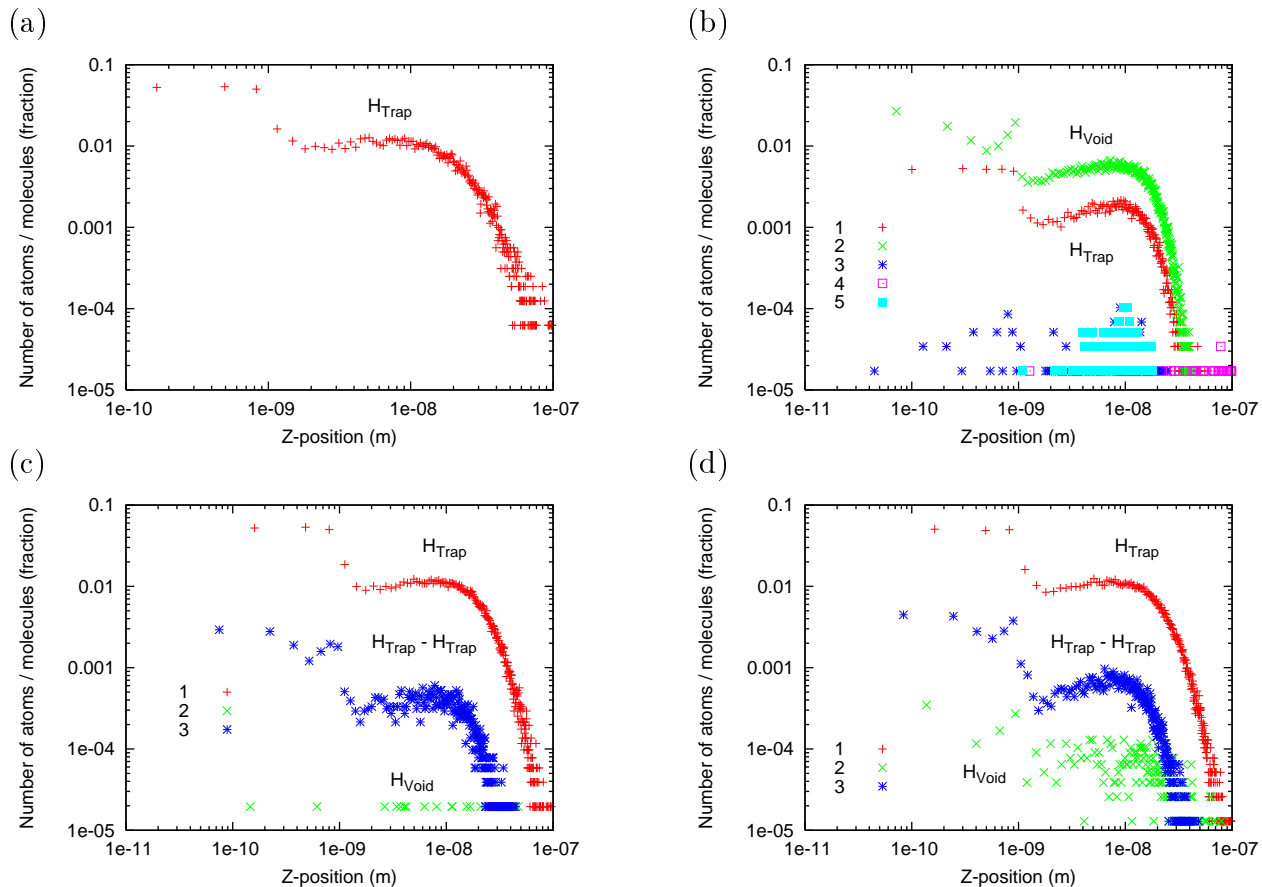


Figure 5.5: Profile of hydrogen present in different chemical state along the Z -direction for different fluxes (fig (a): $1 \times 10^{17} H/m^2s$, (b): $1 \times 10^{20} H/m^2s$, (c): $1 \times 10^{22} H/m^2s$ and (d): $1 \times 10^{24} H/m^2s$,) at 1000 K. 1 \rightarrow trapped hydrogen (2.67 eV), 2 \rightarrow adsorbed hydrogen (0.9 eV), 3 \rightarrow two trapped hydrogen atoms close enough to form a molecule (2.3 eV), 4 $\rightarrow H_2$ molecules in the void and 5 $\rightarrow H_2$ molecules in the crystallites.

5.3 Scaling up to macro-scale

The geometry and the methods used to simulate the hydrogen transport at the macro-scale is shown schematically in Fig 5.7. The atoms at the macropores surfaces are transported using KMC which also provides the time step Δt for the simulation. A Monte-Carlo-Diffusion (MCD) algorithm is implemented for treating the diffusion and recombination within the granules (containing micropores and mesopores) separated by macropores.

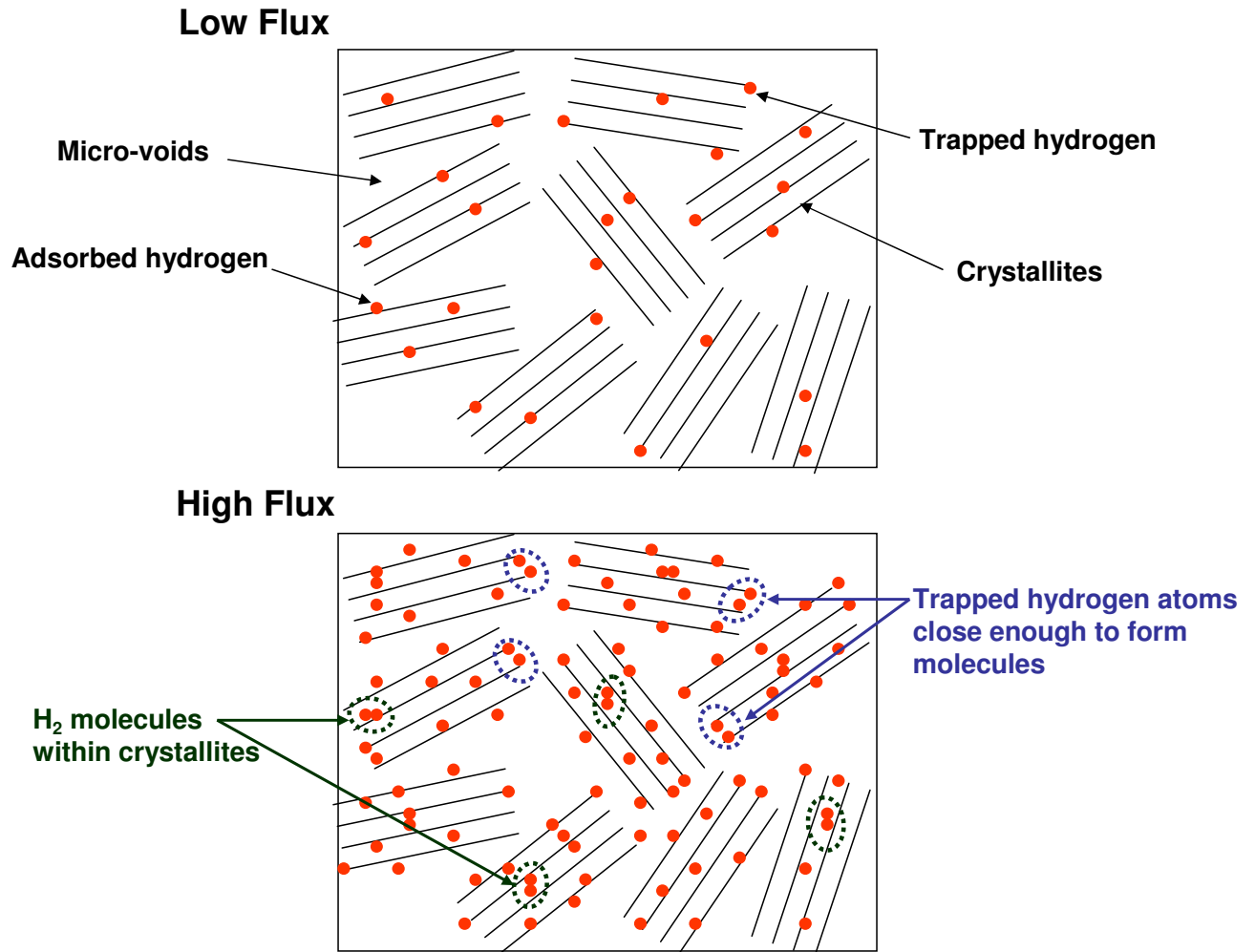


Figure 5.6: Schematic of the distribution of different hydrogen species for low and high fluxes.

To simulate TGD of hydrogen atoms in granules, Eqn.2.6 is used. The time step Δt is decided within the KMC scheme. The Δt is used to decide the number of recombination events that should take place in the time Δt

$$\text{Number of recombination events} = \text{Recombination rate } (s^{-1}) \times \Delta t. \quad (5.2)$$

5.3.1 Setting up the simulation

At macro-scales, the geometry was implemented in the simulations by creating a porous structure of $2 \times 10^{-6} \text{ m}$, $2 \times 10^{-6} \text{ m}$, $2 \times 10^{-6} \text{ m}$ in X, Y and Z direction respectively, with

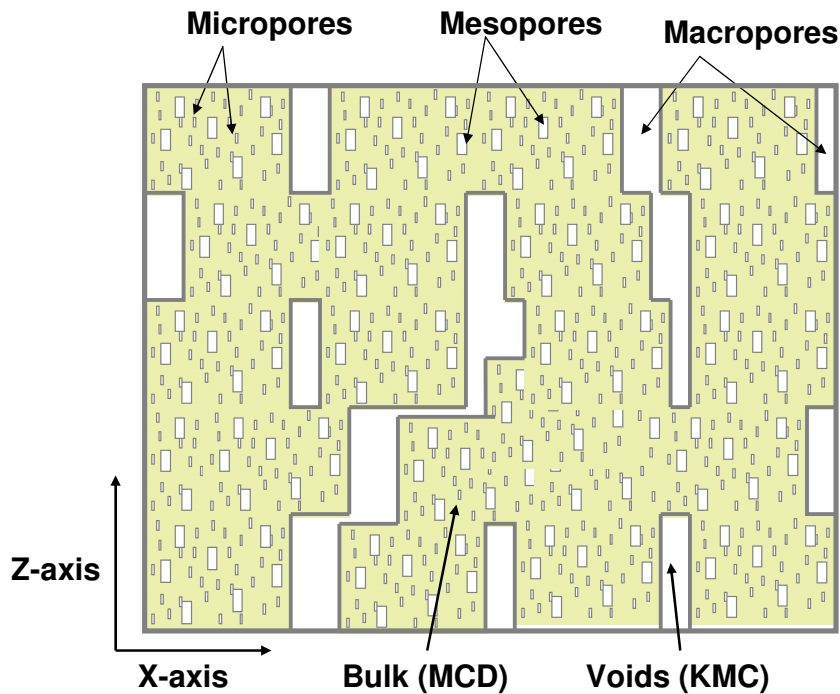


Figure 5.7: Schematic of the macro-scale geometry.

periodic boundary conditions in X and Y direction. The basic cell size was $1 \times 10^{-8} m$. The graphite sample was composed of macropores having 10% void fraction with void size $1 \times 10^{-7} m$, $1 \times 10^{-7} m$, $6 \times 10^{-7} m$. For the hydrogen atom and molecule transport, KMC was used in the voids and MCD was used in the granules. Fig. 5.8 shows the void size distribution in X, Y and Z directions created from the simulation.

5.3.2 Results at macro-scale

Fig. 5.9 shows the retained amount of hydrogen at meso-scales (sample having micropores and meso-pores together) and macro-scales (sample having macropores) from the simulations of typical structures corresponding to Tore Supra deposits subjected to flux of $10^{20} H/m^2/s$. It must be noted that the fraction of hydrogen retained by micropores and mesopores till 1600 K is $\simeq 90\%$ whereas for macropores it is around 60%. This implies that the macropores play a dominant role for the release of hydrogen. This is also intuitive because the large macropores gives an easy access to the geometrical

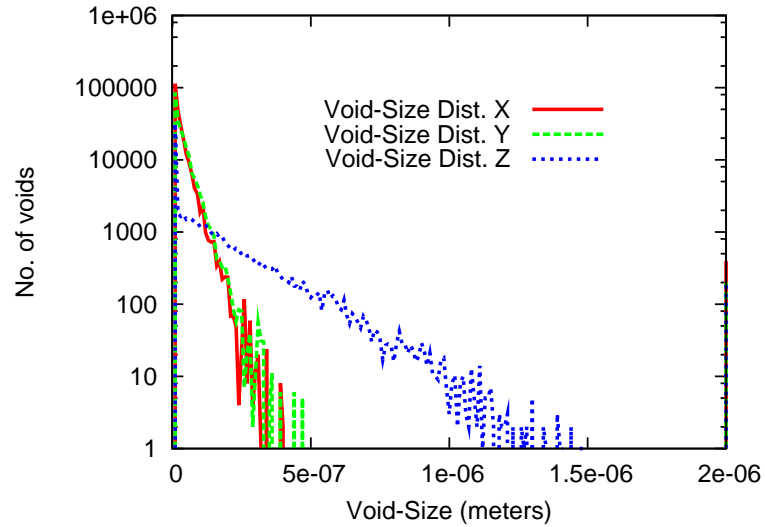


Figure 5.8: Void size distribution for the macropores created from the simulation.

surface. At 2000 K, the retention level drops to zero for mesopores whereas 10% hydrogen is still retained in the macropores. This could be possible if some of the hydrogen which is released from the mesopores get trapped at the macropore surfaces. This gives rise to an internal inventory (or deposition) on macropore surfaces. This mechanism might play a very significant role during the chemical sputtering of such deposits. Hydrocarbons will deposit on the internal surfaces of the macropores. This will further enhance the tritium retention problem.

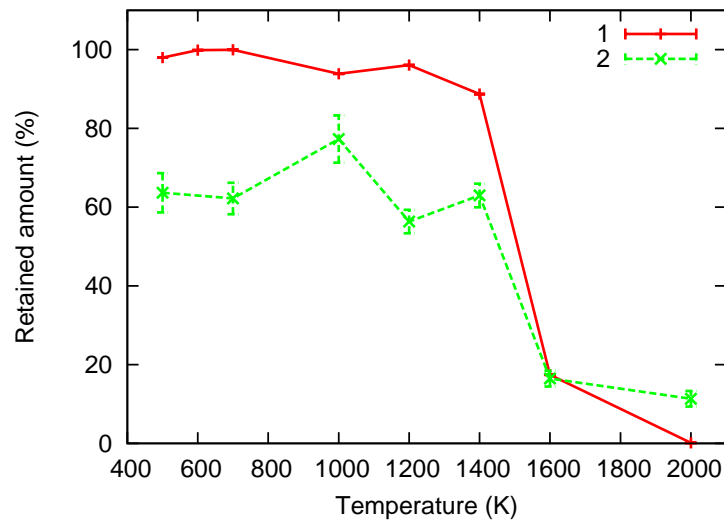


Figure 5.9: Retained amount of hydrogen for mesopores (curve 1) and macropores (curve 2). The incident flux was $10^{20} H/m^2/s$.

Fig. 5.10 shows the hydrogen release behavior for mesopores and macropores. From the total released amount the fraction contributed by atoms and molecules is plotted on the Y-axis. The retained amount for these two cases are given in Fig. 5.9 and one can find for each temperature the exact amount of hydrogen released from the retained amount ($100\% - \text{retained amount}(\%)$). At meso-scales, the hydrogen release curve follows the experimental results of [56] and the model calculation of [29], *i.e.* the released flux is mainly molecular hydrogen at lower temperatures and atomic hydrogen at higher temperatures. At macro-scales, all the hydrogen atoms which are distributed on the macropore surfaces, are trapped (high trapping probability of 0.0075) or they diffuse deep into the bulk. The hydrogen atoms which land up in the granules diffuse within it (MCD, using TGD coefficient) and get recombined to form hydrogen molecules (determined by the recombination rate calculated at meso-scales). As explained above, all the hydrogen released as atoms from the mesopores get trapped again at the macropores surfaces. The hydrogen which is released in the molecular form from the mesopores, due to its chemical inactivity is able to reach the geometrical surface and get released from there. Therefore, at macro-scales even at very high temperatures hydrogen is released mainly in the molecular form.

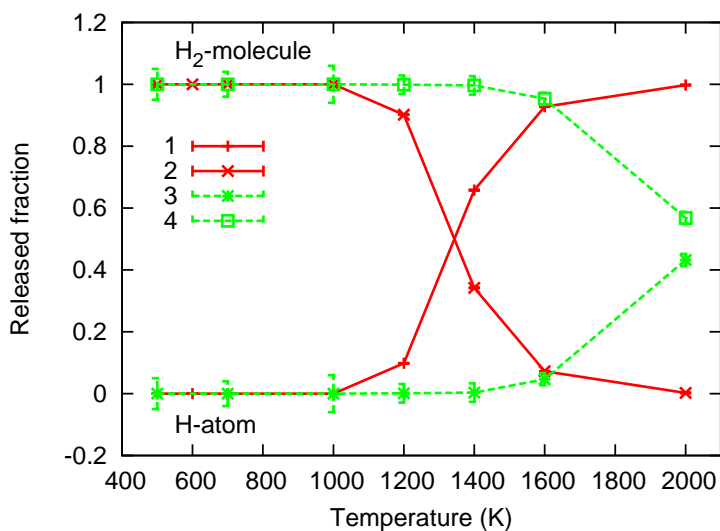


Figure 5.10: Released amount of hydrogen atoms and molecules as a function of temperature for mesopores and macropores. Hydrogen atoms and molecules for mesopores are represented by curve 1 and 2 respectively. Similarly, for macropores hydrogen atoms and molecules are represented by curve 3 and 4 respectively.

Hydrogen profile

Fig. 5.11 shows the profile of the hydrogen present in different chemical state (adsorbed, trapped) at the macro-scales. It can be seen that most of the hydrogen is either adsorbed (0.9 eV) or trapped (2.67 eV) on the macropore surfaces. A large quantity of hydrogen is able to diffuse well beyond the implantation range ($7.5 \times 10^{-9} m$). As explained above, a lot of hydrogen released from the mesopores remains adsorbed or trapped at the macropore surfaces and a significant amount of hydrogen is present in the molecular form within the crystallites in the granules having mesopores and micropores. Fig. 5.12 view of the X–Y plane located at $Z = 5.5 \times 10^{-8} m$. All the atoms having their Z-position between 50 to 60 nm have been projected on the X–Y plane.

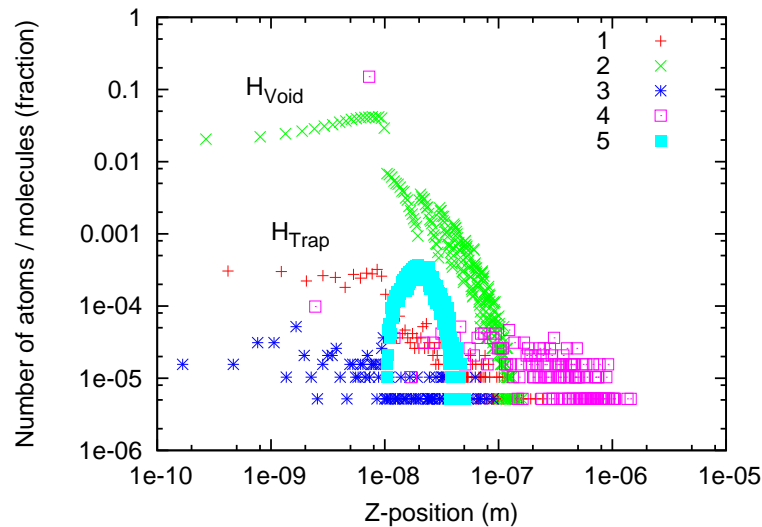


Figure 5.11: Profile of hydrogen present in different chemical state along the Z-direction. 1 → trapped hydrogen (2.67 eV), 2 → adsorbed hydrogen (0.9 eV), 3 → two trapped hydrogen atoms close enough to form a molecule (2.3 eV), 4 → H_2 molecules in the void and 5 → H_2 molecules in the crystallites.

Residence time

The average time spent by a hydrogen atom in graphite (residence time) was calculated and it depends on the temperature of the sample and the incident flux. The molecular diffusion is very fast, therefore, the residence time of hydrogen coming out as molecules is much lesser than the residence time of hydrogen released as atoms. At meso-scales, for ion-beam experiment fluxes ($\simeq 10^{17} H/m^2/s$) and 1200 K, the typical residence

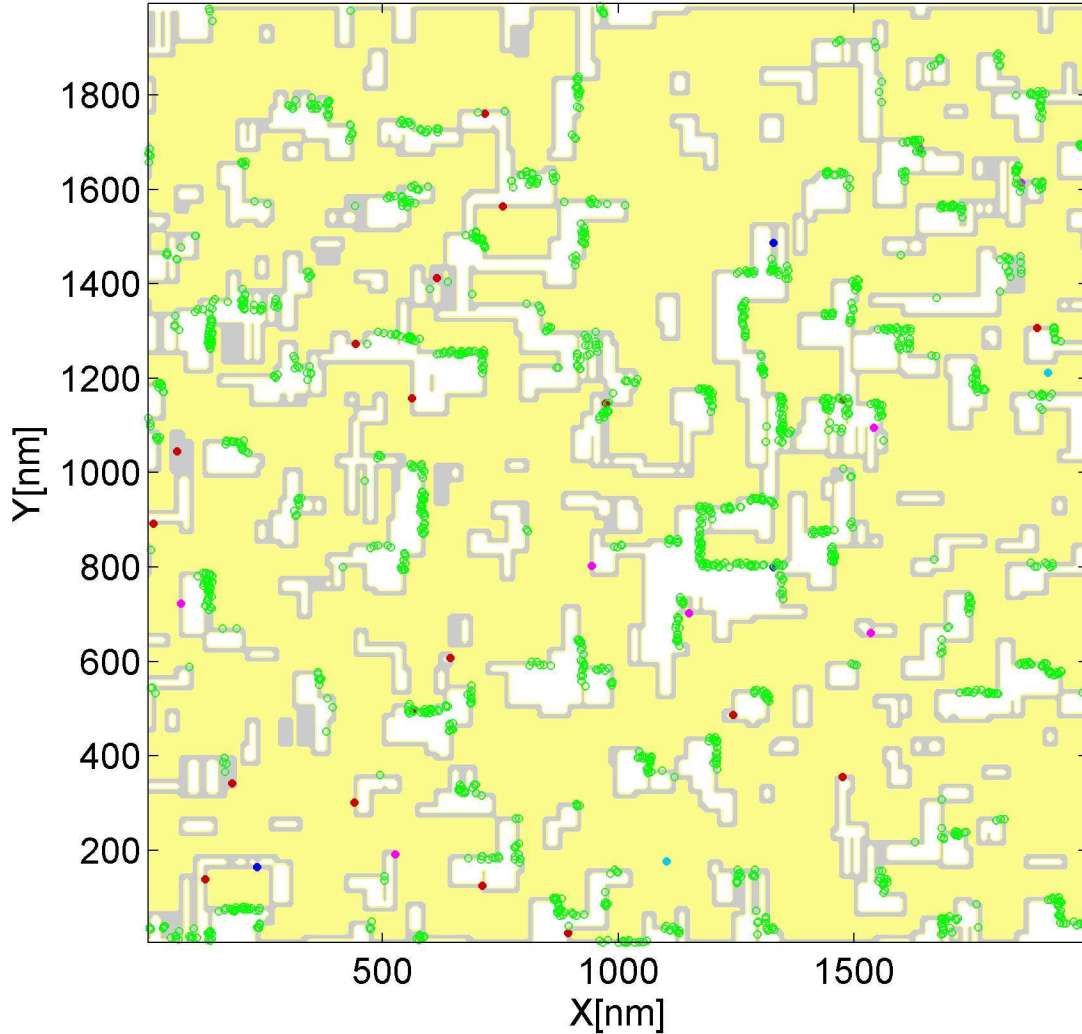


Figure 5.12: A view of the X–Y plane located at $Z = 5.5 \times 10^{-8} m$. The white, grey and pale colored regions correspond to void, surface and the bulk of the graphite respectively. Open green circle: adsorbed hydrogen atom, red dots: trapped hydrogen atom, cyan dots: H_2 molecules in the crystallites, magenta: H_2 molecules in the void and blue dots: two trapped hydrogen atoms close enough to form a molecule

time is around $10^{-3} s$ for atoms and $10^{-2} s$ for hydrogen coming out in molecular form. This is in good agreement with the typical residence time of hydrogen atoms calculated by Haas et al. [67]. They calculated residence time of the hydrogen atoms in ASDEX upgrade and DIII–D tokamaks to be around 1 ms. With increasing flux to $10^{20} H/m^2/s$, at 1200 K, the residence time is $10^{-10} s$ for atoms and $10^{-7} s$ for molecules. At macro-scales no atoms are released at 1200 K and the residence time is around $10^{-7} s$ for

molecules.

5.4 Recap

The multi-scale model was used to study the hydrogen retention and release from Tore Supra deposits. The question which motivated us to study the Tore-Supra deposits was to understand the continuous uptake of the hydrogen. It was shown in the simulations that the accumulation of the hydrogen on the surfaces of the macropores was mainly responsible for the large uptake of the hydrogen in these deposits. A large quantity of hydrogen molecules got stuck in the graphene planes and this also acted as a sink for the hydrogen. The typical residence time of the hydrogen in graphite calculated using the 3D-KMC model was found to be in good agreement with the experiments.

After having understood the hydrogen transport in porous graphite, the next question is where does the molecule formation take place? Does it happen at the end of the ion range, which will indicate that molecule formation is a local process, or it takes place throughout the implantation range (starting from surface till the end of the implantation zone)? Another way of formulating this question is: In which form does the hydrogen transport within the graphite sample take place (atomic or molecular)? For this purpose in the next chapter the hydrogen isotope exchange reaction in graphite is studied.

Chapter 6

Isotope exchange in graphite

So far we have studied the hydrogen retention and re-emission from graphite. In fusion machines hydrogen isotopes, deuterium and tritium, are used as fuel. A natural extension of the work presented till now is to study the effect of hydrogen isotope on release behavior. In experiments this is done by bombarding the target material simultaneously with H^+ and D^+ ion beams and studying the effect of different isotopes on processes like molecule formation or trapping. In the present chapter the results of hydrogen isotope exchange reaction have been presented.

Two important aspects of studying isotope exchange reaction are:

- To understand whether the hydrogen molecule formation takes place at the end of the incident ion range or is it happening throughout the implantation region.
- If the molecule formation takes place throughout the implantation range then the isotope exchange reaction can be used as a cleaning (retrieving the retained tritium from the sample) method of a target material saturated with tritium by bombarding it with deuterium or hydrogen.

6.1 Isotope exchange: present status

In order to understand whether in the implantation range the migration of hydrogen takes place in atomic or in molecular form (after the formation of molecules at the end of the implantation range of hydrogen) a series of experiments were performed by [68, 45, 69]. In experiments the isotope exchange reaction was studied by bombarding a sample simultaneously with H^+ and D^+ ion beams having:

- completely overlapping ion ranges.
- completely separated ion ranges.

Fig. 6.1 shows the re-emission times traces for the two energy combination cases corresponding to maximum overlap and complete separation, respectively. It is evident that the re-emitted signal is independent of the two ion distributions. This gives an indication that the hydrogen atoms diffusion takes place in atomic form too and the molecule formation doesn't take place locally at the end of the ion range. However, it was also pointed out that in the absence of incoming energetic ions, the samples which are 'virgin' (having very less damage), the molecules are indeed formed locally at the end of the ion range.

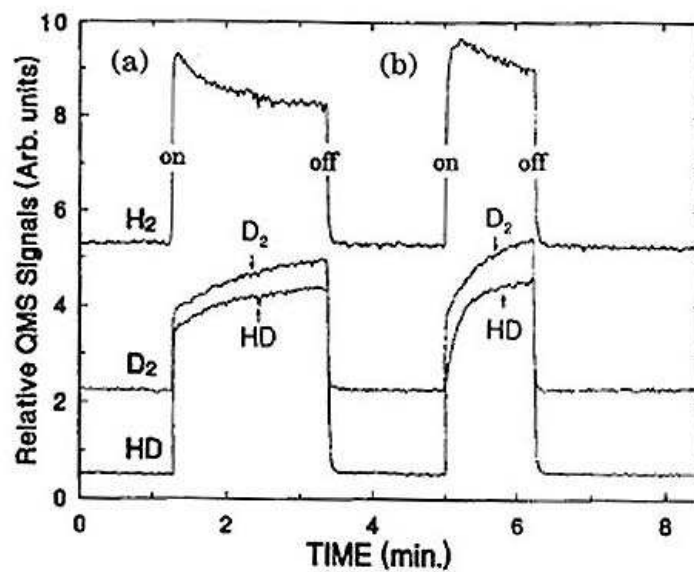


Figure 6.1: HD mixing as a function of H^+ / D^+ range separation during simultaneous bombardment of HPG99 graphite with H^+ and D^+ . (a) 10 keV H^+ and 9.4 keV D^+ , $5 \times 10^{15} H^+$ or D^+ / cm^2s (maximum H^+ / D^+ overlap). (b) 10 keV H^+ and 700 eV D^+ , $5 \times 10^{15} H^+$ or D^+ / cm^2s (complete separation) [45].

It was speculated that in case of a 'virgin' sample (having very less damage) the internal porosity was not very well connected and therefore, not enough internal surface was available for the diffusion of atomic hydrogen along the surfaces. This gave rise to

molecular formation mainly at the end of the ion range. Whereas, in the presence of an ion beam, damage is created into the sample and this gives rise to a lot of internal surface area where a hydrogen atom can diffuse and the molecule formation can take place away from the ion implantation region. This result shows that the extent of isotope mixing depends very strongly on the internal structure of the graphite sample.

In order to understand the effect of the internal structure on isotope mixing first the ideal mixing case is simulated where incident ion beams have completely overlapping ion profiles.

6.2 Completely overlapping ion profiles

6.2.1 Setting up the simulation

The geometry was implemented in the code by creating a cubic structure of 140 nm (sample 1), representing a typical granule with periodic boundary conditions in X and Y direction. The void fraction of the sample was 7%. $280 \times 280 \times 280$ cells were used with elementary size 0.5 nm and cubical voids of 6 nm size. 6000 hydrogen and 6000 deuterium atoms were uniformly distributed in X–Y direction at a depth of 59.5 nm along Z with a Gaussian of width 12 nm. This distribution corresponded to the distribution of thermalized hydrogen isotopes with 3 KeV energy. The effect of the collisional cascade physics was considered in this initial profile through pre-calculations of this distribution by the binary collision code TRIM/TRIDYN. Temperature of the sample was 650 K.

In order to analyze the effect of the internal structure of graphite similar simulation was done for a sample (sample 2) having dimension of 50 nm, 50 nm, 100 nm in X, Y, Z direction respectively, representing a typical granule with periodic boundary conditions in X and Y direction. The sample had $\sim 8\%$ void fraction. $100 \times 100 \times 200$ cells were used with elementary cell size 0.5 nm and void size of dimension 10 nm, 18 nm and 58 nm in X,Y,Z direction respectively (Tore-Supra deposits kind of sample). 2000 hydrogen and 2000 deuterium atoms were distributed uniformly in X–Y at a depth of 19.5 nm along Z with a Gaussian of width 7 nm.

6.2.2 Results

In Fig. 6.2, the ideal mixing in this case is visible i.e. $\text{H}_2:\text{HD}:\text{D}_2$ of 1:2:1, as expected by theory.

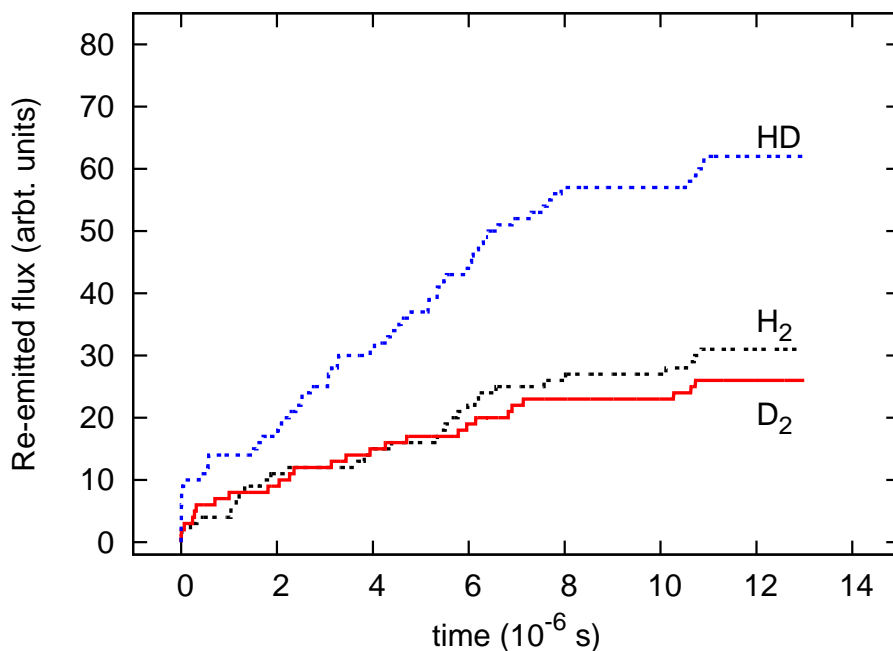


Figure 6.2: Re-emitted flux of molecular species as a function of time for a porous graphite sample having void fraction 7% (sample 1) with totally overlapping profiles of the hydrogen and deuterium ions.

If one compares fig. 6.2 with fig. 6.1 one sees that in experiment the relative re-emitted signal of the hydrogenic species are relatively higher than what is expected from theory for the ideal-mixing case. Following factors were thought to be responsible for this discrepancy:

- (i) Effect of incident fluence of the ion beams on the penetration depth
- (ii) Effect of surface temperature rise due to the energy deposited by the ion beam
- (iii) Presence of a surface layer pre-saturated with hydrogen

Using TRIDYN simulations it was found that the fluence of the ion beam has a negligible effect on the penetration depth of the two hydrogen isotopes. Also the surface temperature rise due to a 10 keV ion beam was estimated to be around 200 K. This didn't explain the observed discrepancy too. All the samples have some hydrogen

content adsorbed on the surface layer due to unavoidable water content in the chamber. Therefore, this influence was studied by preparing a saturated hydrogen surface layer on graphite samples.

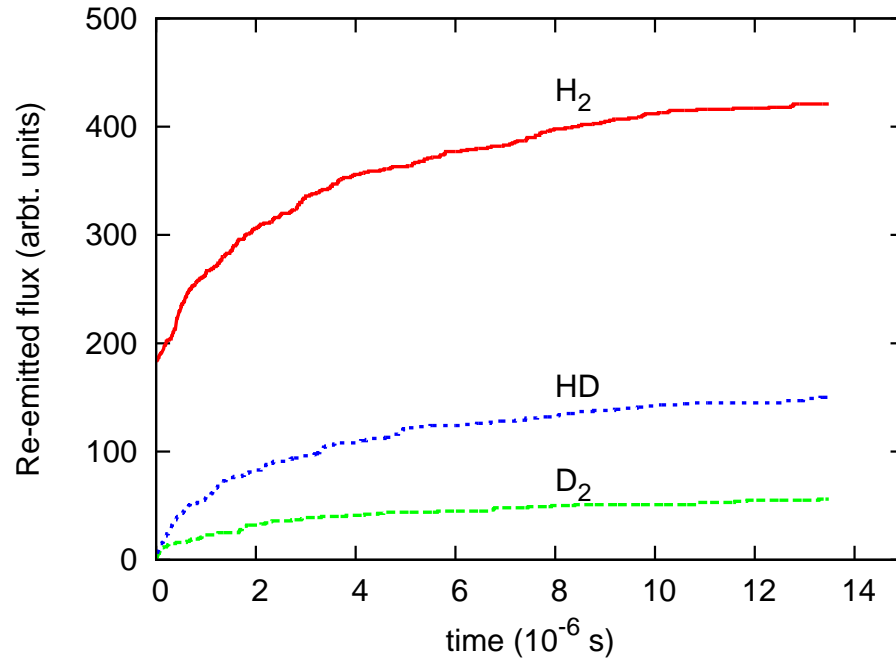


Figure 6.3: Re-emitted flux of molecular species as a function of time for a porous graphite sample having a surface layer pre-saturated with hydrogen and a void fraction of 7% (sample 1) with totally overlapping profiles of the hydrogen and deuterium ions.

Fig 6.3 shows the re-emitted flux for a hydrogen sample having a surface layer saturated with hydrogen. No drastic changes were observed in the behavior of re-emitted signal, just the re-emission level for hydrogenic species shifts to higher values. An isotope difference in the re-emitted amount of hydrogen isotopes is seen. In the beginning, the rate of re-emitted molecules is similar, thereafter molecular species containing hydrogen increases faster and saturates at higher levels as compared to deuterium containing molecules. So, the fluxes follow the order, $\Gamma_{H_2} > \Gamma_{HD} > \Gamma_{D_2}$. This can be attributed to the higher mobility of hydrogen as compared to deuterium due to the lower mass of hydrogen.

Figure 6.4 below shows the released molecular flux from sample 2 for simultaneous bombardment of H^+ and D^+ with overlapping ion profiles. For the sample (sample 2) without a saturated layer ideal mixing i.e. $H_2:HD:D_2$ was observed, as expected

by theory. But, for a sample with a hydrogen saturated surface layer no change in the levels of re-emitted molecules was observed. Whereas for sample 1, the hydrogen saturated surface layer had shown significant effect on the released molecular flux of hydrogenic species (6.3). This was expected because this sample had large voids near the surface, so the net hydrogen content of the surface layer was lesser. Therefore, re-emitted molecules of sample 2 have lesser Hydrogen content as compared to sample 1. It must be mentioned that for both the samples surface layer were formed under similar conditions and with same parameters.

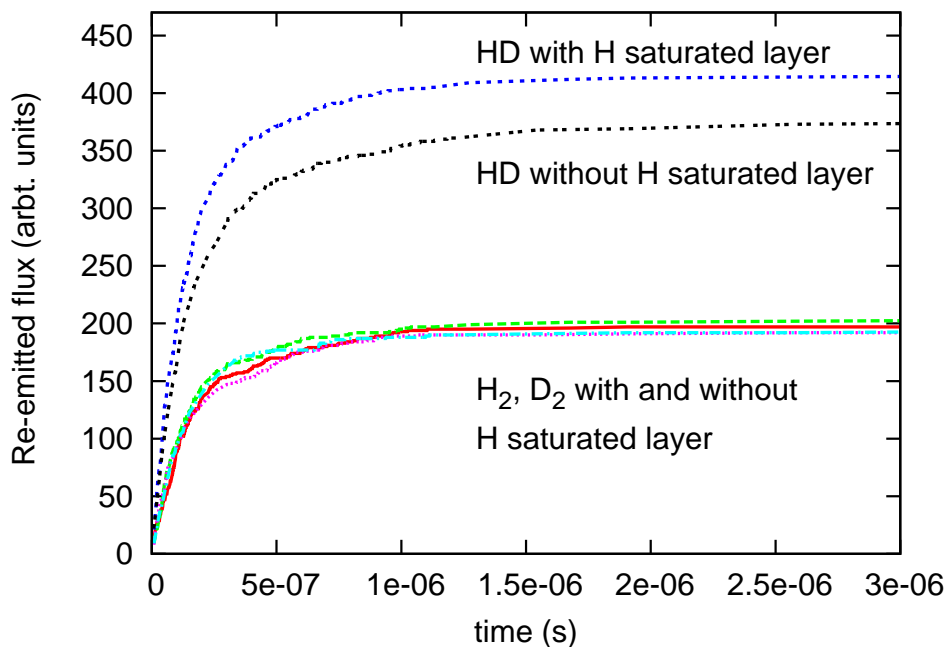


Figure 6.4: Re-emitted molecular flux as a function of time for sample 2 with completely overlapping distribution of hydrogen isotopes. Results are presented for two cases: samples with a pre-saturated hydrogen surface layer and sample without a pre-saturated hydrogen surface layer.

6.3 Completely separated ion profiles

6.3.1 Setting up the simulation

Similar analysis was carried out for completely separated ion ranges. All the geometrical parameters were same. The hydrogen atoms (1 keV having Gaussian distribution in Z-direction with mean value 27.5 nm and standard deviation 8 nm) and deuterium atoms (3 KeV having Gaussian distribution in Z-direction with mean value 59.5 nm

and standard deviation 7.8 nm) were distributed uniformly in X–Y directions. The temperature of the sample was 650 K. At lower temperature HD formation was very strongly reduced which is understandable because at lower temperature ($\sim 400\text{K}$), the diffusion of atoms is very slow. This is clear from the re–emission results of atomic hydrogen at these temperatures (Chapter 4) and one expects the local molecular formation rather than mixed HD molecules which will be formed only after significant atoms starts diffusing throughout the implantation depths.

6.3.2 Results

Fig. 6.5 shows the results for sample 1. The relative fluxes of the modeling agree well with the experiments (Haasz et al.[45]). Just to test the idea, that as soon as the ion beam is switched on, a quick increase in molecular re–emission is seen, the run was continued with increased void fraction to 9% (ion bombardment causes damages and so the increase in void fraction). A rise of both hydrogen and molecular fluxes is seen due to increases of the void fraction as discussed before (chapter 4). However, the experimentally observed jumps of hydrogen molecular fluxes followed by a slow decay to steady state combined with the slow rise of deuterium molecular fluxes is not reproduced. One should note that questions of the interpretation of the experimental results remains too. Therefore, this discrepancy is not too worrying.

Figure 6.6 shows the results of isotope exchange reaction for sample 2 subjected to hydrogen and deuterium ion beam having completely separated ion profiles (hydrogen was distributed at depth of 19.5 nm and standard deviation 7 nm and deuterium at a depth of 39.5 nm and standard deviation 10 nm).

It is observed that a very small amount of mixed molecules were formed. A basic estimate of the time required by deuterium atoms deep inside the bulk to come to the surface where a high concentration of hydrogen atoms exists, was carried out. At this temperature, it was found that the diffusion coefficient, $D \sim 6 \times 10^{-9} \text{ m}^2/\text{s}$ and the deepest deuterium atom was at $5 \times 10^{-8} \text{ m}$, so the time required to reach the surface should be, $\delta t \sim \delta z^2 / 6 \times D$ ($\sim 10^{-7} \text{ s}$). The simulation was indeed carried out for longer times. Another case where hydrogen was distributed deeper than deuterium, i.e. just reversed the profiles of last simulation was analyzed. Two points were noted here,

- (i) the specie which was distributed deeper in the bulk had higher re–emitted flux.

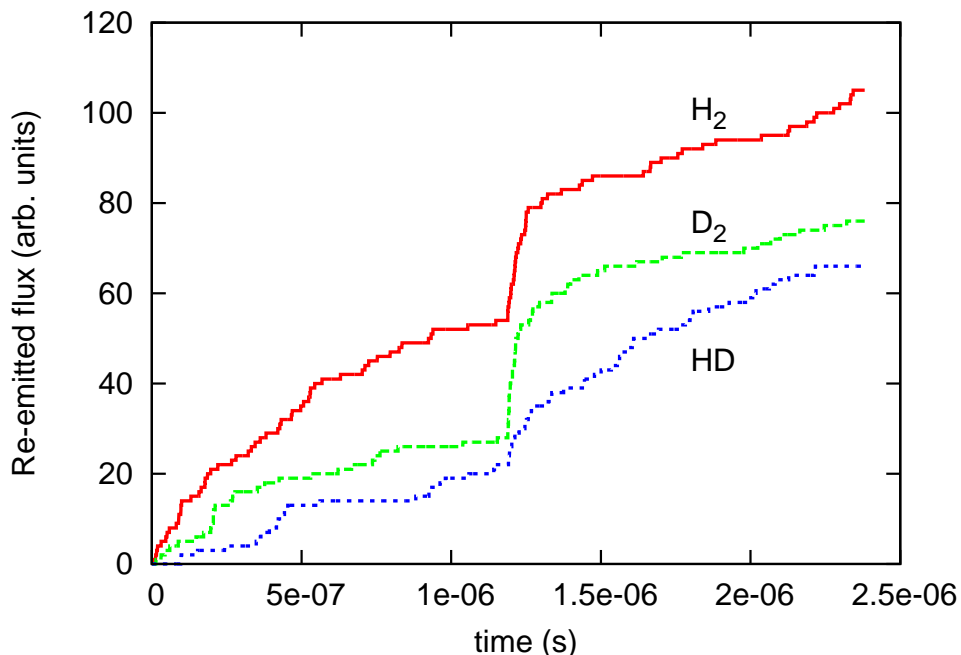


Figure 6.5: Re-emitted molecular flux as a function of time for a porous graphite sample having 7% void fraction (sample 1) with completely separated profile of hydrogen isotopes

The following mechanism is proposed to explain this observation: when the atoms having deeper penetration, there is more probability of getting recombined (with same specie atom) during diffusing out before they could reach the other specie close to the surface. Atoms distributed near the surface are re-emitted more in atomic form. This combined with the fact that molecular diffusion is very fast gives a clear understanding of our first observation.

- (ii) HD re-emitted flux is higher when hydrogen profile is deeper than deuterium. This can be explained by the higher diffusion coefficient of hydrogen at these temperatures.

If one compares the re-emitted flux of sample 2 with that of sample 1, for separate range profiles, one sees that there is a large reduction in relative flux of mixed molecules (HD). This indicates the fact that the mixed molecule formation indeed depends on the internal structure rather than the gross void fraction. The experiments done by Chiu et al. [45] were performed at room temperature. At these temperatures atomic diffusion is very slow and this requires a too long simulation run time for an atom to diffuse to longer distances and recombine. Nevertheless, the basic processes are the same.

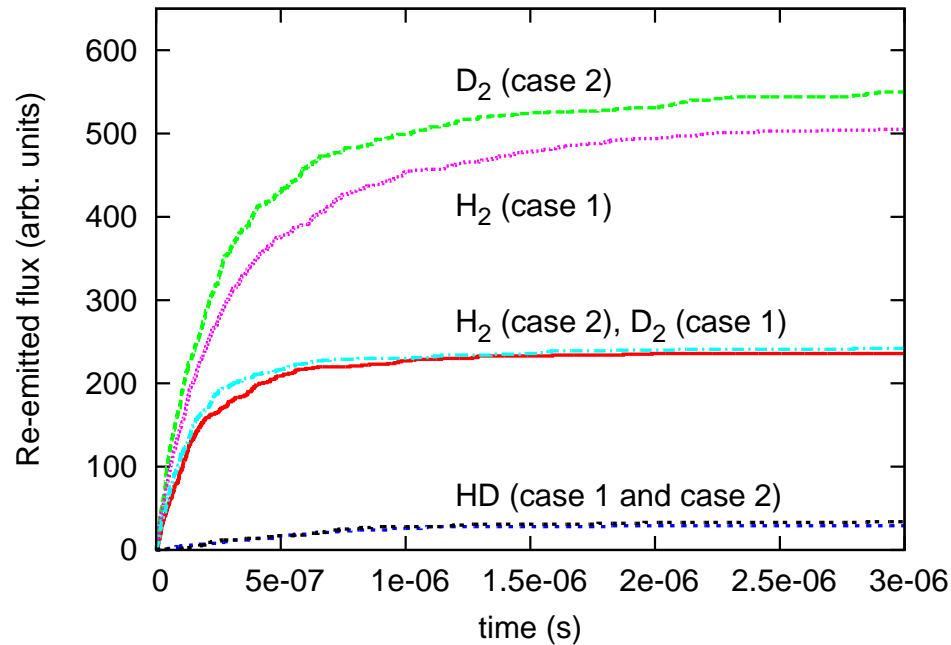


Figure 6.6: Re-emitted molecular flux as a function of time for sample 2. Case 1: hydrogen ion profile deeper than the deuterium ion profile and case 2: deuterium ion profile deeper than the hydrogen ion profile

6.4 Recap

The Isotope exchange reaction of hydrogen in graphite was studied both for completely separated and completely overlapping ion profiles. The mixed molecule formation during the exposure to hydrogen and deuterium ions with completely separate ion profile (penetration depths) indicates that hydrogen molecule formation is not a local process. It takes place throughout the implantation zone and not only at the end of the ion range. The main factors affecting the mixed molecule formation are:

- internal structure of graphite, which affects diffusion coefficient and consequently molecule formation and atomic re-emission
- temperature of the sample, this affects atomic diffusion, which is an important factor for mixed molecule formation.

It must be mentioned that there is need of more experimental data base to compare and understand the results of isotope exchange phenomenon in simulations. Up to now the transport and reactions of hydrogenic species only were studied. In the next chapter

the model is extended to include the reaction of hydrogen with carbon atoms and the chemical erosion of graphite is studied.

Chapter 7

Chemical erosion of graphite

As already pointed out in the introduction of the thesis, erosion of carbon-based materials due to particle impact has long been a concern when it comes to the plasma-facing applications in thermonuclear fusion reactors. Although these materials exhibit excellent thermo-mechanical properties, their susceptibility to erosion through physical and chemical processes limits their lifetimes while increasing plasma impurity levels. There is large uncertainty about the extrapolation of the chemical sputtering yield to high reactor relevant fluxes.

For understanding the chemical erosion process an experiment was performed by Horn et al. [2] where a several mono-layer thick C:H film was grown and exposed to hydrogen ion beam at a flux of $1.9 \times 10^{13} \text{ cm}^{-2} \text{ s}^{-1}$. The basic atomistic processes involved in the chemical erosion process were identified and a simple analytical model was proposed for the chemical erosion of a-C:H films. In this chapter the model to simulate the chemical erosion of porous graphite will be presented. The model presented in the previous chapters to simulate the hydrogen recycling process has been extended to study the chemical erosion process based on the Küppers-Hopf cycle [36, 44].

7.1 Analytical description of chemical erosion

The chemical reaction of energetic ions with carbon atoms was found to occur after slowing down at the end of the penetration depth (range) of the ions. Three main mechanisms have been identified for the chemical erosion

- (i) Thermally activated process

- (ii) Radiation damage
- (iii) Kinetic hydrocarbon emission.

7.1.1 Thermally activated process

The thermally activated process, which leads to a maximum of the chemical yields (Y_{therm}) at temperatures between 700 and 950 K, can be explained by the chemical mechanisms identified by Küppers and co-workers.

Küppers–Hopf cycle for chemical erosion

Fig. 7.1 shows various atomistic processes occurring under thermal H-atom impact on amorphous hydrogenated carbon (a-C:H) films [2]. Küppers and co-workers have identified the following main processes involved during the chemical erosion of the a-C:H films. The rate equation for every process is also written with the bracketed quantities as concentrations, ϕ as H atom flux, σ_H ($= 1.1 \times 10^{-20} m^2$) and σ_D ($= 0.05 \times 10^{-20} m^2$) as hydrogenation and dehydrogenation cross-sections respectively.

- (i) Hydrogenation of the graphitic sp^2 hybridization state (state a), forming state b consisting of a radical sp^x with a neighboring hydrogen-containing carbon in the sp^3 hybridization state.

$$-\frac{d[CH\ sp^2]}{dt} = [CH\ sp^2] \sigma_H \phi \quad (7.1)$$

At higher temperatures split-off of this hydrogen can return the two carbon atoms to their original state b.

$$-\frac{d[CH\ sp^x]}{dt} = [CH\ sp^x] k_{-H} \exp\left(\frac{-E_{-H}}{kT}\right) \quad (7.2)$$

where k_{-H} ($= 10^{13} s^{-1}$) is the frequency factor and E_{-H} ($= 1.73 eV$) is the activation energy for this process.

- (ii) Repetitive application of the hydrogenation to state b will lead to the formation of two carbons in the sp^3 hybridization state (state c), some fraction of which will contain a methyl group attached.

$$-\frac{d[CH\ sp^x]}{dt} = [CH\ sp^x] \sigma_H \phi \quad (7.3)$$

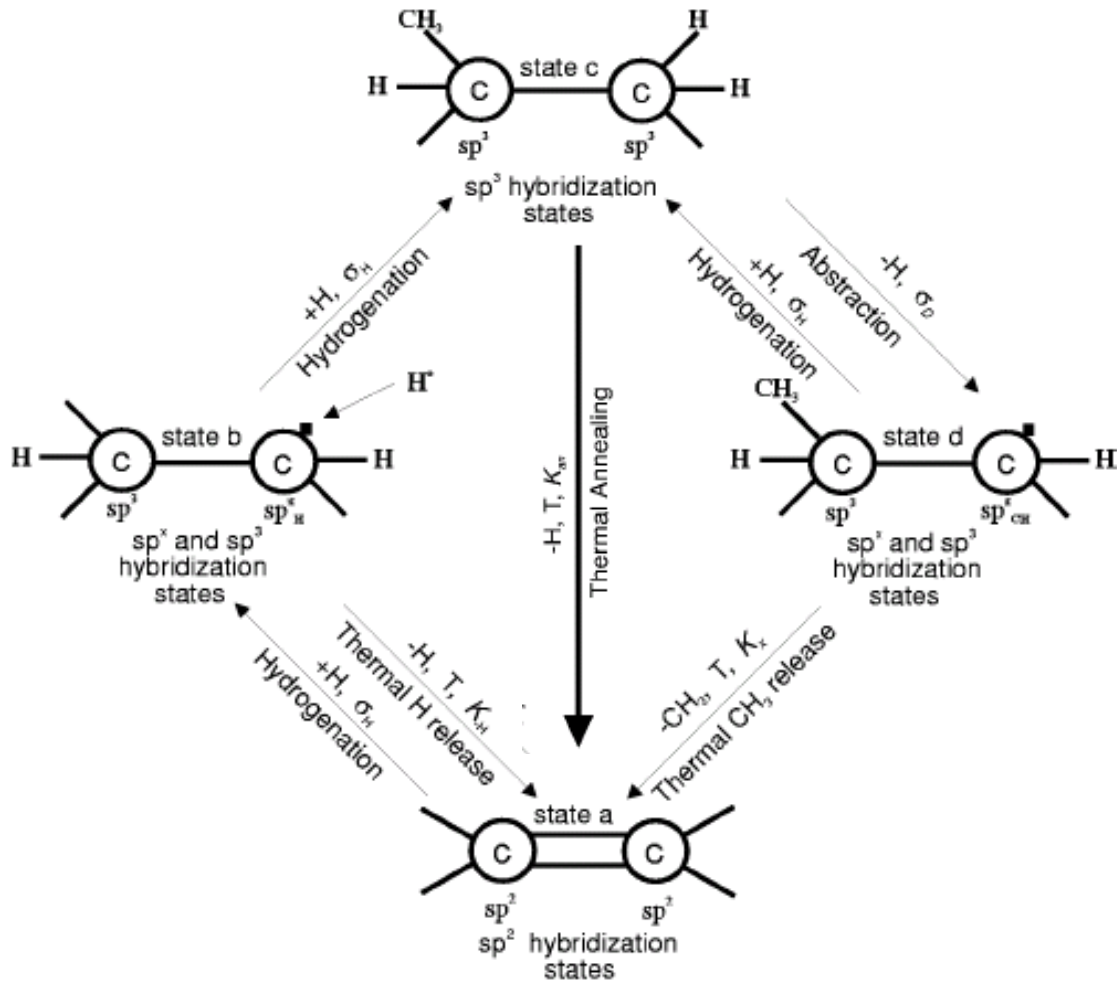


Figure 7.1: Schematic diagram of the reactions leading to methane production due to atomic hydrogen impact on amorphous hydrogenated carbon films, as proposed by Küppers and co-workers [2, 44, 5].

- (iii) Abstraction of a singly bound hydrogen can produce state d consisting of a carbon in the radical sp^x configuration with a neighboring methyl-containing carbon in

the sp^3 hybridization state.

$$-\frac{d[CH\ sp^3]}{dt} = [CH\ sp^3] \sigma_D \phi \quad (7.4)$$

- (iv) Hydrogenation can return state d to state c or, for temperatures above ~ 400 K, the radical can de-excite by split-off of the neighboring methyl group and return the carbon atoms involved to their initial graphitic state a.

$$-\frac{d[CH\ sp^x]}{dt} = [CH\ sp^x] k_x \exp\left(\frac{-E_x}{kT}\right) \quad (7.5)$$

where k_x ($= 10^{13} s^{-1}$) is the frequency factor and E_x ($= 1.604 eV$) is the activation energy for release of methyl group.

- (v) For graphite temperatures in excess of ~ 1100 K thermal annealing can return state c to state a via elimination of some of the ion-induced damage accumulated in the implantation zone.

$$-\frac{d[CH\ sp^3]}{dt} = [CH\ sp^3] k_{an} \exp\left(\frac{-E_{an}}{kT}\right) \quad (7.6)$$

where k_{an} ($= 10^{13} s^{-1}$) is the frequency factor and E_{an} ($= 2.42 eV$) is the activation energy for the annealing.

Thus, at low temperatures, exposure of the film to thermal hydrogen atoms results in the conversion of carbon from the sp^2 to the sp^3 hybridization state with some fraction of radical centers, determined by the ratio of σ_D/σ_H . At higher temperatures (400–650 K) an equilibrium balance between the supply of sp^x radical carbon centers from hydrogenation and abstraction and their loss through thermal decomposition due to methyl and hydrogen split-off is established leading to measurable erosion rates. At even higher temperatures, however, the rapid decomposition of the radical states by H-atom split-off prevents significant hydrogenation to sp^3 hybridization states. This, in turn, means there is little or no abstraction occurring, and so, there is no significant production of carbon in the radical carbon state. Thus, chemical erosion is suppressed at higher temperatures.

The steady-state solution to the above presented set of differential equations leads to a very weak dependence in Y_m (maximum erosion yield) and a very strong dependence in T_m (temperature at which the yield is maximum) on the flux density ϕ . Such dependencies are not observed in experiments. Roth and García-Rosales [70] proposed that, since the absolute concentration of carbon in the sp^3 hybridization state with attached methyl groups is unknown, they use k_x and k_{-H} as fitting parameters adjustable to all the available experimental data in the relevant energy and temperature ranges, and taking into account the flux dependence of Y_m and T_m . The formula resulting from this fitting procedure is

$$Y_{therm} = [CH\ sp^3] \frac{0.033 \exp(\frac{-1.7}{kT})}{2 \times 10^{-32} \phi + \exp(\frac{-1.7}{kT})} \quad (7.7)$$

7.1.2 Radiation damage

In addition to Y_{therm} , a term is required which accounts for radiation damage resulting from energetic impact. For ions with energies above the threshold for physical sputtering, energy deposition in the carbon substrate results in atomic displacement and C-C bond breaking which created active sites increasing the chemical erosion yield. The energy deposited that causes nuclear damage in the surface layer has a maximum between 300 eV and 2 keV, similar to physical sputtering. Roth and García-Rosales [70] had proposed that this enhancement can be well described by a multiplicative term which is proportional to physical sputtering such that the energetic chemical yield is given by

$$Y_{chem} = Y_{therm}(1 + DY_{phys}) \quad (7.8)$$

where D is a constant dependent on the mass of the impinging isotope and Y^{phys} is the physical sputtering yield given by the revised Bohdansky formula [71].

7.1.3 Kinetic hydrocarbon emission

In case of low-energy hydrogen ion impact on carbon, hydrocarbon production is observed at room temperature which is not explained by the atom impact model where higher temperatures are required. The isotope effect on the yield which has been observed for this low energy impact, as well as TDS results [5], suggest that physical sputtering of weakly bound sp^3 centers with attached hydrocarbon ligands may be oc-

curing at the surface. This seems reasonable since the concentration of these carbon hybridization states is high at room temperature. García-Rosales et al. argue that the dependence of this kinetic ejection process on energy should be similar to physical sputtering, but shifted towards lower threshold energies in the range of 1–2 eV, and that, for hydrogenic impact at energies greater than ~ 90 eV, hydrogenation occurs at the end of range, away from the surface and so the erosion yield from this surface process is reduced. Furthermore, as the temperature of the carbon increases, the sp^3 hybridization state concentration drops, limiting the effect of this surface process to temperatures below T_m . The term proposed to describe this surface effect on erosion is

$$Y_{surf} = [CH sp^3] \frac{Y_{phys}^*}{1 + \exp\left(\frac{E_0 - 90}{50}\right)} \quad (7.9)$$

where Y_{phys}^* is the yield given by modified Bohdanky equation with the lower threshold energies. Note that the term in the denominator restricts the process to energies below 90 eV.

The total chemical erosion yield after incorporating all the above mentioned contributions is

$$Y_{chem} = Y_{surf} + Y_{therm}(1 + DY_{phys}) \quad (7.10)$$

7.2 A simple 1D–KMC model for chemical erosion

A simple 1D–KMC model was implemented as follows: as explained in chapter 2, the probability of the occurrence of a process is determined by ω_o^j and E_m^j . For the thermally activated processes these values were taken from the analytical model (for j^{th} process $k_j \sim \omega_o^j$). For non-thermally activated processes, i.e. hydrogenation and dehydrogenation, $\sigma_H\phi$ and $\sigma_D\phi$ respectively, gives us an idea about ω_o^j (E_m^j is obviously set to zero). So no hydrogen atoms were distributed explicitly and the effect of the flux enters into simulation through ω_o^j ($=\sigma_H\phi$).

7.2.1 Validation of the simple 1D–KMC model for chemical erosion

The 1D–KMC model developed above to simulate the chemical erosion of graphite was used to simulate the experiment performed by Horn et al. [2] where a several mono-layer thick C:H film was grown and exposed to hydrogen ion beam at a flux of $1.9 \times 10^{13} \text{ cm}^{-2} \text{ s}^{-1}$. The results were also compared with the analytical model of Horn et al.

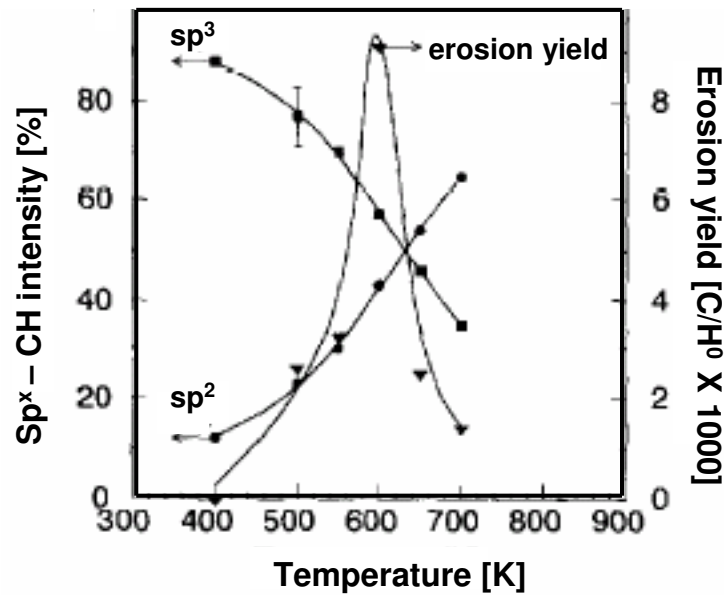


Figure 7.2: Erosion yield and normalized sp^2 / sp^3 contributions at a C:H substrate as a function of temperature obtained from the experiment by Horn and Küppers [2] for hydrogen flux of $1.9 \times 10^{17} \text{ H m}^{-2} \text{ s}^{-1}$.

Fig. 7.3 shows the result of the calculations and it can be clearly seen that the results using KMC method matches very well the experimental results and analytical model [2] (Fig. 7.2). At low temperature the rate of thermal decomposition of radical centers is small and the rather large cross-section σ_H provides effective transfer of these centers back to sp^3 , therefore one sees that at low temperatures carbon is present mainly in sp^3 hybridization state. Whereas, at higher temperatures the radical centers decompose readily and therefore sp^2 carbon atoms dominate. The hydrogen

split-off reaction provides a pathway to destroy erosion relevant groups. Only in an intermediate temperature range the balance between the supply of sp^x centers through dehydrogenation, their thermal decomposition via hydrogen or CH_3 split-off, and hydrogenation to sp^3 enables a noticeable chemical erosion rate.

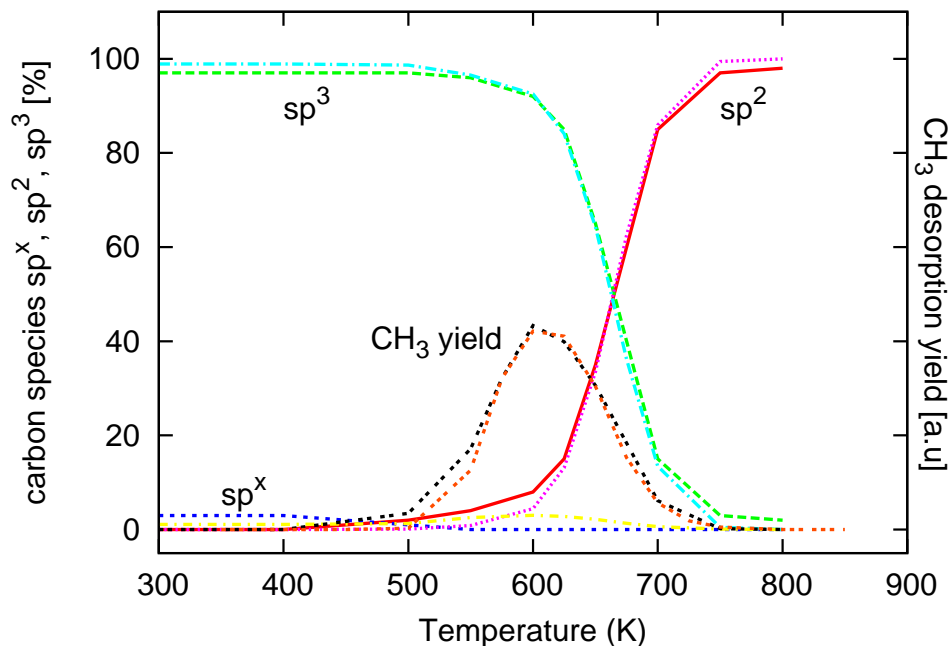


Figure 7.3: Erosion yield and normalized sp^2 / sp^3 contributions at a C:H substrate as a function of temperature obtained from the analytical model proposed by Horn and Küppers [2] for hydrogen flux of $1.9 \times 10^{17} \text{ H m}^{-2} \text{ s}^{-1}$. The same problem was solved using 1D-KMC model. Erosion yield and sp^2 / sp^3 contributions calculated from 1D-KMC model are also plotted here.

7.2.2 Flux dependence of chemical erosion

Fig. 7.4 shows the flux dependence of the chemical erosion yield as a function of temperature as calculated from the analytical model. We see that as the flux is increased the temperature (T_m) at which erosion yield is maximum (Y_m) shifts towards right. T_m depends on the actual flux of hydrogen atoms. This can be explained on the similar lines as was explained in chapter 5 for the reaction rates (for hydrogen molecule formation and similarly here for CH_3 molecule formation). The temperature at which the reaction rate is maximum depends on the balance between diffusion (temperature) and the number density of hydrogen atoms (depends on the combination of flux and

temperature).

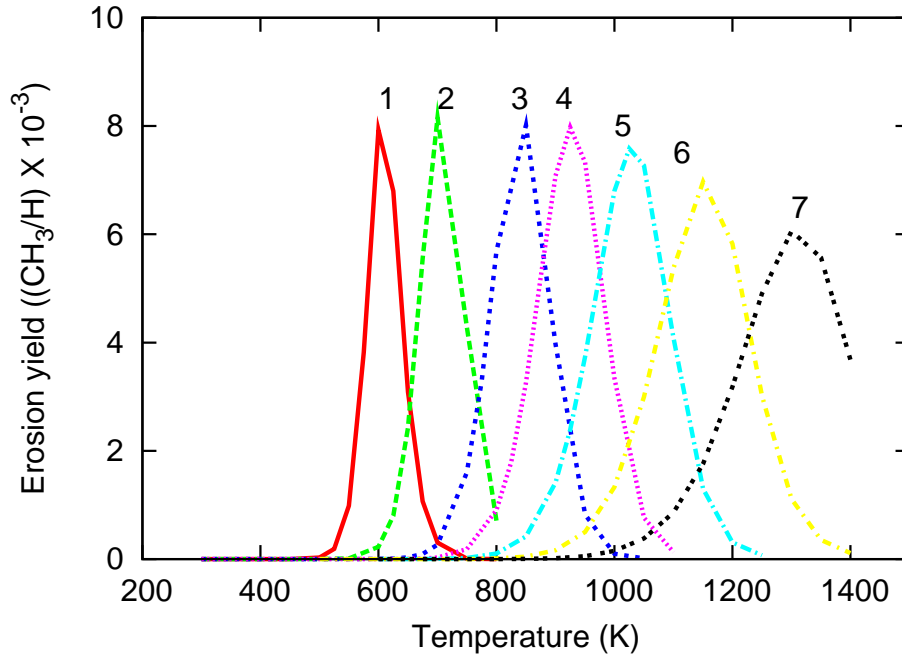


Figure 7.4: Erosion yield calculated from the analytical model proposed by Horn and Küppers [2] as a function of temperature for different fluxes. The flux for curve 1 : $10^{17} H m^{-2} s^{-1}$, 2 : $10^{19} H m^{-2} s^{-1}$, 3 : $10^{21} H m^{-2} s^{-1}$, 4 : $10^{22} H m^{-2} s^{-1}$, 5 : $10^{23} H m^{-2} s^{-1}$, 6 : $10^{24} H m^{-2} s^{-1}$ and 7 : $10^{25} H m^{-2} s^{-1}$.

The maximum erosion yield Y_m is almost constant until a hydrogen flux of $10^{21} H m^{-2} s^{-1}$ beyond which it starts decreasing with increasing flux. As shown in chapter 5, hydrogen recombination rate in general increases with increasing flux which means that lesser hydrogen is available to carry out chemistry processes which leads to hydrocarbon molecule formation. This mechanism contributes to the reduction of Y_m with increasing flux.

However if we compare the maximum erosion yield for a given flux in Fig. 7.4 with Fig. 1.8, it can be seen that the flux dependence is quite weak here. Another point to note here is the shift of T_m with increase in flux. T_m is 1050 K for a flux of $10^{23} H m^{-2} s^{-1}$ and increases further with increasing flux. These T_m values seem to be too high since plasma experiments, at fluxes up to $2 \times 10^{22} H m^{-2} s^{-1}$ suggest that T_m never exceeds ~ 950 K [72]. So the chemistry model proposed by Küppers [2] et al. works quite well in explaining many of the experimentally observed features of the chemical erosion but it does not predict the flux dependence quantitatively.

7.3 A 3D–KMC model for chemical erosion

Coming back to the 3D model developed in chapter 3, the Küppers–cycle described above was included into the model with $\omega_o^j \sim 10^{13} \text{ s}^{-1}$ and $L^j = 0$ for all the carbon species except CH_3 which is the only mobile carbon specie included in the model. For different processes migration energies values mentioned above were used. It must be mentioned that only the contribution from the thermally activated processes are included into the 3D KMC model. The other two contributions i.e. the contribution from radiation damage and kinetic hydrocarbon emission are based on momentum transfer processes. Theses contributions can not be included in the present 3D KMC model as we simulate the reaction of the thermalized hydrogen atoms only. A future project could be to combine the present 3D KMC code with the TRIM code (binary collision code). Then, the contribution to the chemical erosion coming from the momentum transfer processes can also be included.

In the simulations presented in the last chapters carbon atoms were not distributed explicitly as particles and only hydrogen atoms were distributed as particles. All the occupied cells corresponded to the collection of carbon atoms depending on density of the graphite sample (or the void fraction). Whereas, for simulating chemical erosion and specially the change in the hybridization state of carbon atoms as the system evolves, we need to introduce carbon atoms also explicitly as particles and follow their evolution. Even a very small sample contains large number of carbon atoms.

$$N_c = N_A \times \rho \times L_x \times L_y \times L_z / 24 \quad (7.11)$$

where N_c is the number of carbon atoms contained in a graphite sample of size L_x , L_y , L_z and having mass density ρ . N_A is the Avogadro number. This puts a limit on the size of the sample which can be simulated. On the other hand Recalling Eqn. 2.7,

$$\Delta N = \phi \times \Delta t \times L_x \times L_y$$

we see that the number of hydrogen atoms introduced (ΔN) in time step Δt depends on

- flux
- Δt (decreases with increasing temperature (see BKL time step determination))

- system dimension

Thus, if a very small sample is chosen or the incident flux is low then the ΔN becomes too small and it takes very long computational time to introduce enough number of hydrogen atoms which will cause significant hydrogenation and dehydrogenation events. The limitation of handling small samples puts a limit on the flux value that can be simulated. For example, if we want to simulate the chemical erosion of a sample subjected to 50 eV hydrogen ions (penetration depth 2 nm and width of the ion profile is 3.4 nm) we need to take a sample which is at least 6 nm long in Z–direction (surface lies at $Z = 0$). A sample having void fraction 12 % and dimension of $10\text{ nm} \times 10\text{ nm} \times 6\text{ nm}$ in X, Y and Z direction respectively has ~ 50000 carbon atoms. For this particular sample it was found that the lowest flux that can be simulated is $10^{22}\text{ H m}^{-2}\text{ s}^{-1}$.

7.3.1 Setting up the simulation

A porous structure of $1 \times 10^{-8}\text{ m}$, $1 \times 10^{-8}\text{ m}$, $6 \times 10^{-9}\text{ m}$ in X, Y and Z direction respectively was created, with periodic boundary conditions in X and Y direction. The basic cell size was $4 \times 10^{-10}\text{ m}$. The graphite sample was composed of macropores having 12% void fraction with a cubic void of size $1 \times 10^{-9}\text{ m}$. Out of the total 9375 basic cells in the simulation volume 3858 cells (41 %) cells were surface cells. In the coming discussions this sample is referred as sample 1. In order to check the dependence of the chemical erosion process on the internal structure of the graphite another sample was prepared with different void fraction and void size. In this case (referred further on as sample 2) had void fraction of 14 % with cubical voids of 3 nm. Out of the total 9375 basic cells in the simulation volume 3008 cells (32 %) cells were surface cells. The interaction of the sample with a hydrogen ion beam having 50 eV energy and a flux of $10^{22}\text{ H m}^{-2}\text{ s}^{-1}$ was simulated. The hydrogen profile was approximated by a Gaussian having range of 2 nm and standard deviation 1.7 nm.

7.3.2 Results

Fig. 7.5 shows the chemical erosion yield as a function of the surface temperature of the graphite sample 1. As explained earlier, initially the erosion yield increases with temperature and at 750 K it reaches maximum and thereafter it starts decreasing. It is seen that the maximum erosion yield occurs earlier (750 K) as compared to what is

predicted by the analytical model. The maximum erosion yield is ~ 0.04 which is in good agreement with the experimental data (Fig. 1.8).

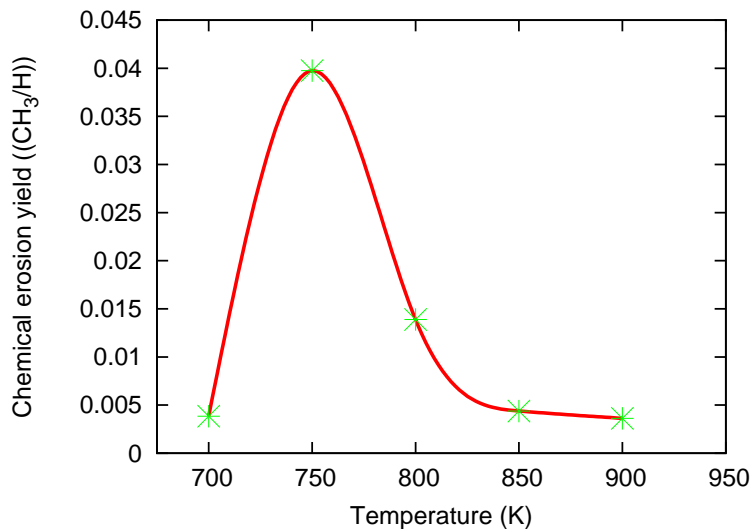


Figure 7.5: Chemical erosion yield calculated from the 3D KMC model as a function of temperature for incident flux of $10^{22} \text{ H m}^{-2} \text{ s}^{-1}$.

Profile of different species

Fig. 7.7 shows the depth profile of the different hydrogenic species. It can be seen that the sample having higher internal porosity (sample 1) shows higher amount of CH_3 formation (specially at 2.7 nm) as compared to sample 2 having lower internal porosity. In sample 1 (41 % internal surface cells), 504 and in sample 2 (32 %), 274 CH_3 molecules were formed. Another interesting thing to notice here is that the maximum amount of the CH_3 is present at the end of the ion range as observed in experiments [68]. This is due to the fact that the energy for the diffusion of CH_3 molecules is around 2.3 eV [73] and it will take a long time for them to diffuse and get desorbed. Due to the very fast diffusion of H_2 molecules (0.06) present in the voids practically no hydrogen molecules in the void are left in the sample. The hydrogen molecules present within the the crystallites are stuck there due to their size and we see that they have depth profile similar to the initial distribution of the hydrogen atoms.

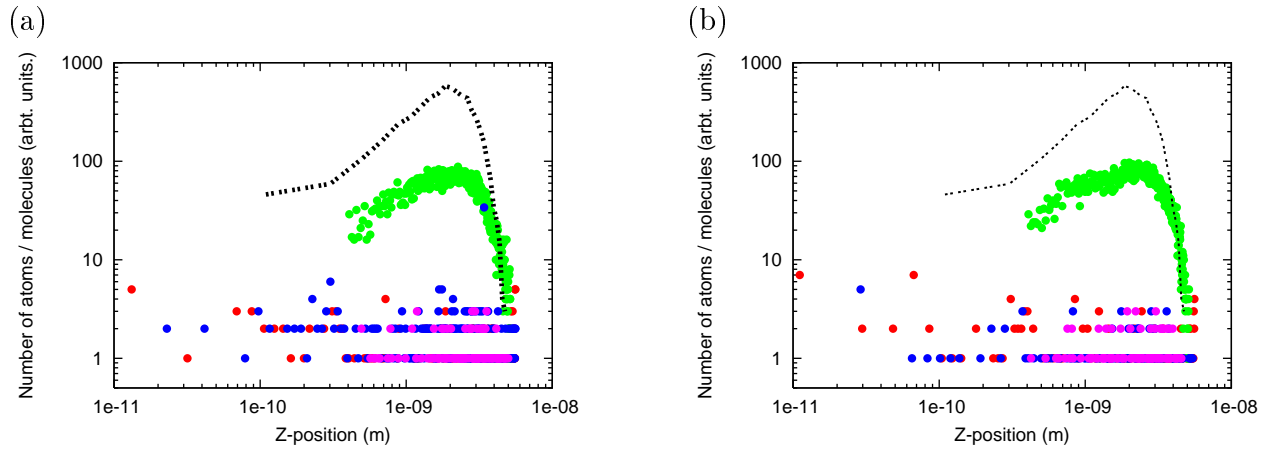


Figure 7.6: Profile of the different hydrogen containing species present in sample 1 (Fig. (a)) and sample 2 (Fig. (b)). Red: Hydrogen atoms adsorbed at the microvoid surfaces, green: hydrogen molecules within the crystallites, magenta: CH_3 molecules within the crystallites, blue: CH_3 molecules adsorbed at the microvoid surfaces and black line: initial profile of the hydrogen atoms.

Point of formation of the different molecular species

Fig. 7.7 shows the point of creation of H_2 and CH_3 molecules in sample 1. Hydrogen molecules are created within as well as much beyond the implantation zone. It is clearly seen that the amount of hydrogen molecules is much higher than that of CH_3 molecules. The formation of CH_3 molecules is confined to the hydrogen implantation range as observed in experiments [68]. The hydrogen atoms diffusing along the micro-void surfaces penetrate beyond the penetration depth and on the way form molecules after which they are quickly released. For the formation of CH_3 at least 4 hydrogenation events should take place. Due to the high H-H recombination probability at this temperature (750 K) very few hydrogen atoms are left for the multiple hydrogenation events and formation of CH_3 . That is why practically no CH_3 is formed beyond the implantation region.

7.4 Recap

The model for chemical erosion of graphite due the thermal hydrogen ion bombardment proposed by Horn et al. [2] was implemented. A simple 1D-KMC model was developed to check the implementation of the basic atomistic process occurring during the chemical erosion process. The simple 1D-KMC model was validated against the analytical model and the experimental results of Horn et al. [2]. It was extended to 3D-KMC model and the effect of the internal structure on the chemical erosion

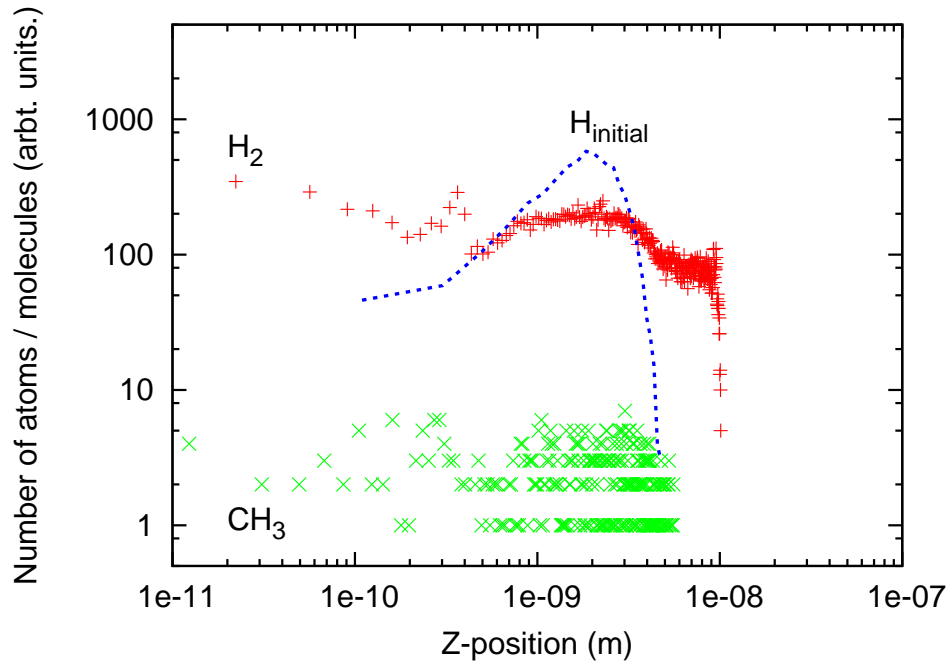


Figure 7.7: Depth profile showing the point of origin of H_2 and CH_3 molecules.

process was studied. The sample having higher internal surface area facilitates the chemical erosion process. The flux dependence predicted with the present 3D-model is very weak. In the next chapter a simple model to simulate the flux dependence of the chemical erosion is presented.

Chapter 8

Flux dependence of chemical erosion: a simple multi-scale model

The models proposed by Küppers et al. and others [36, 44, 2, 5] were successful in explaining many experimentally observed dependencies on energy and temperature, but not the flux dependence of the chemical erosion of graphite during hydrogen ion bombardment. However the analytical model can explain a drop in the erosion yield for high fluxes *provided* the sample temperature exceeds 900 K [70]. In the experiments of Kallenbach et al. at the ASDEX upgrade tokamak, however, the drop in yield is observed even though the temperature is measured to remain below 360 K at the sample surface [74]. Hence, no current analytical model can account for the experimentally observed drop in the carbon erosion yield [75].

Salonen et al. performed MD studies to understand the flux dependence of chemical erosion [23, 24]. A a:C–H sample was bombarded with hydrogen ions of 10 eV energy and at a rate of $2 \times 10^{25} \text{ ions/cm}^2 \text{ s}$. The hydrogen content of the surface first increased strongly and after reaching a $\text{H/C} \sim 0.56$ the sample became supersaturated. After this the hydrogen content in the sample increased only slightly, as the surface was already fully coated with hydrogen. The erosion yield for the unsaturated surface was ~ 0.01 , while for the supersaturated surface it was only ~ 0.001 . The drop of one order of magnitude in the observed erosion yield was believed to be the explanation to the experimentally observed decrease in the erosion yield. The reason to the sharp drop was the decreased carbon collision cross section at a surface which had obtained the temporary supersaturation of H atoms due to the extremely high flux involved.

Inspired by the above study, a simple multi-scale model was developed which can account for the flux dependence of the erosion yield of carbon.

8.1 Description of the model

A virgin graphite structure is created and bombarded with a fixed number of hydrogen ions per time step. The term *time* here does not correspond to the real time and is just used to represent the number of simulation steps. Chemical erosion yield obtained from the analytical models, Y_{Chem} (chapter 7), gives us an idea about the release probability of a CH_3 molecule from the sample at a given temperature and ion energy. On the basis of the position of a hitted carbon atom (geometrical constraints), the carbon atoms present at the surface have a release probability ($P_{Geometry}$) of 0.5. For the atoms present in the deeper layer a *ray tracing* kind of technique was used to find $P_{Geometry}$. For a given carbon atom which was hitted by the incoming hydrogen ion the whole volume lying above the hitted carbon atom was traced with lines originating from it. The scan was done in the steps of one degree both in azimuthal as well as poloidal direction. Then the probability of the carbon atom to get released was calculated from the ratio of the number of hits with other carbon atom (lying above the chosen carbon atom) to the total number of trials. The release probability calculated by the above method is due to the geometry of the sample ($P_{Geometry}$) and the location of the particular carbon atom being hit by the hydrogen atom. The actual release probability ($P_{Release}$) is

$$P_{Release} = P_{Geometry} \times Y_{Chem} \quad (8.1)$$

So the quantity $P_{Release}$, includes the effect of the chemistry processes proposed by Küppers et al. [36] as well as the effect of the geometrical constraints on the carbon release probability due to the roughness of the sample and the position of the hitted carbon atom.

8.2 Setting up the simulation

A crystalline graphite sample of $2.46 \text{ nm} \times 2.13 \text{ nm} \times 13.4 \text{ nm}$ was created. This represents 10, 10 and 20 unit cells in x, y and z directions respectively, 8000 carbon atoms

in the simulation volume and 400 carbon atoms in each layer. In order to avoid the boundary effects the hydrogen atoms were bombarded only within $x = 0.3$ nm and $x = 2.16$ nm and similarly, in y direction from $y = 0.3$ nm and $y = 1.83$ nm. The surface of the sample lies at $z = 0$. The sample was bombarded with n_H number of hydrogen atoms per time step. The n_H value ranging from 1, 5, 10, 25, 50, 100, 500 and 800 were studied. As area of the sample is fixed, therefore, increasing n_H amounts to increase in the incident flux of the hydrogen ions. So, practically the relative flux value in the simulations covered three orders of magnitude. To make the simulations faster the erosion yield (Y_{Chem}) in the present simulations was taken to be 1.

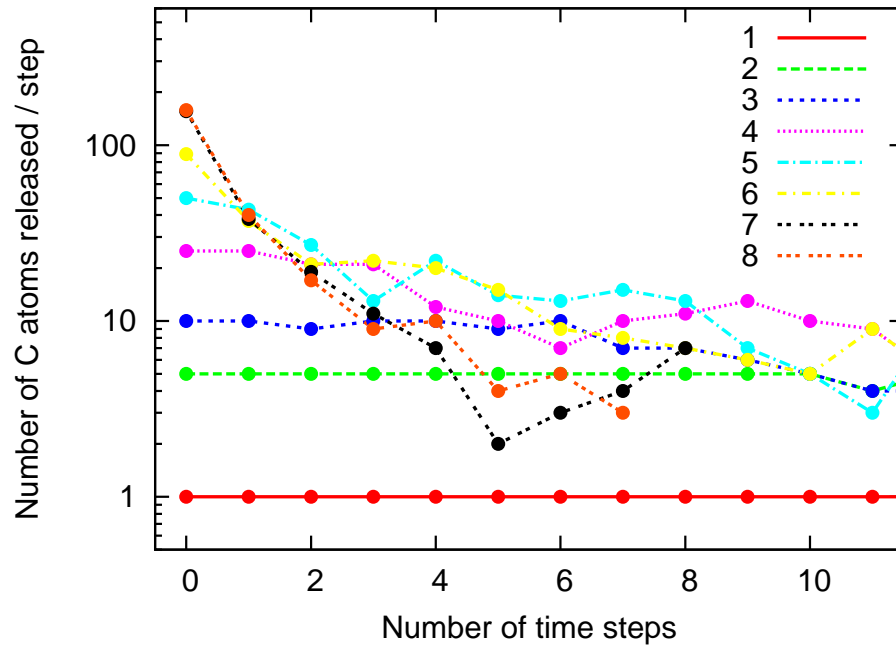


Figure 8.1: The number of carbon atoms released per time step for different incident flux. The number of the hydrogen atoms introduced per time step corresponding to the lines are: 1: 1, 2: 5, 3: 10, 4: 25, 5: 50, 6: 100 7: 500 and 8: 800.

8.3 Results

Fig. 8.1 shows the number of carbon atoms released per time step for different n_H . The number of hydrogen atoms introduced per time step and the number of carbon atoms released per time step are represented by n_H and n_C respectively. It can be seen that for n_H equal to 1 and 5 the ratio n_C/n_H equals 1, which means that every incoming hydrogen ion hits a carbon atom which is released. For $n_H \leq 100$ we see that at least

for the first time step n_C/n_H equals 1 and after that not every incoming hydrogen atom is able to release a carbon atom. This can be explained as follows: The number of carbon atoms on the surface layer are fixed and when the hydrogen atoms strike a smooth surface the release probability of a carbon atom is very high. After some time when sufficient number of carbon atoms are released from the surface it becomes rough. Now the newly arriving hydrogen atoms hit a carbon which might have other carbon atoms on the layer above the hitted carbon atom. This reduces the release probability and we see the drop in the number of atoms released. The key message is that only few surface layers are accessible by the incoming hydrogen flux and this puts an upper limits on the released carbon flux.

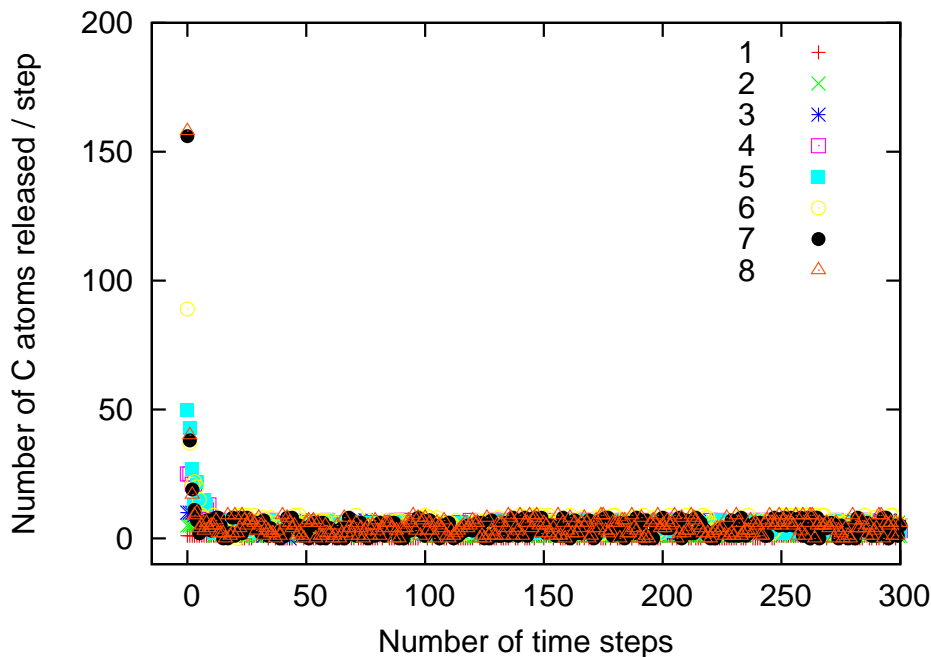


Figure 8.2: Total number of carbon atoms released per time step for different incident flux. The number of hydrogen atoms introduced per time steps corresponding to the lines are: 1: 1, 2: 5, 3: 10, 4: 25, 5: 50, 6: 100 7: 500 and 8: 800.

At what time step this situation will occur definitely depends on n_H and we see that the higher the n_H the sooner the surface carbon atoms are removed turning the surface rough. Another interesting thing to note here is the kind of oscillating behavior of n_C at very high $n_H \geq 100$. First, the atoms are released from the surface layer and n_C is maximum then the surface becomes rougher and therefore the probability of carbon release decreases sharply. As soon as a lot of the carbon atoms from the first layer

are released the second carbon layer gets exposed and again the release probability increases and we see a rise in n_C . Obviously the changes in the levels for higher n_H are much sharper than that of lower n_H .

Fig. 8.3 shows the longer time traces of the number of carbon atoms released per time step (carbon flux) for all n_H values studied here. We see that for $n_H \geq 100$ the carbon flux released from the sample is nearly the same irrespective of the n_H value. This is due to the shielding of the carbon atoms lying in the lower layers. The maximum number of carbon atoms that can be released is determined by the number of carbon atoms present at the surface layer. So the key message is that after a certain critical n_H value, depending on the number of carbon atoms present on the surface of the sample, the released carbon flux is almost constant and if one still increases n_H the erosion yield will obviously decrease. For the sample we study this limit of n_H is 10 after which surface is too rough and the erosion yield starts to drop.

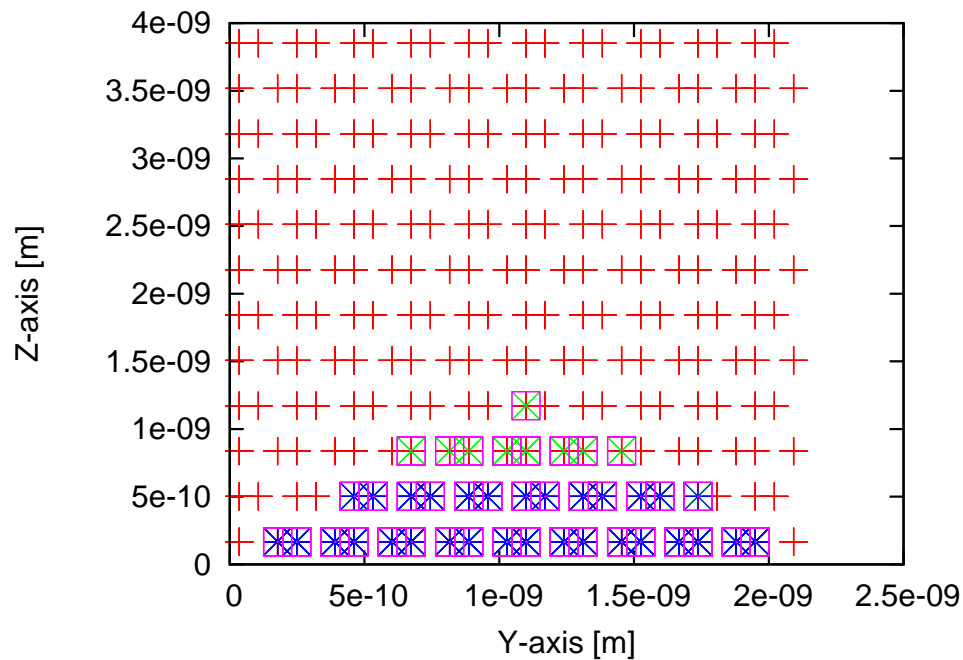


Figure 8.3: Point of release of the C atoms from the graphite sample. The hydrogen atoms introduced per time step corresponding to green: 1, magenta: 100, blue: 800. Red points shows the position of carbon atoms.

Fig. 8.3 shows the point of release of the C atoms from the graphite sample for different n_H . It is seen that for the sample studied here carbon atoms from utmost third

layer were released. It is interesting to note that for lower n_H values the carbon atoms in the lower (third) layers are accessible for the newly hydrogen atoms because of the fact that the surface is not completely covered by the hydrogen atoms and that is why carbon atoms from the third layer are also released. Whereas for very high $n_H \sim 800$ the carbon layers are completely covered due to the high incident hydrogen content. This shields the lower lying carbon atoms and reduces the collision cross-section of hydrogen with carbon atoms. That is why carbon atoms are released only from the first two layers.

Fig. 8.4 shows the erosion yield calculated from the simple multi-scale model. We see that the erosion yield shows the similar order of magnitude decrease in the erosion yield for the similar order of increase in the flux as observed in experiments (fig. 1.8). This confirms that the mechanism responsible of the observed flux dependence has been identified. All the estimates about the chemical erosion and co-deposition were made for the situation where it was assumed that erosion yield has very weak flux dependence. The results presented above shows that the flux dependence of erosion yield is indeed very strong. This means that the problem of carbon erosion and co-deposition will not be as severe as predicted and carbon will still be a good candidate of as a PFM for ITER.

Just to check the idea, similar analysis was done for a sample having carbon atoms distributed uniformly (randomly) in the sample and not in the ordered graphite crystalline structure studied above. Not much difference was observed in the erosion behavior.

8.4 Recap

A simple multi-scale model was developed to study the flux dependence of chemical erosion. The trends in the results agree very well with the experimental results and the model explains the basic mechanism responsible for the observed flux dependence. After a certain critical incident flux, the carbon flux released from a sample becomes equal for all incident hydrogen fluxes and the erosion yield decreases by orders of magnitude with increasing flux. All the estimates about the chemical erosion and co-deposition were made for the situation where it was assumed that erosion yield has

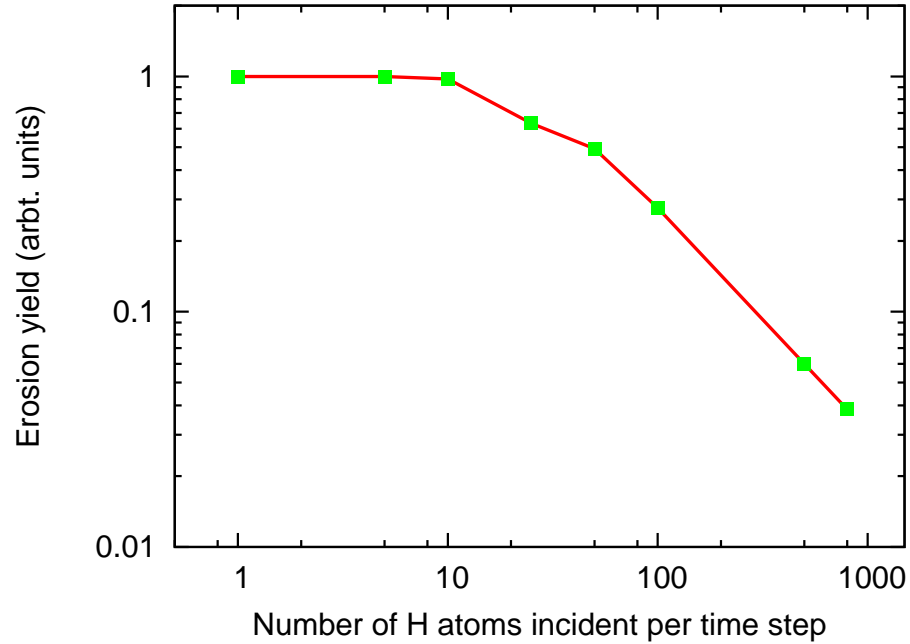


Figure 8.4: Chemical erosion yield as a function of the incident flux.

very weak flux dependence. Whereas the results obtained using the simple multi-scale model shows that the flux dependence of erosion yield is indeed very strong. This means that the problem of carbon erosion and co-deposition will not be as severe as predicted and carbon will still be a good candidate as a PFM for ITER.

Chapter 9

Summary and conclusions

Plasma material interaction in fusion devices is a critical issue that affects the overall machine performance. The knowledge of these processes has a significant role in designing plasma facing materials (PFM) for fusion devices. In the current design of ITER graphite has been chosen as a PFM in the regions where heat loads are extremely high (10 MW/m^2) due to its good thermal conductivity and low atomic number. The two main topics regarding interaction of hydrogen isotopes and graphite that need to be understood properly are: (i) hydrogen retention and release and (ii) chemical erosion and its flux dependence. The problem of tritium retention is extremely important to study because tritium is a radioactive material and its long term inventory in a fusion device should stay below the safety limit (350 g tritium).

The graphite used in fusion devices consists of granules (typically 1-10 micrometer) separated by voids which are typically a fraction of a micrometer. The granules consist of graphitic micro-crystallites of size 10-100 nm separated by micro-voids which are typically one nm [11, 12]. The existence of such large variations in length scales of sub-structures coupled with the wide range of possible atomistic processes makes the study of hydrogen transport and inventory (or complementing this, the formation of hydrocarbons and their transport) in graphite a non-trivial exercise. The answer to this problem is to use multi-scale modeling. The idea is to use the insights gained from the microscopic models (MD or ab-initio methods) for modeling the transport at the meso-scale and further at the macro-scale in order to understand the physical processes contributing to macroscopic transport. By using this philosophy of multi-scale modeling, one is able to develop numerical tools that takes into account the physics

happening at the micro-scale and the efficiency that is comparable to the macroscopic models.

Various studies and experimental databases to understand the interaction of hydrogen isotopes with graphite can be classified into two regimes. First, ion beam experiments, which are carried out using energetic ion beams having energies and fluxes of the order of few keV and 10^{19} ions/m²/s respectively. Second, tokamak experiments where the ion energies close to the divertor region are a few eV to a few hundreds eV and the ion fluxes are very high $\sim 10^{21} - 10^{24}$ ions/m²/s. Both of the scenarios have been studied in the simulations presented here. The different conditions make extrapolation of beam scenarios to fusion devices very problematic. Modeling allows to overcome these problems.

The multi-scale model developed by Warrier et al. [1] has been improved to model the hydrogen reactive-diffusive transport in porous graphite. Various factors affecting the retention and release of hydrogen from graphite have been analyzed. For given ion beam parameters (flux, energy etc.) the internal surface provided by a graphite sample (which is determined by the void fraction, void size and void orientation) determines the retention and release behavior of hydrogen. The void fraction has the most dominant role followed by the void size and then the void orientation comes into play.

The hydrogen retention and release from the deposits collected from the leading edge of the neutralizer of Tore Supra have been analyzed. These deposits consists of micropores with typical size lower than 2 nm ($\sim 11\%$), mesopores (typical size between 2 and 50 nm, $\sim 5\%$) and macropores with a typical size more than 50 nm. The parametrized recombination rate and TGD (Trans-Granular Diffusion) coefficient for the graphite structure representing Tore Supra deposits at meso-scales (sample having micropore and mesopores) have been used as input to model macropores at macro-scales.

At very high fluxes a large quantity of hydrogen molecules get stuck in the graphene planes and this acts as a sink for the hydrogen. The accumulation of the hydrogen on the surfaces of the macropores will lead to high tritium retention levels. The macropores play a dominant role for the release of hydrogen. The hydrogen which is released from the mesopores get trapped at the macropore surfaces. This gives rise to an in-

ternal inventory (or deposition) on macropore surfaces. This mechanism might play a very significant role during the chemical sputtering of such deposits. In that case we will see the deposition of the hydrocarbons on the internal surfaces of the macropores. This will further enhance the tritium retention problem. The typical residence time of the hydrogen in graphite calculated using the 3D-KMC model was found to be in good agreement with the experiments.

The multi-scale model was also used to study the hydrogen isotope exchange reaction in graphite. The mixed molecule formation during the exposure to hydrogen and deuterium ion beams having completely separate ion profile (penetration depths) demonstrates that hydrogen molecule formation is not a local process. It takes place throughout the implantation zone and not only at the end of the ion range. The main factors affecting the mixed molecule formation are:

- internal structure of graphite, which affects diffusion coefficient and consequently molecule formation and atomic re-emission
- temperature of the sample, this affects atomic diffusion, which is an important factor for mixed molecule formation.

The model for chemical erosion of graphite due the thermal hydrogen ion bombardment proposed by Horn et al. [2] was implemented. A simple 1D-KMC model was developed to check the implementation of the basic atomistic process occurring during the chemical erosion process. The simple 1D-KMC model was successfully validated against the analytical model and the experimental results of Horn et al. [2]. It was extended to 3D-KMC model and the effect of the internal structure on the chemical erosion process was studied. The samples having higher internal surface areas facilitate the chemical erosion process. The flux dependence predicted with this 3D-model was very weak.

To study the flux dependence of chemical erosion a simple multi-scale model was developed. The trends in the results agree very well with the experimental results and the model explains the basic mechanism responsible for the observed flux dependence. Due to the shielding of the carbon atoms lying in the lower layers only few surface layers are accessible by the incoming hydrogen ions and this puts an upper limit on the released carbon flux. The erosion yield calculated from the simple multi-scale shows

a very strong flux dependence. All the estimates about the chemical erosion and co-deposition were made for the situation where it was assumed that the erosion yield has very weak flux dependence. Whereas the results presented above shows that the flux dependence of erosion yield is indeed very strong. This means that the problem of carbon erosion and co-deposition will not be as severe as predicted and carbon will still be a good candidate as a PFM for ITER.

Bibliography

- [1] M. Warrier. Multi-scale modeling of hydrogen isotope transport in porous graphite. *Ph.D. Dissertation, Faculty of Mathematics and Natural Science, Uni. Greifswald, Germany*, (2004).
- [2] A. Horn, A. Schenk, J. Biener, B. Winter, C. Lutterloh, M. Wittmann, and J. Küppers. H atom impact induced chemical erosion reaction at C:H film surfaces. *Chem. Phys. Lett.*, 231(2-3):193–198, (1994).
- [3] V. Phillips. Plasma-wall interaction, a key issue on the way to a steady state burning device. *Phys. Scr.*, T123:24–32, (2006).
- [4] J. Roth, E. Vietzke, and A. A. Haasz. Atomic and Plasma-Material Interaction Data for Fusion. *Supplement to the J. Nucl. Fusion*, 1:63, (1991).
- [5] A. A. Haasz B. V. Mech and J. W. Davis. Model for the chemical erosion of graphite due to low-energy H⁺ and D⁺ impact. *J. Appl. Phys.*, 84(3):1655–1669, (1998).
- [6] J. W. Davis and A. A. Haasz. Impurity release from low - Z materials under light particle bombardment. *J. Nucl. Mater.*, 241-243:37–51, (1997).
- [7] Y. Ueda. Impacts of carbon impurities in hydrogen plasmas on tungsten blistering. *Nucl. Fusion*, 44:62–67, (2004).
- [8] G. Federici. Plasma-material interactions in current tokamaks and their implications for next step fusion reactors. *Nucl. Fus.*, 41(12R):1968–2137, (2001).
- [9] J. D. Huba. Revised nrl plasma formulary. *Naval Research Laboratory, Washington DC*, page 56, (2000).

- [10] V. Philipps, J. Roth, and A. Loarte. Key issues in Plasma-Wall Interactions for ITER. *30th EPS conference on controlled fusion and plasma physics*, (July, 2003).
- [11] R. Schneider, A. Rai, A. Mutzke, M. Warrier, E. Salonen, and K. Nordlund. Dynamic Monte-Carlo modeling of hydrogen isotope reactive-diffusive transport in porous graphite. *J. Nucl. Mater.*, 367-370:1238–1242, (2007).
- [12] M. Warrier. Subroutines for some plasma surface interaction processes: physical sputtering, chemical erosion, radiation enhanced sublimation, backscattering and thermal evaporation. *Comp. Phys. Commu.*, 160(1):46–68, (2004).
- [13] K. L. Wilson and W. L. Hsu. Hydrogen recycling properties of graphite. *J. Nucl. Mater.*, 145-147:121–130, (1987).
- [14] S. Chiu and A. A. Haasz. Chemical release of implanted deuterium in graphite. *J. Vac. Sci. Technol. A*, 9:747, (1991).
- [15] R. A. Causey, M. I. Baskes, and K. L. Wilson. The retention of deuterium and tritium in POCO AXF-5Q graphite. *J. Vac. Sci. Technol. A*, 4(3):1189–1192, (1986).
- [16] R. A. Causey. The interaction of tritium with graphite and its impact on tokamak operations. *J. Nucl. Mater.*, 162-164:151–161, (1989).
- [17] J. N. Brooks, D. Alman, G. Federici, D. N. Ruzic, and D. G. Whyte. Erosion/redeposition analysis: status of modeling and code validation for semi-detached tokamak edge plasmas. *J. Nucl. Mater.*, 266-269:58–66, (1999).
- [18] J.P. Coad, N. Bekris, J.D. Elder, S.K. Erents, D.E. Hole, K.D. Lawson, G.F. Matthews, R.D. Penzhorn, and P.C. Stangeby. Erosion/deposition issues at JET. *J. Nucl. Mater.*, 290-293:224–230, (2001).
- [19] C. Martin, M. Richou, W. Saikaily, B. Pégourié, C. Brosset, and P. Roubin. Multiscale study of the porosity of carbon deposits collected in Tore Supra. *J. Nucl. Mater.*, 363-365:1251–1255, (2007).
- [20] J. Roth, R. Preuss, W. Bohmeyer, S. Brezinsek, A. Cambe, E. Casarotto, R. Doerner, E. Gauthier, G. Federici, S. Higashijima, J. Hogan, A. Kallenbach, A. Kirschner, H. Kubo, J.M. Layet, T. Nakano, V. Philipps, A. Pospieszczyk,

- R. Pugno, R. Ruggiéri, B. Schweer, G. Sergienko, and M. Stamp. Flux dependence of carbon chemical erosion by deuterium ions. *Nucl. Fus.*, 44(11):L21–L25, (2004).
- [21] V. Dose, R. Preuss, and J. Roth. Evaluation of chemical erosion data for carbon materials at high ion fluxes using Bayesian probability theory. *J. Nucl. Mater.*, 288(2-3):153–162, (2001).
- [22] Ph. Mertens, S. Brezinsek, P. T. Greenland, J. D. Hey, A. Pospieszczyk, D. Reiter, U. Samm, B. Schweer, G. Sergienko, and E. Vietzke. Hydrogen release from plasma-facing components into fusion plasmas—recent results from a spectroscopic approach. *Plasma Phys. Control. Fusion*, 43:A349, (2001).
- [23] E. Salonen, K. Nordlund, J. Tarus, T. Ahlgren, J. Keinonen, and C. H. Wu. Suppression of carbon erosion by hydrogen shielding during high-flux hydrogen bombardment. *Phys. Rev. B*, 60:14005–14008, (1999).
- [24] E. Salonen, K. Nordlund, J. Keinonen, and C. H. Wu. Carbon erosion mechanisms in tokamak divertor materials: insight from molecular dynamics simulation. *J. Nucl. Mater.*, 290-293:144–147, (2001).
- [25] P. E. Kloeden and E. Platen. Numerical solution of Stochastic Differential Equations. *Springer series in Applications of Mathematics*, 23, (1999).
- [26] K. A. Fichthorn and W. H. Weinberg. Theoretical foundations of dynamical Monte Carlo simulations. *J. Chem. Phys.*, 95(2):1090–1096, (1991).
- [27] F. Graziani. Radiation transport in 3D heterogeneous materials: Direct numerical simulation. *APS meeting : Conference on computational physics 2002, August 25-28 (San Diego)*, (2002).
- [28] W. Möller. Hydrogen trapping and transport in carbon. *J. Nucl. Mater.*, 162-164:138–150, (1989).
- [29] A. A. Haasz, P. Franzen, J. W. Davis, S. Chiu, and C. S. Pitcher. Two-region model for hydrogen trapping in and release from graphite. *J. Appl. Phys.*, 77(1):66–86, (1995).

- [30] G. Federici and C. H. Wu. Modeling of plasma hydrogen isotope behavior in porous materials (graphites or carbon-carbon composites). *J. Nucl. Mater.*, 186(2):131–152, (1991).
- [31] A. Hassanein, B. Wiechers, and I. Konkashbaev. Tritium behavior in eroded dust and debris of plasma-facing materials. *J. Nucl. Mater.*, 258-263:295–300, (1998).
- [32] B. M. U. Scherzer, M. Wielunski, Möller, A. Turos, and J. Roth. Hydrogen-ion-induced detrapping of implanted deuterium in graphite. *Nucl. Instrum. Methods Phys. Res. B*, 33:714–718, (1988).
- [33] B. M. U. Scherzer, Wang Jianhua, and Möller. Temperature dependence of ion-induced detrapping of deuterium in graphite. *J. Nucl. Mater.*, 162-164:1013–1018, (1989).
- [34] W. Möller and B. M. U. Scherzer. Modeling of hydrogen implantation into graphite. *J. Appl. Phys.*, 64:4860–4866, (1988).
- [35] H. Atsumi, S. Tokura, and M. Miyake. Absorption and desorption of deuterium on graphite at elevated temperatures. *J. Nucl. Mater.*, 155-157:241–245, (1988).
- [36] J. Küppers. The hydrogen surface chemistry of carbon as a plasma facing material. *Surface Science Reports*, 22:249–321, (1995).
- [37] E. Salonen, K. Nordlund, J. Keinonen, , and C. H. Wu. Swift chemical sputtering of amorphous hydrogenated carbon. *Phys. Rev. B*, 63(19):195415, (2001).
- [38] Y. Ferro, F. Marinelli, and A. Allouche. Density functional theory investigation of the diffusion and recombination of H on a graphite surface. *Chemical Physics Letters*, 368:609–615, (2003).
- [39] Y. Ferro, F. Marinelli, and A. Allouche. Density functional theory investigation of H adsorption and H₂ recombination on the basal plane and in the bulk of graphite: Connection between slab and cluster model. *J. Chem. Phys.*, 116(18):8124–8131, (2002).
- [40] M. Warrier, R. Schneider, E. Salonen, and K. Nordlund. Modeling of the diffusion of hydrogen in porous graphite. *Physica Scripta*, T108:85, (2004).

- [41] M. Warrier, R. Schneider, E. Salonen, and K. Nordlund. Multi-scale modelling of hydrogen isotope diffusion in graphite. *Contrib. Plasma Phys.*, 44(1-3):307–310, (2004).
- [42] K. L. Wilson, R. Bastasz, R. A. Causey, D. K. Brice, B. L. Doyle, W. R. Wampler, W. Möller, B. M. U. Scherzer, and T. Tanabe. Trapping, detrapping and release of implanted hydrogen isotopes. *Atomic and plasma-material interaction data for fusion (supplement to the journal Nuclear Fusion)*, 1:31–50, (1991).
- [43] M. Warrier, R. Schneider, E. Salonen, and K. Nordlund. Multi-scale modeling of hydrogen isotope transport in porous graphite. *J. Nucl. Mater.*, 337-339:580–584, (2005).
- [44] M. Wittmann and J. Küppers. A model of hydrogen impact induced chemical erosion of carbon based on elementary reaction steps. *J. Nucl. Mater.*, 227:186–194, (1996).
- [45] S. Chiu and A. A. Haasz. Molecular formation due to sequential and simultaneous exposure of graphite to H^+ and D^+ . *J. Nucl. Mater.*, 196-198:972–976, (1992).
- [46] M. Mayer, M. Balden, and R. Behrisch. Deuterium retention in carbides and doped graphites. *J. Nucl. Mater.*, 252:55–62, (1998).
- [47] S. L. Kanashenko, A. E. Gorodetsky, V. N. Chernikov, A. V. Markin, A. P. Zakharov, B. L. Doyle, and W. R. Wampler. Hydrogen adsorption on and solubility in graphites. *J. Nucl. Mater.*, 233-237:1207–1212, (1996).
- [48] V. N. Chernikov, W. R. Wampler, A. P. Zakharov, and A. E. Gorodetsky. Deuterium trapping in deep traps of differently oriented pyrolytic graphite exposed to D_2 gas at 1473 K. *J. Nucl. Mater.*, 264:180–197, (1999).
- [49] H. Atsumi. Hydrogen bulk retention in graphite and kinetics of diffusion. *J. Nucl. Mater.*, 307-311:1466–1470, (2002).
- [50] K. Ashida, K. Ichimura, M. Matsuyama, and K. Watanabe. Thermal desorption of hydrogen, deuterium and tritium from pyrolytic graphite. *J. Nucl. Mater.*, 128 & 129:792, (1984).
- [51] M. V. Smoluchowski. *Z. Physik Chem.*, 107:463, (1957).

- [52] T. R. Waite. Theoretical treatment of the kinetics of diffusion-limited reactions. *Phys. Rev.*, 107(2):463–470, (1957).
- [53] G. Duesing, H. Hemmerich, W. Sassin, and W. Schilling. Proceedings of the International Conference on Vacancies and Interstitials in Metals, Jülich, Germany, 1968. (*North-Holland, Amsterdam, 1970*), page 246, (1970).
- [54] W. Möller, P. Borgesen, and B. M. U. Scherzer. Thermal and ion-induced release of hydrogen atoms implanted into graphite. *Nucl. Instrum. Methods Phys. Res. B*, 19/20:826–831, (1987).
- [55] H. Atsumi. Mechanism of hydrogen trapping and transport in carbon materials. *Phy. Scr.*, T103:77–80, (2003).
- [56] P. Franzen and E. Vietzke. Atomic release of hydrogen from pure and boronized graphites. *J. Vac. Sci. Technol. A*, 12:820–825, (1994).
- [57] J. W. Davis, A. A. Haasz, and D. S. Walsh. Flux and fluence dependence of H⁺ trapping in graphite. *J. Nucl. Mater.*, 176-177:1000–1004, (1990).
- [58] M. Braun and B. Emmoth. Deuterium implantation in carbon at elevated temperatures. *J. Nucl. Mater.*, 128-129:657–663, (1984).
- [59] J. A. Sawicki, J. Roth, and L. M. How. Thermal release of tritium implanted in graphite studied by t(d, α)n nuclear reaction depth profiling analysis. *J. Nucl. Mater.*, 162-164:1019–1024, (1989).
- [60] B. L. Doyle, W. R. Wampler, and D. K. Brice. Temperature dependence of H saturation and isotope exchange. *J. Nucl. Mater.*, 103:513–517, (1981).
- [61] B.M.U. Scherzer, R.A. Langley, W. Möller, J. Roth, and R. Schultz. Influence of damage on the thermal release of deuterium implants in graphite. *Nucl. Instruments and Methods.*, 194(1-3):497–500, (1982).
- [62] R. A. Langley, R. S. Blewer, and J. Roth. Behavior of implanted D and He in pyrolytic graphite. *J. Nucl. Mater.*, 76-77:313–321, (1978).
- [63] B. Pégourié, C. Brosset, E. Delchambre, T. Loarer, P. Roubin, E. Tsitrone, J. Bucalossi, J. Gunn, H. Khodja, C. Lafon, C. Martin, P. Parent, R. Reichle, and Tore Supra Team. Long discharge particle balance and fuel retention in Tore Supra. *Physics Scripta*, T111:23–28, (2004).

- [64] E. Tsitrone, D. Reiter, T. Loarer, C. Brosset, J. Bucalossi, L. Begrambekov, C. Grisolia, A. Grosman, J. Gunn, and et al. J. Hogan. Role of wall implantation of charge exchange neutrals in the deuterium retention for Tore Supra long discharges. *J. Nucl. Mater.*, 337-339:539–543, (2005).
- [65] E. Tsitrone, C. Brosset, and et al. J. Bucalossi. *Proceedings of 20th IAEA Fusion Energy Conference, Vilamoura*, (2004).
- [66] C. Martin, M. Richou, W. Sakaily, B. Pégourié, C. Brosset, and P. Roubin. Multiscale study of the porosity of carbon deposits collected in Tore Supra. *J. Nucl. Mater.*, 363-365:1251–1255, (2007).
- [67] G. Haas, R. Maingi, J. Neuhauser, ASDEX Upgrade team, and DIII-D team. Dynamic hydrogen retention in the walls of the tokamaks ASDEX Upgrade and DIII-D. *J. Nucl. Mater.*, 266-269:1065–1071, (1999).
- [68] W. Möller and B. M. U. Scherzer. Subsurface molecule formation in hydrogen-implanted graphite. *Appl. Phys. Lett.*, 50(26):1870–1872, (1987).
- [69] B. Tsuchiya and K. Morita. Isotope difference between hydrogen inventories in graphite under simultaneous H^+ and D^+ irradiation. *J. Nucl. Mater.*, 233-237:1213–1217, (1996).
- [70] J. Roth and C. Garcia-Rosales. Analytic description of the chemical erosion of graphite by hydrogen ions. *Nucl. Fusion*, 36:1647–1659, (1996).
- [71] C. García-Rosales, W. Eckstein, and J. Roth. Revised formulae for sputtering data. *J. Nucl. Mater.*, 218:8–17, (1994).
- [72] D. M. Goebel, J. Bohdansky, R. W. Conn, Y. Hirooka, W. K. Leung, R. E. Nygren, and G. R. Tynan. Erosion and redeposition of graphite by hydrogen plasmas. *Fusion Technol.*, 15:102, (1988).
- [73] E. Salonen. Overview of the atomistic modeling of the chemical erosion of carbon. *Phys. Scr.*, T111:133–137, (2004).
- [74] A. Kallenbach, A. Thoma, A. Bard, K.H. Behringer, K. Schmidtman, M. Weinelich, and ASDEX Upgrade Team. Evidence for hydrogen flux dependence of the apparent chemical erosion yield of graphite under high flux conditions. *Nucl. Fusion*, 38:1097–1103, (1998).

- [75] A. Kallenbach, A. Bard, D. Coster, R. Dux, C. Fuchs, J. Gafert, A. Herrmann, R. Schneider, and ASDEX-Upgrade Team. New results on carbon release and transport in ASDEX-Upgrade. *J. Nucl. Mater.*, 266-269:343, (1999).

Acknowledgments

A journey is easier when you travel together. Interdependence is certainly more valuable than independence. This thesis is a result of approximately three years of work whereby I have been accompanied and supported by many people. It is a pleasant aspect that I have now the opportunity to express my gratitude for all of them.

The first person I would like to thank is my supervisor Dr. Ralf Schneider. I have been working on this project since March 2005. During these years I have known Ralf as a sympathetic and principle-centered person. His overly enthusiastic and integral view on research and his mission for providing 'only high-quality work and not less', has made a deep impression on me. I owe him lots of gratitude for having me shown this way of research. I thank Prof. Dr. Jürgen Nührenberg for inviting me to IPP Greifswald, to do my PhD.

I would like to thank Dr. Manoj Warriar for letting me use his DiG code and for the great discussions throughout my PhD period. The discussions during his visit to Greifswald as well as via gmail chats and phone with him were very useful. I specially want to thank him for teaching me how to write scientific papers neatly and clearly.

My colleagues at Stellarator division at IPP were helpful in a variety of ways and I thank each of them. Special thanks to Jutta Gauger and Susann Wangnett who made difficult office procedure look simple. Henry and Matthias made stubborn compilers, puzzling networks and unyielding computing systems, behave synergistically. Many thanks to Andreas Mutzke for teaching me TRIM-TRIDYN code. I would specially like to thank Matthias Köppen for helping me in using Matlab data visualization techniques. Many thanks to Andrea Puls for the graphic support for making the pictures look nicer.

The International Max–Planck Research School (IMPRS) was interesting and useful. Thanks to Prof. Thomas Klinger and Prof. Olaf Grulke who made it so. I would like to thank Frau. Schirmacher, the librarian of IPP–Greifswald for her help in obtaining numerous references and books.

As I submit this thesis I remember a host of friends and relatives who have wished me well and helped me at various times. I would like to thank my parents–in–law for supporting me throughout the PhD duration. Finally a big thanks to my husband Gaurang Dilip Phadke for help, support and encouragement he has extended to me till now in my life.

Finally, today I just want to stop and take a minute to thank the Almighty God - the source of all good things - who always blessed me with the best things I could wish for in my life.

Hiermit erkläre ich, daß diese Arbeit bisher von mir weder an der Mathematisch-Naturwissenschaftlichen Fakultät der Ernst-Moritz-Arndt-Universität Greifswald noch einer anderen wissenschaftlichen Einrichtung zum Zwecke der Promotion eingereicht wurde.

Ferner erkläre ich, daß ich diese Arbeit selbständig verfaßt und keine anderen als die darin angegebenen Hilfsmittel benutzt habe.

Greifswald, im Dezember 2007

(Abha Rai)